

EMPIRICAL EQUATION FOR DETERMINATION OF SAFE PIT SLOPE
GEOMETRY AT PHU KHAM MINING



A Thesis Submitted in Partial Fulfillment of the Requirements for the
Degree of Master of Engineering in Civil, Transportation
and Geo-Resources Engineering
Suranaree University of Technology
Academic Year 2022

สมการเชิงประจักษ์สำหรับการกำหนดรูปร่างเชิงเรขาคณิตที่ปลอดภัยของ
ความลาดเอียงบ่อเหมืองภูค้ำ

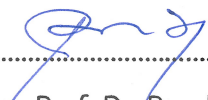



วิทยานิพนธ์นี้เป็นส่วนหนึ่งของการศึกษาตามหลักสูตรปริญญาวิศวกรรมศาสตรมหาบัณฑิต
สาขาวิชาวิศวกรรมโยธา ขนส่ง และทรัพยากรธรณี
มหาวิทยาลัยเทคโนโลยีสุรนารี
ปีการศึกษา 2565


EMPIRICAL EQUATION FOR DETERMINATION OF SAFE PIT SLOPE
GEOMETRY AT PHU KHAM MINING


Suranaree University of Technology has approved this thesis submitted in partial fulfillment of the requirements for a Master's Degree.


Thesis Examining Committee


.....
(Assoc. Prof. Dr. Pornkasem Jongpradist)
Chairperson


.....
(Dr. Thanittha Thongrapha)
Member (Thesis Advisor)


.....
(Asst. Prof. Dr. Prachya Tepnarong)
Member


.....
(Assoc. Prof. Dr. Chatchai Jothityangkoon)
Vice Rector for Academic Affairs and
Quality Assurance


.....
(Assoc. Prof. Dr. Pornsiri Jongkol)
Dean of Institute of Engineering

วสันต์ สารณาด : สมการเชิงประจักษ์สำหรับการกำหนดรูปร่างเชิงเรขาคณิตที่ปลอดภัย
ของความลาดเอียงบ่อเหมืองภูค่า (EMPIRICAL EQUATION FOR DETERMINATION OF
SAFE PIT SLOPE GEOMETRY AT PHU KHAM MINING) อาจารย์ที่ปรึกษา : อาจารย์ ดร.
ธนัชฐา ทองประภา, 93 หน้า.

คำสำคัญ: มุมเอียงของความลาดชัน/รอยเลื่อน/มุมสัมประสิทธิ์ความเสียดทาน

การศึกษานี้มุ่งศึกษาค่ากำลังเฉือนสูงสุดของมวลหินและรอยเลื่อนบริเวณผนังบ่อใต้ของ
เหมืองภูค่าโดยการทดสอบกำลังเฉือนในห้องปฏิบัติการและแบบจำลองทางตัวเลขคอมพิวเตอร์ ผล
การทดสอบที่ได้ถูกนำไปใช้ในแบบจำลองทางคอมพิวเตอร์ เพื่อวิเคราะห์เสถียรภาพด้วยระเบียบวิธี
เชิงตัวเลข โดยการใช้ Distinct element method (UDEC code) ดำเนินภายใต้ความแตกต่างของ
มุมความลาดเอียง มุมของรอยเลื่อนและค่ากำลังเฉือนของหิน ผลการจำลองทางคอมพิวเตอร์ระบุว่า
ค่าความปลอดภัยของความลาดเอียงเพิ่มขึ้นด้วยการเพิ่มขึ้นของค่าความเค้นยึดติด สัมประสิทธิ์ความ
เสียดทาน และ ระยะทางระหว่างรอยเลื่อนกับยอดของความชัน ขณะเดียวกันค่าความปลอดภัยลดลง
ด้วยการเพิ่มขึ้นของมุมการเอียงของการลาดชัน สมการเชิงประจักษ์ได้ถูกพัฒนาจากผลการจำลองเชิง
ตัวเลขเพื่อใช้ในการคาดคะเนค่าความปลอดภัยของความลาดเอียงภายใต้ความแตกต่างของมุมลาด
เอียง ค่าความเค้นยึดติดและสัมประสิทธิ์ความเสียดทานของมวลหินเพดาน (Hanging wall) ในขณะ
ที่ระยะทางระหว่างรอยเลื่อนกับยอดของความชัน และมุมของรอยเลื่อนไม่ส่งผลมากต่อค่าความ
ปลอดภัย จึงไม่ถูกนำมาพิจารณาในสมการเชิงประจักษ์

สาขาวิชาเทคโนโลยีธรณี

ปีการศึกษา 2565

ลายมือชื่อนักศึกษา.....*วสันต์ สารณาด*.....

ลายมือชื่ออาจารย์ที่ปรึกษา.....*ดร.ธนัชฐา*.....

WASAN SARANART : EMPIRICAL EQUATION FOR DETERMINATION OF SAFE PIT
SLOPE GEOMETRY AT PHU KHAM MINING. THESIS ADVISOR : THANITTHA
THONGPRAPHA, Ph.D., 93 PP.

Keywords: SLOPE ANGLE/FAULT/FRICTION ANGLE/COHESION

This study aims to investigate shear strength parameters of rock mass and fault zone at South Wall of Phu Kham open pit mine by direct shear testing and numerical simulation. The test results are simulated using distinct element method (UDEC code) under different slope face angles, fault angles and shear strength parameters. The model results show that safety factors of slopes increase with increasing cohesions, friction angles and distances between fault and slope face, but decreases with increasing slope face angles. An empirical equation is derived based on the simulation results. It can be used to predict the safety factor of slopes under various slope face angles, cohesions and friction angles of the hanging wall. Distances between fault from crest and fault angle are excluded in equation as they are not sensitive to the factor of safety.

มหาวิทยาลัยเทคโนโลยีสุรนารี

School of Geotechnology

Academic Year 2022

Student's Signature.....

Advisor's Signature.....

Wasan Saranart
Thanittha Thongprapha

ACKNOWLEDGEMENT

I would like to express the Institute of Research and Development, Suranaree University of Technology funding to this research. I would like to thank my honest appreciation to Dr. Thanittha Thongrapha for her valuable guidance. I appreciate her powerful support, suggestions, and encouragement during the research period. I also would like to thank Professor Dr. Kittitep Fuenkajorn for valuable suggestions, support and comment on my research works. Grateful thanks to all staff of Geomechanics Research Unit who helped and supported my work.

Wasan Saranart



TABLE OF CONTENTS

	Page
ABSTRACT (THAI).....	I
ABSTRACT (ENGLIST).....	II
ACKNOWLEDGEMENT	III
TABLE OF CONTENTS	IV
LIST OF TABLES	VII
LIST OF FIGURES.....	VIII
LIST OF ABBREVIATIONS	IX
CHAPTER	
I INTRODUCTION	1
1.1 Background and rationale.....	1
1.2 Research objectives	2
1.3 Scope and limitations.....	2
1.4 Research methodology	3
1.4.1 Literature review.....	4
1.4.2 Sample preparation and laboratory testing.....	4
1.4.3 Numerical simulations.....	4
1.4.4 Development of mathematical relationships.....	4
1.4.5 Discussions and conclusions.....	4
1.5 Thesis Contents.....	5
II LITERATURE REVIEWS	6
2.1 Geology and lithology of Phu Kham site.....	6
2.1.1 Geology.....	6
2.1.2 Lithology and weathering domains.....	9
2.1.3 Structural geology in Southern Walls.....	15
2.2 Joint shear strengths.....	22

TABLE OF CONTENTS (Continued)

	Page
2.3 Rock slope stability and rock mass classification	24
2.3.1 Slope failure modes.....	24
2.3.2 Slope stability assessment.....	27
2.4 Numerical model.....	27
2.5 Relationship between slope geometry, mechanical properties of rock and slope stability.....	34
III LABORATORY TESTING	38
3.1 Introduction.....	38
3.2 Sample preparation.....	38
3.3 Uniaxial compressive strength test.....	47
3.4 Direct shear tests of rock specimens on rough fracture.....	48
3.5 Direct shear tests of soil samples.....	55
IV NUMERICAL SIMULATIONS.....	59
4.1 Introduction.....	59
4.2 Numerical simulations.....	59
4.2.1 Effect of slope face angle.....	63
4.2.2 Effect of distance between fault and crest.....	65
4.2.3 Effect of fault angle.....	68
4.2.4 Effect of mechanical properties of hanging rock.....	71
4.3 Prediction.....	76
V DISCUSSIONS AND CONCLUSIONS.....	78
5.1 Discussions.....	78
5.2 Conclusions.....	81
5.3 Recommendations for future studies.....	82
REFERENCES	83
APPENDIX A. List of Publications	86
BIOGRAPHY	93

LIST OF TABLES

Table	Page
2.1	Comparison between limit equilibrium and numerical analysis methods28
2.2	Implication of slope height on its factor of safety (Igwe and Chukwu, 2018).....35
2.3	Significance of slope angle on factor of safety (Igwe and Chukwu, 2018).....35
2.4	Effect of cohesion on factor of safety (Igwe and Chukwu, 2018)36
2.5	Effect of internal friction angle on factor of safety (Igwe and Chukwu, 2018)37
3.1	Dimension of VTF specimen for UCS testing.....43
3.2	Dimension of SLR specimen for UCS testing.....44
3.3	Test results of VTF samples.....44
3.4	Test results of SLR samples.....47
3.5	Dimension of VTF specimen for DS testing.....50
3.6	Dimension of SLR specimen for DS testing.....50
3.7	DS test results of VTF.....52
3.8	DS test results of SLR.....52
3.9	Summarize shear strength parameters of VTF and SLR.....53
3.10	Dimensions of soil samples.....56
3.11	Test results of soil samples.....57
3.12	Summarize shear strength parameters of VTF and SLR.....58
4.1	Summary mechanical properties from laboratory testing.....59
4.2	Parameters used in UDEC simulations.....62

LIST OF FIGURES

Figure		Page
1.1	Methodology of research.....	3
2.1	Phu Bia Mining location map, Lao PDR.....	7
2.2	Geology of study area for pre-mining topography (Tate, 2005).....	8
2.3	Lithology of Phu Kham mine site.....	10
2.4	Typical VTF cores with characteristic foliation, local folding and quartz.....	11
2.5	Typical SCG fresh cores with characteristic coarse grains and clasts.....	12
2.6	Typical SLR cores with characteristic bedding.....	12
2.7	Typical SLS cores with characteristic foliation, local folding and carbonate.....	13
2.8	Typical IDI cores with characteristic weak foliation and quartz veins.....	14
2.9	Typical IGN fresh cores with joints.....	14
2.10	Broad structural domains at 560m RL (King 2015, after Tate 2005).....	16
2.11	South wall fault network; $\pm 25\text{m}$ slice 450mRL level plan.....	17
2.12	South wall cross section $\pm 5\text{m}$ slice.....	18
2.13	Drill cores showing South Thrust in VTF, intense foliation development and clay alteration.....	19
2.14	Drill cores showing Splay in VTF: foliation and clay alteration, in SLS carbonaceous shears.....	20
2.15	Drill cores showing Splay fault in SLR with several quartz veins and cleavage.....	20
2.16	Black Fault 16, faulted contact between VTF and IGN with clay alteration.....	21
2.17	Black Fault 16 with black, clayey matrix supported fault breccia in VTF.....	21
2.18	South Wall SLR Fault 07 presenting a clay gouge core, disjunctive cleavage.....	22
2.19	Plane failure (Wyllie and Mah, 2005).....	25
2.20	Wedge failure (Wyllie and Mah, 2005).....	25

LIST OF FIGURES (Continued)

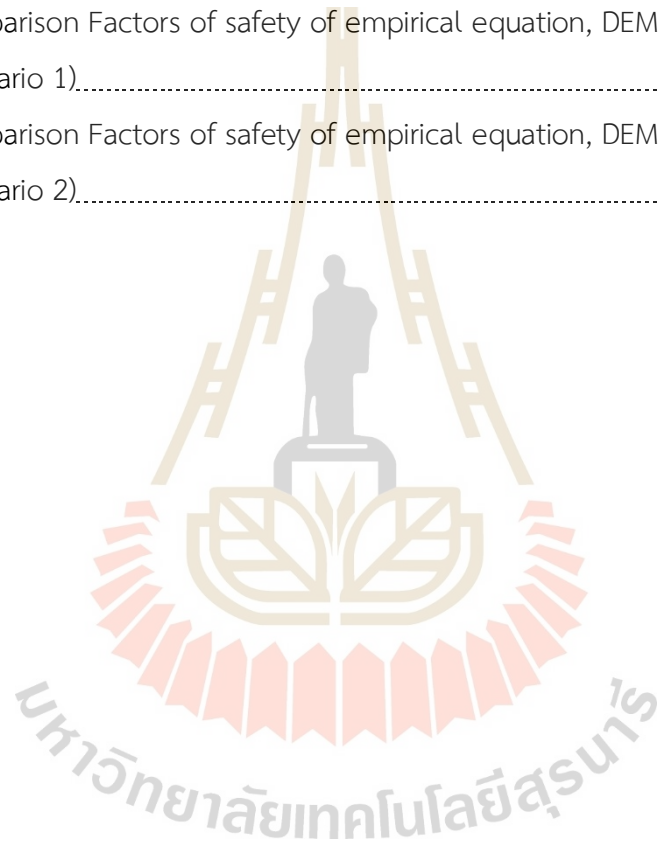
Figure	Page
2.21 Toppling failure: (a) block toppling, (b) flexural toppling and (c) block flexural toppling (Wyllie and Mah, 2005).....	26
2.22 Circular failure (Wyllie and Mah, 2005).....	26
2.23 Large scale structures in 3DEC model (Severin et al., 2013).....	30
2.24 Horizontal and total displacement in 3DEC model (Severin et al., 2013).....	30
2.25 Displacement vectors distribution (Deliveris et al., 2016).....	32
2.26 Plastic regions propagation. (Deliveris et al., 2016).....	33
2.27 Effects of slope height and angle on factor of safety (Igwe and Chukwu, 2018)....	36
2.28 Relationship between shear strength parameters and factor of safety (Igwe and Chukwu, 2018).....	37
3.1 Borehole location in the study area.....	39
3.2 VTF core samples.....	40
3.3 SLR core samples.....	40
3.4 Fault samples.....	41
3.5 Uniaxial compressive strength test frame.....	42
3.6 Some VTF (a) and SLR (b) specimens prepared for UCS testing.....	42
3.7 Post-test VTF (a) and SLR (b) specimens of UCS testing.....	42
3.8 Some stress-strain curves of uniaxial compression test (VTF).....	45
3.9 Some stress-strain curves of uniaxial compression test (SLR).....	45
3.10 Direct shear test frame.....	48
3.11 Some VTF (a) and SLR (b) specimens prepared and moulded for DS testing....	49
3.12 Some VTF (a) and SLR (b) specimens after DS testing.....	49
3.13 Some stress-displacement relationships of DS test (VTF).....	51
3.14 Some stress-displacement relationships of DS test (SLR).....	51
3.15 Shear strength of VTF.....	54
3.16 Shear strength of SLR.....	54

LIST OF FIGURES (Continued)

Figure	Page
3.17 Direct shear tests frame for three-ring mold.....	55
3.18 Soil samples before testing.....	56
3.19 Soil samples after testing.....	57
3.20 Shear strength of fault.....	57
4.1 Boundary conditions and geometry of the representative slope model.....	60
4.2 Mesh model.....	61
4.3 Displacement vectors (a), shear strains and factor of safety (b) of slope face angle 30°	63
4.4 Displacement vectors (a), shear strains and factor of safety (b) of slope face angle 90°	64
4.5 Factors of safety as a function of slope angle.....	65
4.6 Displacement vectors (a), shear strains and factor of safety (b) of distance between fault and crest is 25 m.....	66
4.7 Displacement vectors (a), shear strains and factor of safety (b) of distance between fault and crest is 125 m.....	67
4.8 Factors of safety as a function of distance between fault and slope crest (X).....	68
4.9 Displacement vectors (a), shear strains and factor of safety (b) of fault angle 40 degrees.....	69
4.10 Displacement vectors (a), shear strains and factor of safety (b) of fault angle 80 degrees.....	70
4.11 Factors of safety as a function of fault angle.....	71
4.12 Displacement vectors (a), shear strains and factor of safety (b) of c_{hang} 0.01 MPa... 72	72
4.13 Displacement vectors (a), shear strains and factor of safety (b) of c_{hang} 2.00 MPa.....	73
4.14 Displacement vectors (a), shear strains and factor of safety (b) of ϕ_{hang} 22.5 degrees.....	74
4.15 Displacement vectors (a), shear strains and factor of safety (b) of ϕ_{hang} 35.0 degrees.....	75

LIST OF FIGURES (Continued)

Figure		Page
4.16	Factors of safety as a function of hanging wall friction angle (ϕ_{hang}) Various cohesion of hanging rock (c_{hang}).....	76
4.17	Predicted FS as a function of $\phi_{\text{hang}} \cdot \alpha / \phi_{\text{flt}} \cdot \psi$ under various $c_{\text{hang}}/c_{\text{flt}}$	77
5.1	Comparison Factors of safety of empirical equation, DEM, LEM, and FEM (Scenario 1).....	80
5.2	Comparison Factors of safety of empirical equation, DEM, LEM, and FEM (Scenario 2).....	81



LIST OF ABBREVIATIONS

c	=	Cohesion
D	=	Diameter of specimen
E	=	Elastic modulus
flt	=	Fault
FS	=	Factor of safety
hang	=	Hanging wall
L	=	Length of specimen
W	=	Weight of specimen
X	=	Distance between fault and crest of slope
a	=	Fault angle
f	=	Friction angle
y	=	Slope face angle
n	=	Poisson's ratio

CHAPTER I

INTRODUCTION

1.1 Background and rationale

Rock slope stability is considered crucial for safety in engineering project areas, such as open pit mine, dam embankment, road cut, and railway. Slope failure is controlled by rock mass characteristics, slope geometries, groundwater and other operating conditions. Geology comprehension is necessary for rock slope design. In the mining process, small changes in the slope face angle may have large consequences to the mining operation economy.

Phu Kham open pit mine is the largest copper reserve in Laos, which is located in PanAust's Phu Bia Mining Contract Area, Xaisomboun Province, Lao PDR. A problem of Phu Kham open pit is slope instability at the South Wall. This location has specific discontinuities that lead to the decrease of slope stability. To prevent slope failures, several methods have been proposed by researchers. Empirical method or rock mass classification system is often used for preliminary evaluation of rock mass behaviors (Basahel and Mitri, 2017). It is simple and convenient to use. Numerical method is used for a more complex slope geometry and failure mechanisms. It is useful when the other methods cannot represent rock mass behaviors (Wyllie and Mah, 2005; Romer and Ferentinou, 2019). Even though the empirical methods have been proposed by many researchers to quantify rock mass behavior, the effort of rock mass classification for specific pit slope design of Phu Kham open pit has rarely been attempted. To correlate the shear strength parameters with the rock slope behavior, empirical equation for predicting the Factor of Safety (FS) are needed. Such equation can be readily applied, and hence allows a quick excavation and production of the ore.

1.2 Research objectives

The main objective of this study is to determine rock shear strength parameters of fault and shear zone at South Wall of Phu Kham open pit mine by direct shear testing. The laboratory results are demonstrated in numerical models with a distinct element method using UDEC code (Itasca, 2011). The numerical results are used to develop mathematical relationships between shear strength parameters under different factors of safety.

1.3 Scope and limitations

The scope and limitations of the study include as follows.

- 1) This study involves field observation on the geological engineering from rock slope open pit at Phu Kham mine site, Laos.
- 2) Representative slope locations from South Wall of Phu Kham open pit are emphasized.
- 3) Uniaxial compressive strength test is carried out on cylindrical specimens of volcanic tuff (VTF) and Red Beds (SLR) with a nominal diameter of 61 mm and L/D ratio between 2.0 to 2.5 are axially loaded to failure. The laboratory testing procedure strictly follows ASTM D7012-14 standard.
- 4) Direct shear test is conducted on nominal specimens with 100 mm diameter obtained from VTF, SLR and faults in South Wall. Direct shear test methodology and calculation follow ASTM D5607-08 standard.
- 5) UDEC5.0 (Itasca, 2011) software are used in numerical simulations.
- 6) Slope face angles in numerical simulation are varied from 30° to 90° with 10° increment. Slope heights are maintained constant at 100 m. The distance between fault and crest varies from 25, 50, 75, 100 to 125 m. Fault angles are varied from 40°, 50°, 63°, 70° and 80°. Cohesion of hanging wall varies from 0.01, 0.05, 0.10, 0.15, 0.20, 0.30, 0.50, 1.00 and 2.00 MPa. Friction angle of hanging wall varies from 22.5°, 25.0°, 28.4°, 30.0°, 32.5° and 35.0°

1.4 Research methodology

The methodology of research comprises 6 steps; including literature review, sample preparations and laboratory testing, numerical simulations, mathematical relationship development, discussions and conclusions, and thesis writing (Figure 1.1).

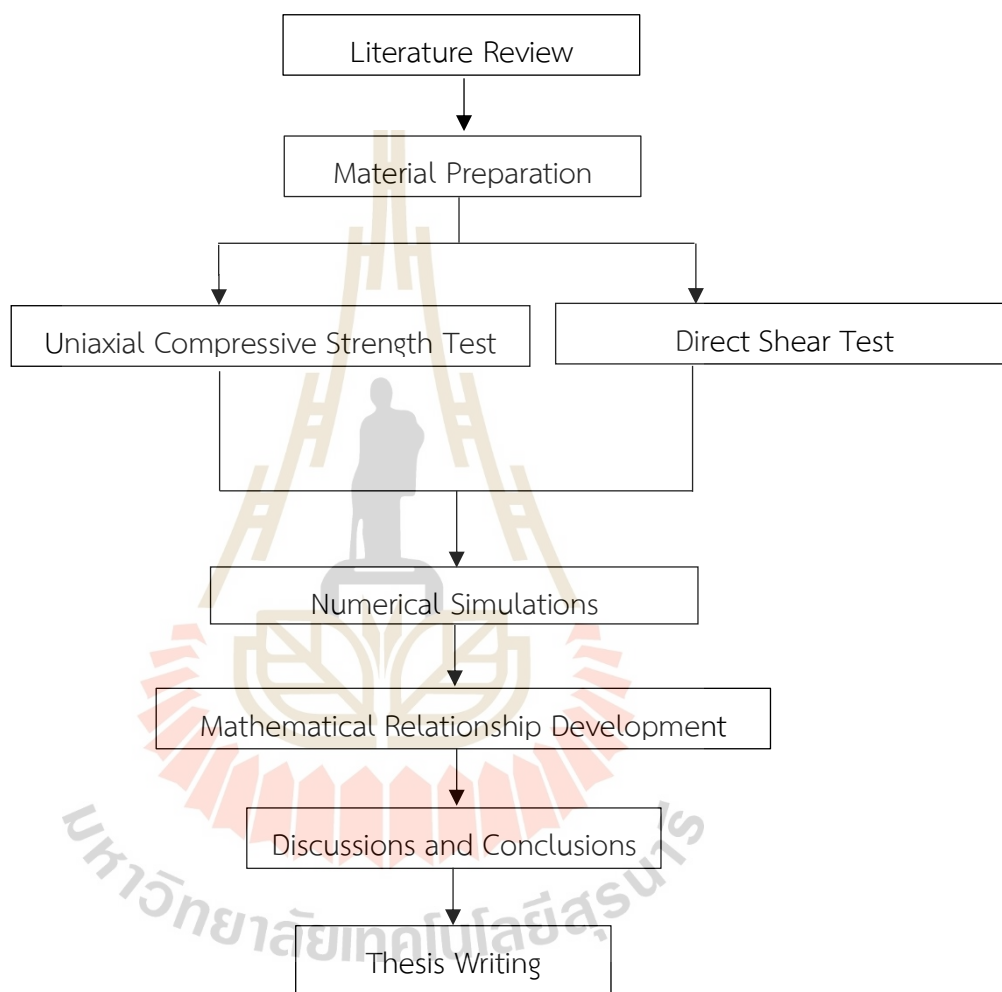


Figure 1.1 Research methodology

1.4.1 Literature review

Literature review is performed to study research on slope stability of Phu Kham open pit mine, sources of information are from journals, reports, conference papers and books. A summary of literature reviews is given in this study.

1.4.2 Sample preparation and laboratory testing

Rock and soil samples have been obtained from the South Wall zone in the Phu Kham pit. Three types of samples are used in this study, they are volcanic tuff (VTF), Red Beds (SLR). The VTF and SLR, and fault are represented as hanging wall, footwall, and major fault respectively.

All samples are collected from diamond drill cores. There are three groups of sample preparation for different test methods: 1) uniaxial compressive strength tests (UCS), 2) direct shear tests of rock specimens on rough fracture (DS), and 3) direct shear tests of soil samples (DS- soil). The core specimens with a nominal diameter 61 mm (HQ bit size) tested here are drilled from depths ranging between 15.50 and 183.40 m.

1.4.3 Numerical simulations

Discrete element analyses are performed using UDEC (Itasca, 2011) to demonstrate the slope stability behavior. The discrete element models are performed to represent various slope face angles and distances between fault and crest. The models use mechanical properties obtained from the laboratory testing.

1.4.4 Development of mathematical relationships

The results from the numerical simulations are used to develop mathematical equation between the shear strength parameters with slope characteristics and factor of safety.

1.4.5 Discussions and conclusions

All study methods, and results are documented and incorporated in the thesis. The research is published in the conference proceedings or journals.

1.5 Thesis Contents

This thesis is separated into five chapters. Chapter I explains the objectives, problems and rationale, and methodology of research. Chapter II presents results of

the literature review to improve the knowledge of slope stability and shear strength properties. Chapter III describes sample preparations, test methods and test results. Chapter IV describes the numerical model method, boundary condition to simulate and mathematical relationships. Chapter V concludes the results, discussions, conclusions and recommendation for future studies.



CHAPTER II

LITERATURE REVIEWS

2.1 Geology and lithology of Phu Kham site

2.1.1 Geology

The Phu Kham Copper-Gold Operation (PKM) is the largest copper reserve in Laos, which located in PanAust's Phu Bia Mining Contract Area, Xaisomboun Province, Lao PDR, approximately 140 km north of Vientiane (Figure 2.1). The Copper-Gold PKM deposit is described as a porphyry-skarn ore system, believed to be of Late Triassic, related to subduction and island arc magmatism associated with the Loei and Truongson fold-thrust belts. Alteration and mineralisation extend over approximately 2 km in an arcuate zone approximately 500 m wide. The ore body is hosted by muscovite schist and narrow zones of skarn, inferred to have originated as quartz diorite and impure limestones. Copper mineralisation is predominantly chalcopyrite, both in skarn and disseminated porphyry-style.

Above the paleo-water table, copper is mostly leached from skarn and stockwork mineralisation. The resulting oxide profile has a gold only signature in which skarns are converted to gossans. Intense Himalayan tectonism (approximately 45 Ma) has resulted in penetrative schistose and phyllitic fabrics in previously sericite-altered rocks and small-scale folding and spaced cleavage development in limestones. Surface geology (on the topography prior to mining) is shown in Figure 2.2.

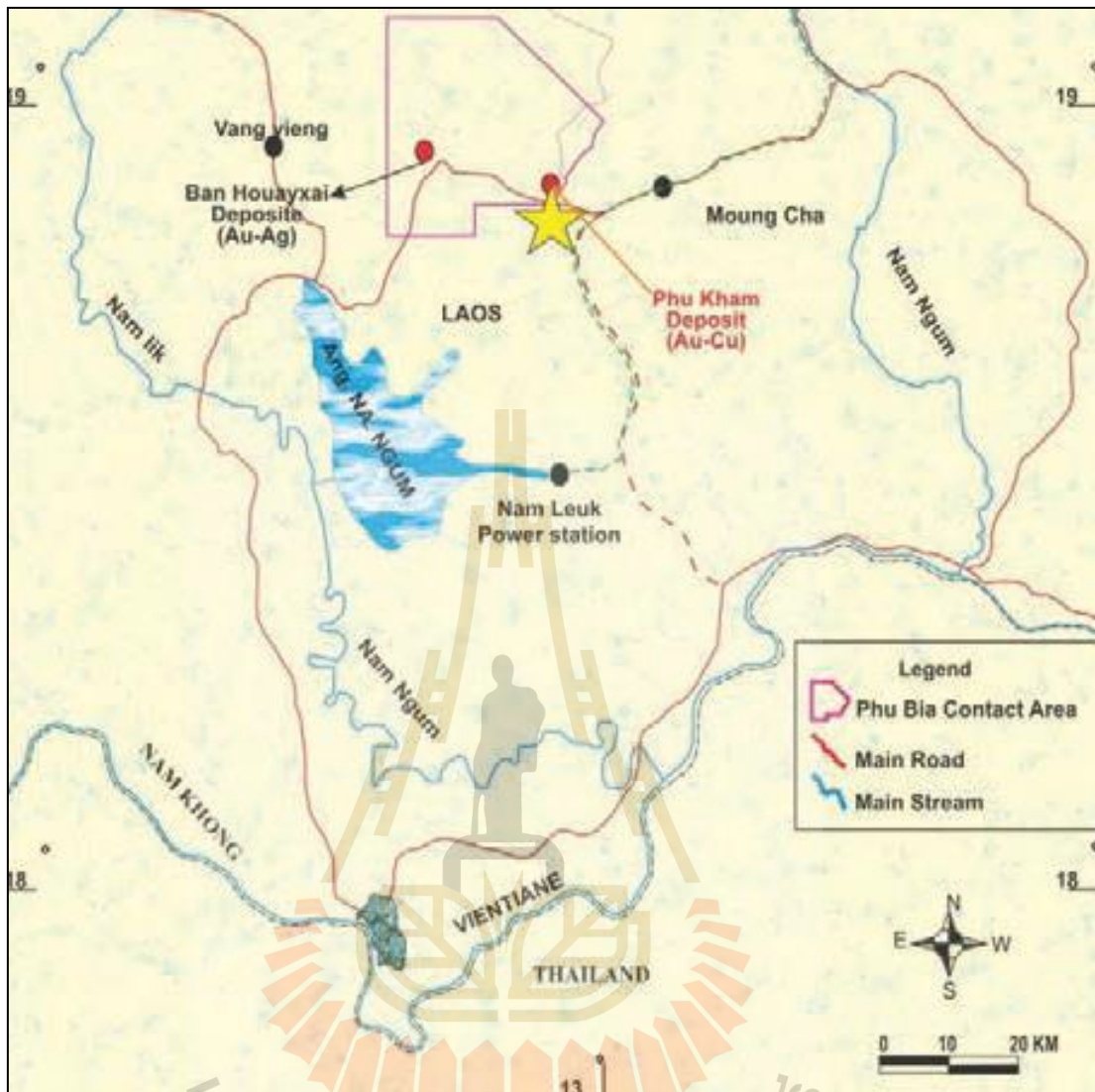


Figure 2.1 Phu Bia Mining location map, Lao PDR.

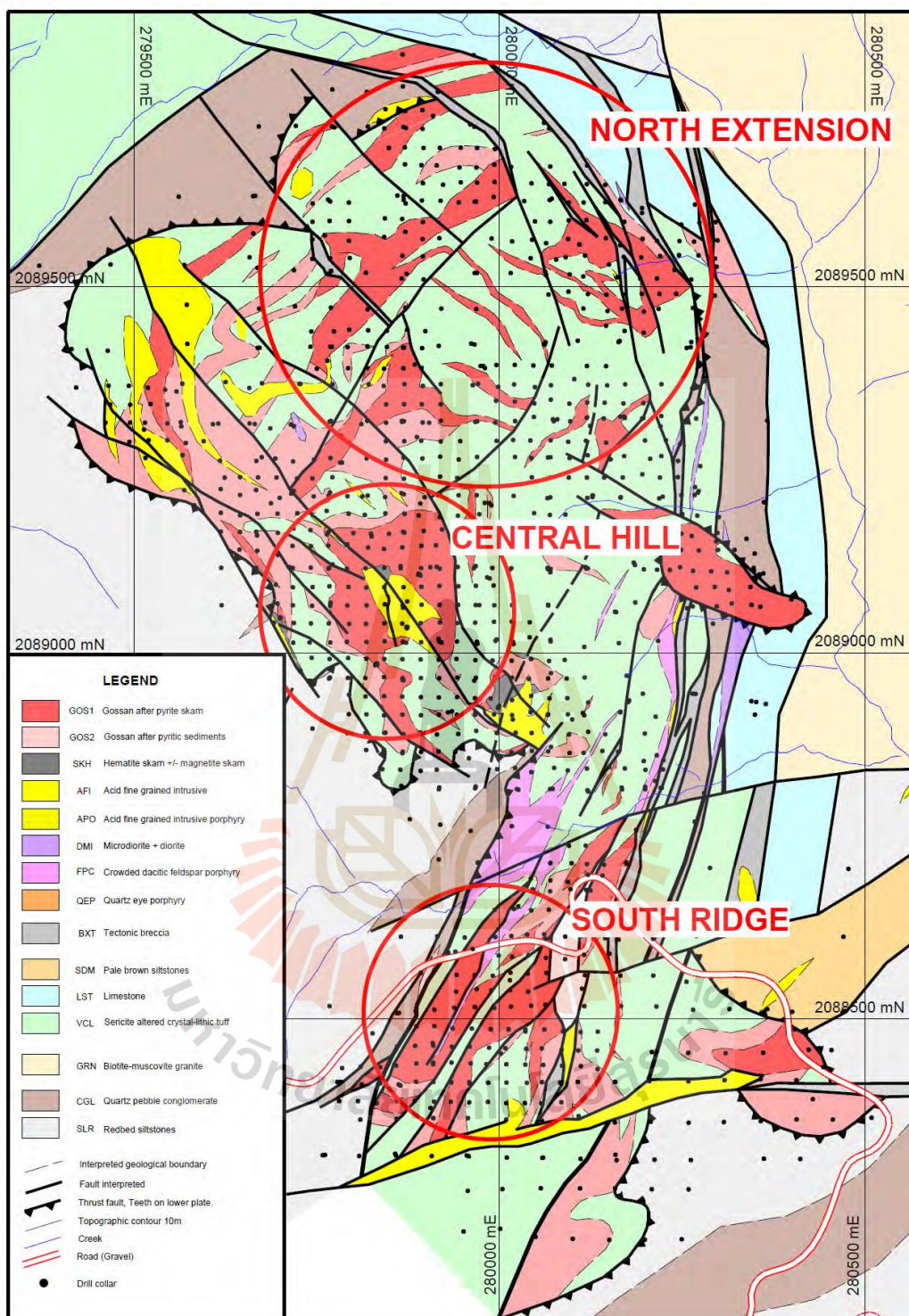


Figure 2.2 Geology of study area for pre-mining topography (Tate, 2005).

The following lithological units are present:

Granite of Silurian-Ordovician age in an elliptical body approximately 4x5 km in the north-east, mainly homogeneous.

Limestone of Permo-Carboniferous age. Carbonaceous siltstone known as “black shale”, associated with the limestone.

Interbedded calcareous siltstone-sandstone correlated to the Late Triassic Nam Phong Formation, which is the basal unit of the Korat Group.

Siltstone “Red Beds” belonging to the Late Cretaceous part of the Korat Group

Andesitic lapillic tuffs derived from Late Permian-Late Triassic island arc magmatism.

Diorite intrusions which post-date the Red Beds and were associated with faulting

2.1.2 Lithology and weathering domains

Major rock types exposed on PKM design, as per the provided block model, are illustrated in Figure 2.3.

1) Tuff (VTF)

The VTF rock mass (Figure 2.4) is exposed in the lower southern slopes of the southern extension, and the lower northern slope. The rock mass is foliated and is expected to behave anisotropically. The direction of foliation is highly variable in the southern region of the mine, due to several major structures intercepting the rock mass.

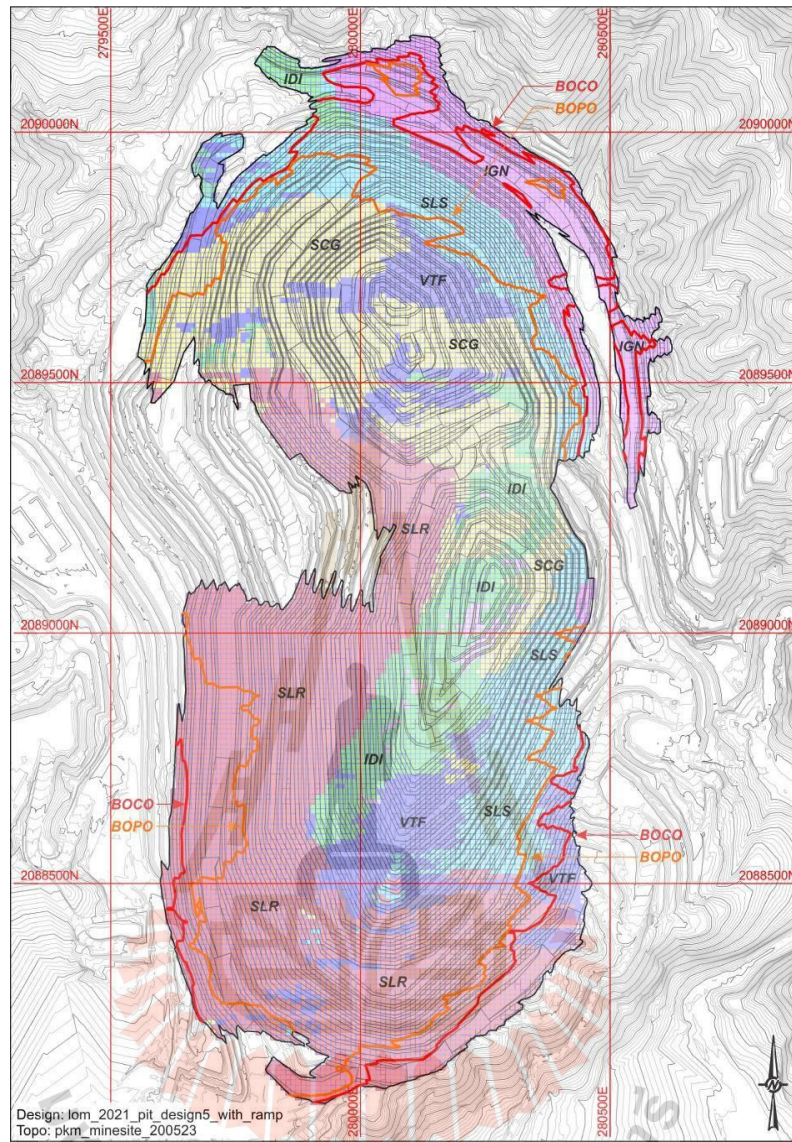


Figure 2.3 Lithology of Phu Kham mine site.

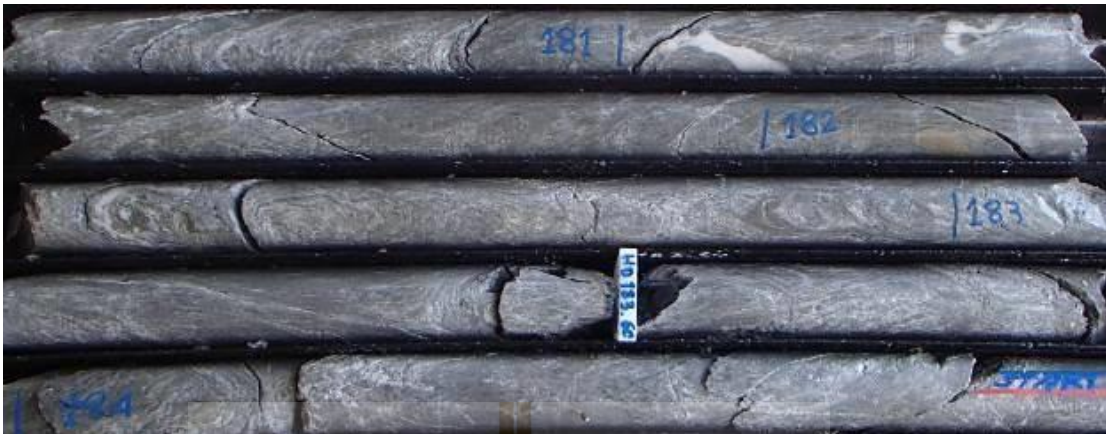


Figure 2.4 Typical VTF cores with characteristic foliation, local folding and quartz.

The VTF rock mass away from fault induced degradation is expected to be of good quality, with rock mass rating index (σ) proposed by Bieniawski (1989) of between 60 to 80.94% of the recovered core has been logged as fresh. It is expected that large scale shearing through the competent VTF blocks are unlikely. However, blocks of fault bounded VTF may form unstable wedges, particularly within the southeastern slopes.

2) Conglomerate (SCG)

The conglomerate (Figure 2.5) is exposed in the north-western wall of Phu Kham mine site, and in parts of the lower central and eastern walls. It is expected that this material will form a competent slope toe and control slope scale instability. The conglomerate is expected to behave isotropically and be of good quality, with RMR89 greater than 60. 87% of the recovered core has been logged as fresh.

3) Red beds (SLR)

The SLR rock mass (Figure 2.6) will be critical for stability analysis of the western slopes for the design, as well as the eastern slopes if the unconstrained design is mined. The SLR rock mass is bedded and is expected to behave anisotropically. The bedding is expected to be undulating at a multi-bench scale, with several bedding shears dispersed throughout the unit. The bedding is expected to be moderately dipping into the mine and may form basal sliding surfaces for slope instability. The SLR rock mass is expected to be of good quality, with most of the interval RMR89 being

between 60 to 70.96% of the recovered core has been logged as fresh. It is expected that large scale shearing through the competent SLR blocks will be unlikely and failure may occur in the direction of bedding, with minor breakout at the slope toe.

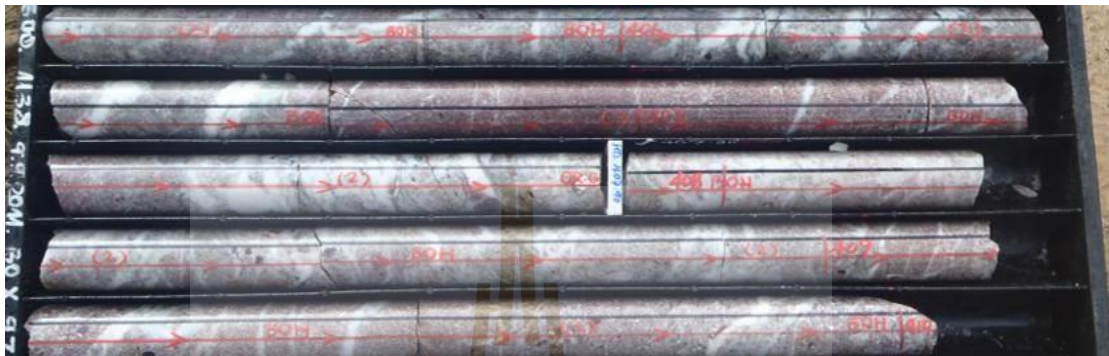


Figure 2.5 Typical SCG fresh cores with characteristic coarse grains and clasts.



Figure 2.6 Typical SLR cores with characteristic bedding.

4) Limestone (SLS)

The SLS rock mass (Figure 2.7) is exposed in the upper south-eastern, and central northern slopes. Like the VTF, the SLS rock mass is foliated and is expected to behave anisotropically. The direction of foliation is highly variable due to several major structures intercepting the rock mass. The SLS rock mass is expected to be of good quality, with RMR89 of between 60 to 70.99% of the recovered core has been logged as Fresh. It is expected that large scale shearing through the competent SLS blocks

will be unlikely. However as with the VTF material, blocks of fault bounded SLS may form unstable wedges, particularly within the south-eastern slopes.



Figure 2.7 Typical SLS cores with characteristic foliation, local folding and carbonate.

5) Diorite (IDI)

The IDI rock mass (Figure 2.8) is exposed in the lower central and western slopes of the southern part of PKM Design. The diorite is expected to be foliated and to behave anisotropically. The foliation is highly variable through the center of the deposit due to several major structures intercepting the region. However, the foliation of the diorite is not expected to be orientated parallel to the slopes and will not form a basal sliding plane. The IDI rock mass is expected to be of good quality, with RMR89 of between 60 to 70.99% of the recovered core has been logged as Slightly Weathered to Fresh. Similar to SLS and VTF, it is expected that large scale shearing through the competent IDI blocks will be unlikely. However, blocks of fault bounded IDI may form unstable wedges, particularly within the south-eastern slopes.

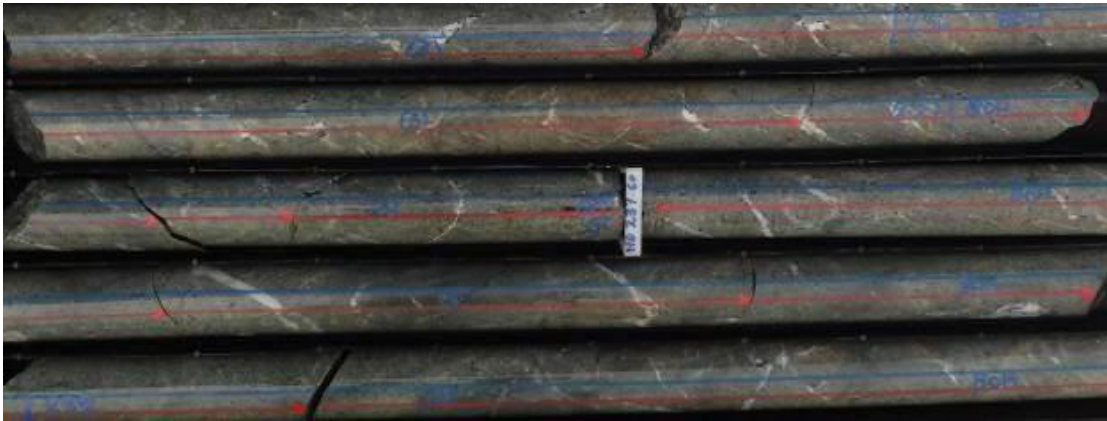


Figure 2.8 Typical IDI cores with characteristic weak foliation and quartz veins.

6) Granite (IGN)

The upper half of the north eastern slope of PKM Design is formed within the granite rock mass (Figure 2.9). It is expected that this material will be important for slope stability both above and below the Nam San Channel. 19% of the total recovered core. It is expected that this region will mostly be formed within soil and weathered sediments, with low strengths limiting the achievable slope angle. The granite is foliated and is expected to behave anisotropically.



Figure 2.9 Typical IGN fresh cores with joints.

The direction of foliation is favorable for the northern wall stability, dipping into the slope. The rock mass is fair to good quality, with RMR89 of between 40 and 70.74% of the recovered core has been logged as slightly weathered or fresh. It is

expected that large scale instability of the north wall will require shearing through the granite rock mass, across the foliation.

2.1.3 Structural geology in Southern Walls

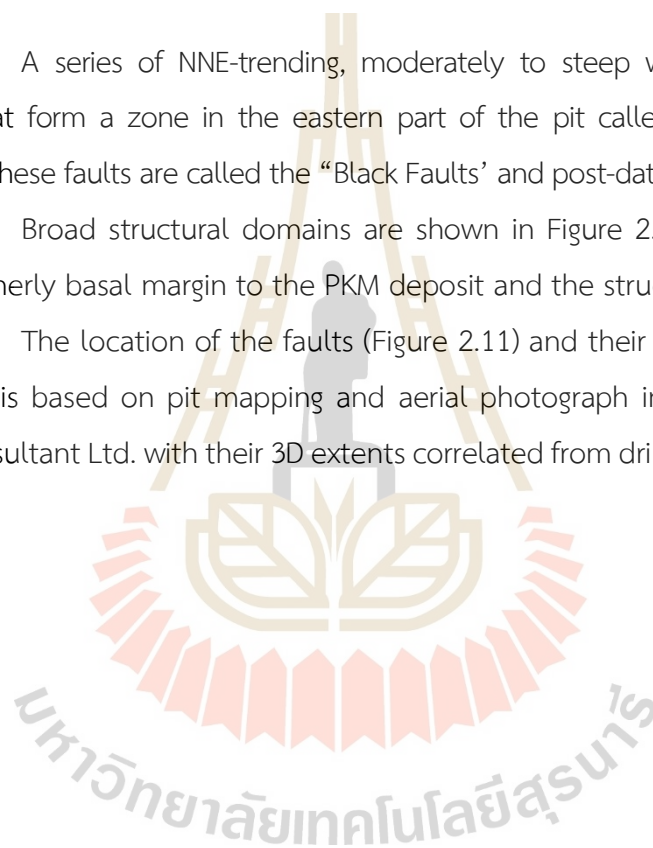
The structural architecture in the south of the PKM design is distinguished by two main structural elements:

A network of shallow to moderate NNW-dipping, NE-trending faults which include the South Thrust Fault and their splays, the East Faults and the South Wall SLR faults.

A series of NNE-trending, moderately to steep west-dipping, strike-slip structures that form a zone in the eastern part of the pit called the “Blocks Zone”. Collectively, these faults are called the “Black Faults’ and post-date and offset the thrust.

Broad structural domains are shown in Figure 2.10. The South Thrust forms a southerly basal margin to the PKM deposit and the structural domains.

The location of the faults (Figure 2.11) and their cross-cutting relations (Figure 2.12) is based on pit mapping and aerial photograph interpretation by Solid Geology Consultant Ltd. with their 3D extents correlated from drilled hole photography and logging.



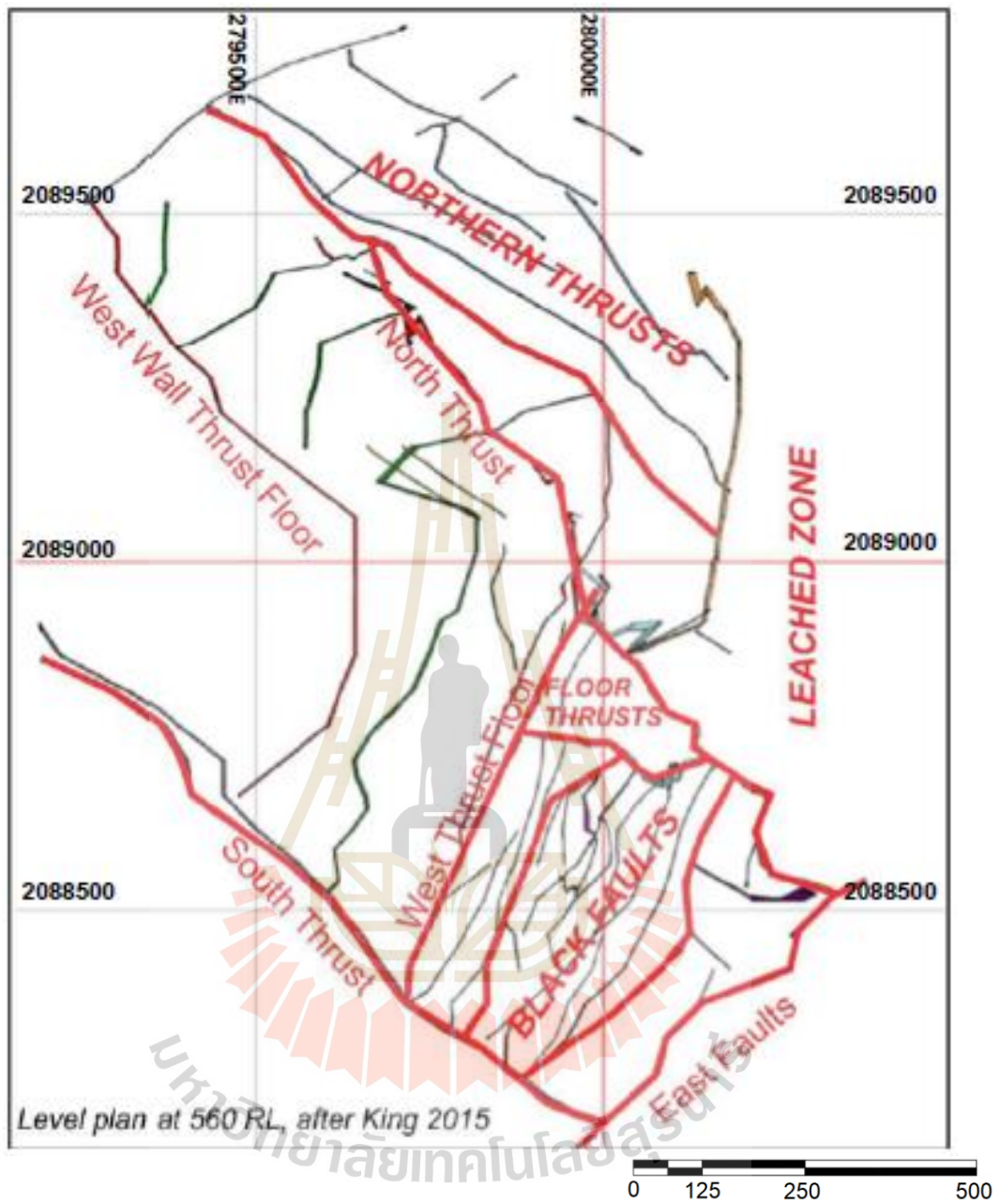


Figure 2.10 Broad structural domains at 560m RL (King, 2015, after Tate, 2005).

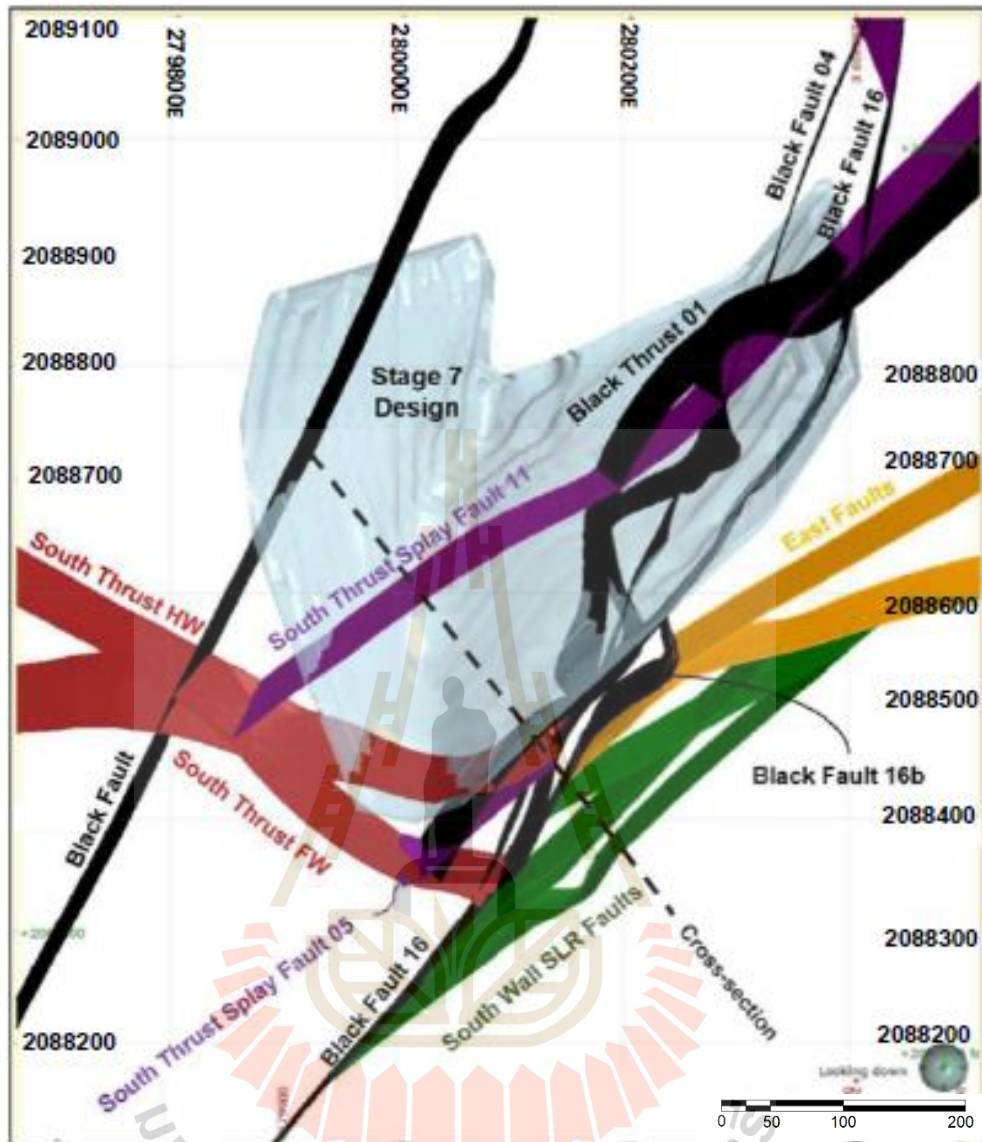


Figure 2.11 South wall fault network; $\pm 25\text{m}$ slice 450mRL level plan.

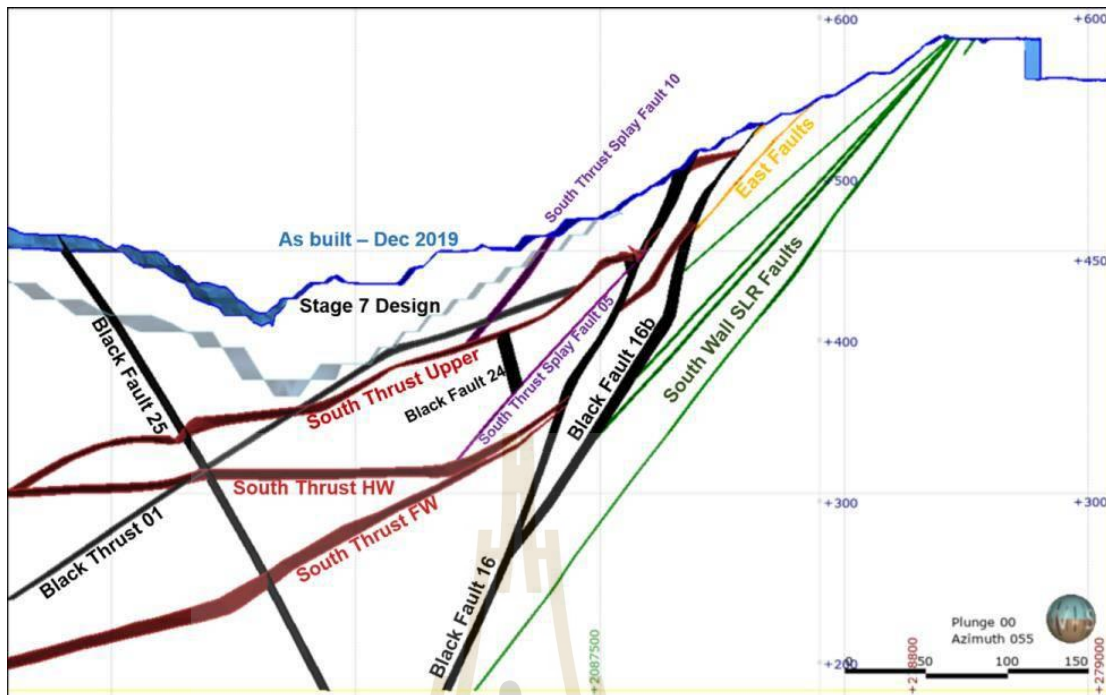


Figure 2.12 South wall cross section $\pm 5\text{m}$ slice (location shown in Figure 2.11).

7) South Thrust System

In the south wall, the South Thrust System includes a series of NW-striking thrusts faults that includes 'South Thrust Hanging Wall (HW) and Foot Wall (FW)', 'South Thrust Upper', 'East Fault Upper' and 'East Fault Segment'. These faults have the largest displacements in the system and often have strong foliation parallel to them. Steeper, secondary thrust faults emerge from, and link between, the larger thrust fault forming duplexes to collectively form a south vergence thrust system. The thrust system is bound by the South Thrust HW and FW faults (South Thrust) that form the footwall floor thrust, while the hanging wall roof thrust is mapped as a series of undulating roof thrusts included in the south wall, the South Thrust Upper (Figure 2.12).

In the south wall, the South Thrust undulates in and out of the SLR and roughly divides the SLR in the footwall from the VTF-IDI-SLS in the hanging wall.

The basal South Thrust has an anastomosing geometry with fluctuating separation between the HW and FW fault planes, that can extend to as much as 6m, or merge into a single zone. This produces a variability in the thickness of the intensely foliated rock mass characteristic of the fault zone (Figure 2.13).

The character and thickness of the shear zone is dictated by the mechanical properties of the inter-fault lithology. Maximum thickness and intense foliation development are observed within the softer altered volcanics and diorite units while the stiffer limestone is folded and appears boudinage into blocks that deflect deformation to their margins, forming smaller carbonaceous shears (Figure 2.14). The South Thrust develops a broader, more complex geometry of smaller (in extent) thrust splays as it approaches the steep Black Fault zone to the east (Figure 2.14 and 2.15).

The array of thrust splays link into the Black Faults implying they were active at the same time. Only Black Fault 16 offsets the South Thrust suggesting other Black Faults maybe using the South Thrust as a differential movement plane with minimal <10 m offset anticipated. The East Faults are interpreted as truncated and offset continuations of the South Thrust across the strike-slip Black Fault 16. Both faults have similar morphologies with very characteristic, strongly deformed, limestone sheared into them, and the South Thrust seems to be rotating towards the East Faults at depth.



Figure 2.13 Drill cores showing South Thrust in VTF, intense foliation development and clay alteration.

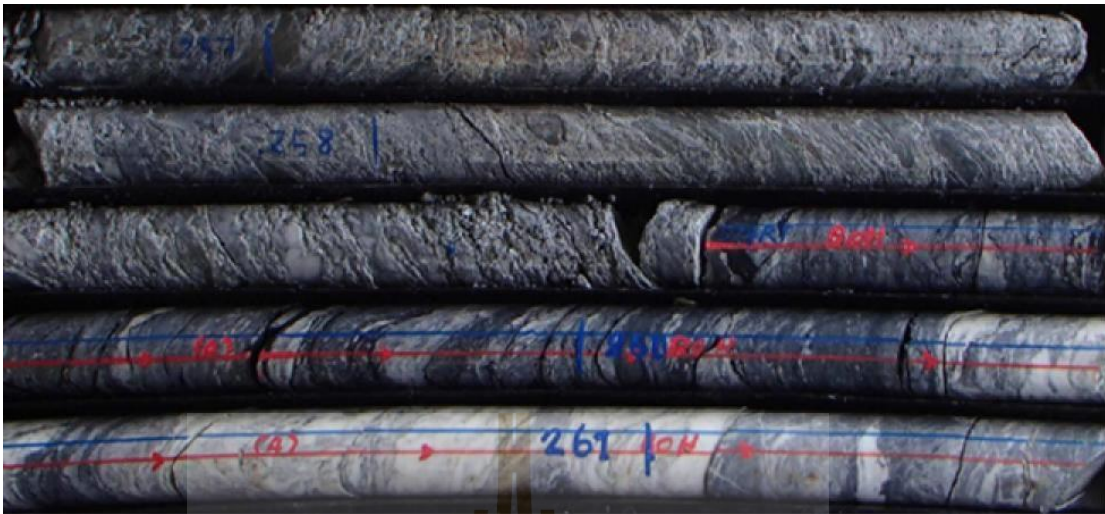


Figure 2.14 Drill cores showing Splay in VTF: foliation and clay alteration, in SLS carbonaceous shears.



Figure 2.15 Drill cores showing Splay fault in SLR with several quartz veins and cleavage.

8) Black Faults

The 'Block Zone' is a series of fault-bound blocks and slices developed between the 'Black Fault' in the west and the 'Black Fault 16' in the east (Figure 2.11). The Black Fault 16 is a steep zone of brittle-ductile deformation characterized by variable, lithology controlled, thicknesses of brittle fractures and black (carbonaceous)

clayey gouge (Figures 2.16 and 2.17). Black Fault 16 appears to be the youngest major structure as it offsets the South Thrust – East Faults in a lateral sense. Strike-slip movement initiates an apparent dextral offset of the ‘Granite fault 01’ thrust contact to the Silurian Granite in the north, but an apparent sinistral offset of the South Thrust – East Faults in the south; this apparent inconsistency is probably related to the difference in dip of the two surfaces.

Black Fault 16b is interpreted as a FW splay to Black Fault 16 and may utilize a steeply dipping zone of black, gouge-like clays with brecciated clasts to return to Black Fault 16 (Figures 2.11 and 2.12).



Figure 2.16 Black Fault 16, faulted contact between VTF and IGN with clay alteration.



Figure 2.17 Black Fault 16 with black, clayey matrix supported fault breccia in VTF.

9) South Wall SLR Faults

The steep dipping South Wall SLR faults are characterized by zones of quartz veins, strong disjunctive cleavage and/or bedding parallel clayey gouge (Figure 2.18). These structures have likely contributed to several failures within the weathered material of the south wall during 2017 and 2018.

An approximately 20 m wide central zone of strong deformation comprising a broad zone of stranded shears is bound by the upper South Wall SLR Fault 08 and the lower South Wall SLR Fault 07 (Figure 2.12). Where the South Thrust intersects the South Wall SLR Faults, moderately to strongly jointed/fractured zones and quartz veins have developed.



Figure 2.18 South Wall SLR Fault 07 presenting a clay gouge core, disjunctive cleavage.

2.2 Joint shear strengths

Rock mass is anisotropic, heterogeneous and discontinuous materials. In realistic, the rock slope stability assessment is necessary estimated rock mass shear resistance both along potential shear plane and along weakest discontinuity. The rock joint shear strength is influenced by the joint surface roughness and nature of joint material. Several researchers attempt have been to verify these effects. Most of attempts based on laboratory testing to derive the empirical parameters or on numerical simulations.

Patton (1966) evaluate the joint roughness by defining the dilation angle and develop rock joint shear strength equation (Equation 2.2) based on Coulomb friction criteria (Equation 2.1) as follows:

$$\tau = c + \sigma_n \tan \phi \quad (2.1)$$

where τ is shear strength, c is cohesion, σ_n is normal stress and ϕ is friction angle.

$$\tau = c + \sigma_n \tan(\phi_b + i) \quad (2.2)$$

where i is regular teeth inclination and ϕ_b is basic friction angle.

Ladanyi and Archambault (1970) study the model of the rock joint shear strength, defining that two modes of failure occur simultaneously. However, that model is good and excellent idea, but it is difficult to define the parameters used (Equation 2.3) as follows:

$$\tau = \frac{\sigma_n (1 - a_s)(V + \tan \phi) + a_s \cdot \tau_r}{1 - (1 - a_s)V \tan \phi_B} \quad (2.3)$$

where τ_r is intact material shear strength, a_s is the discontinuity surface proportion when sheared through projections of intact material and V is dilation rate at peak shear strength.

Barton (1973) studies joint roughness and strength, it represents in term of the joint roughness coefficient (JRC). Barton proposes an empirical equation (Equation 2.4), that modified from Patton's equation. This criterion has some constraints for used.

Barton and Choubey (1977) suggest that the peak shear strength curves should be had maximum allowable shear strength given by $\tan^{-1}(\tau/\sigma_n) = 70$ degrees for designing purposes. Barton's law is only valid when joint wall is in rock-to-rock contact. Hoek and Bray (1981) state that the Barton criterion is valid when normal stress as $0.01 < (\sigma_n/JRC) < 0.3$.

$$\tau = \sigma_n \tan[\phi_b + JRC \log_{10}(JCS/\sigma_n)] \quad (2.4)$$

where JCS is joint wall compressive strength.

Grasselli and Egger (2003) provide the rough joint shear strength equation based on three-dimensional surface characterization. (Equation 2.5). This equation based on few experimental strength data.

$$JRC = [\tan^{-1} [\tan\phi_r^*(1+g)] - \phi_b] / [\log_{10}(\sigma_c / \sigma_n)] \quad (2.5)$$

where ϕ_r^* is residual friction angle.

2.3 Rock slope stability and rock mass classification

2.3.1 Slope failure modes

Hoek and Bray (1981) classify modes of slope failure as

1) Plane failure

Plane failure occurs when bedding planes or joint planes strike or nearly parallel to slope face (within approximately ± 20 degrees). The sliding plane must daylight in the slope face that indicates the plane dip angle (ψ_p) is smaller than the slope face angle (ψ_f). Furthermore, the plane dip angle be greater than the plane friction angle (ϕ), as shown in Figure 2.19.

2) Wedge failure

Wedge failure occurs when two discontinuity planes strike obliquely opposite the slope face where wedge takes place along the intersection line of two planes. The intersection line daylights in the slope face, plunge of the intersection line (ψ_i) is flatter than the slope face angle (ψ_f) and larger than the rock internal friction angle (ϕ), as illustrated in Figure 2.20.

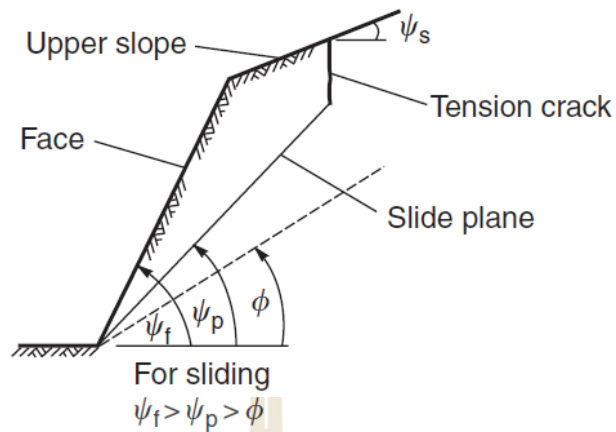


Figure 2.19 Plane failure (Wyllie and Mah, 2005).

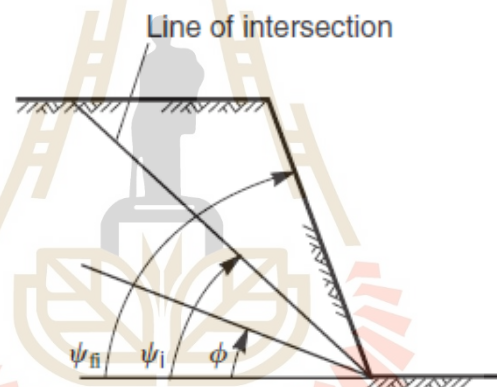


Figure 2.20 Wedge failure (Wyllie and Mah, 2005).

3) Toppling failure

Toppling failure occurs when columns of rock, formed by steeply dipping discontinuities in the rock rotates about an essentially fixed point at or near the base of the slope followed by slippage between the layers. Toppling failure be further categorized to three modes: block toppling, flexural toppling and block-flexural toppling (Figure 2.21).

4) Circular failure

The rock body is defined as a discontinuous rock mass. Circular failure occurs when the individual particles in rock mass or soil are very small compared with the slope size, then broken rock or soil fail in a circular mode (Figure 2.22).

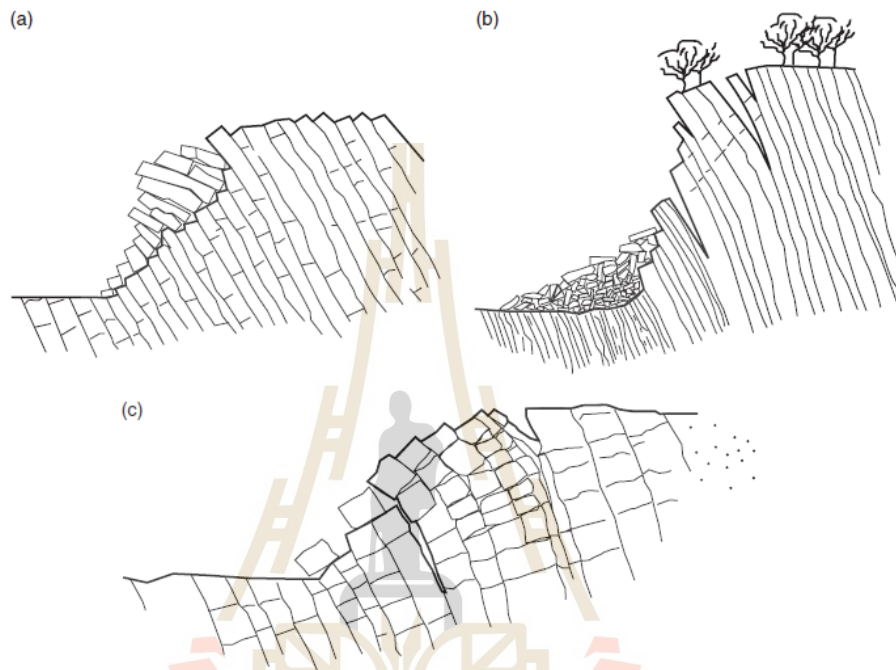


Figure 2.21 Toppling failure: (a) block toppling, (b) flexural toppling and (c) block-flexural toppling (Wyllie and Mah, 2005).

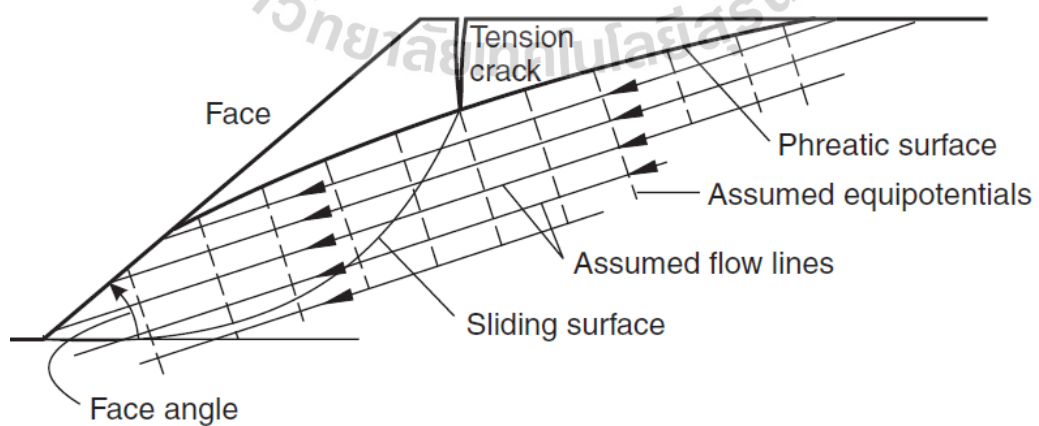


Figure 2.22 Circular failure (Wyllie and Mah, 2005).

2.3.2 Slope stability assessment

Several methods for slope stability assessment have been proposed by many researchers. Those methods can be basically grouped into four categories, i.e., kinematic analysis, limit equilibrium, empirical method and numerical modelling. Kinematic analysis is generally used to estimate the potential structural failure mechanisms as planar, wedge, toppling and circular failure (Price and Cosgrove, 1990). Limit equilibrium method compares the magnitudes of the driving and resisting forces that act along the sliding planes to estimate the factor of safety (Coggan et al., 1998). Empirical method or rock mass classification system is often used for preliminary evaluation of rock mass behaviors (Basahel and Mitri, 2017). It is simplified and convenient to use. Numerical model method is used in more complex slope geometries and failure mechanisms. It is sometimes useful when the other methods cannot represent rock mass behaviors (Wyllie and Mah, 2005; Romer and Ferentinou, 2019).

Wyllie and Mah (2005) compare the limit equilibrium method with the numerical method, as shown in Table 2.1.

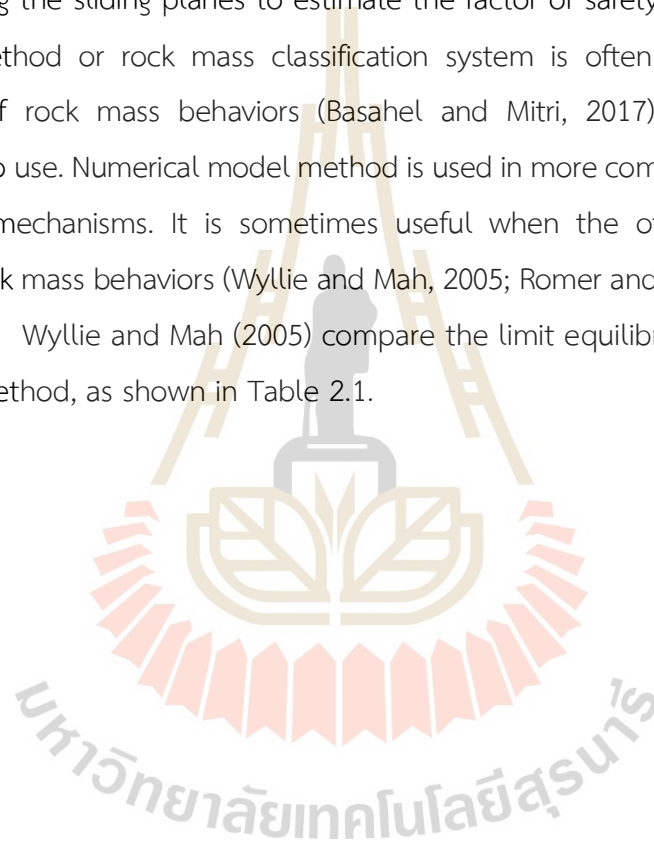


Table 2.1 Comparison between limit equilibrium and numerical analysis methods.

Analysis results	Limit equilibrium	Numerical analysis
Equilibrium	Satisfied only for specific objects, such as slices	Satisfied everywhere
Kinematics	A single kinematic condition is specified according to the articular geologic conditions	The “mechanisms” that develop satisfy kinematic constraints
Stresses	Computed approximately on certain surfaces	Computed everywhere using field equations
Deformation	Not considered	Part of the solution
Failure	Failure allowed only on certain pre-defined surfaces; no check on yield condition elsewhere	Yield condition satisfied everywhere; slide surfaces develop “automatically” as conditions dictate

2.4 Numerical model

Numerical models are useful tool for evaluation slope failure. This method has advantage in terms of complex boundary conditions and time, this model is an accurate reflection of realistic behavior of rock mass.

The numerical simulations are four mainly methods including (1) The finite element method (FEM), (2) The finite difference method (FDM), (3) The boundary element method (BEM) and (4) The distinct element method (DEM). The FEM mostly used among of the numerical method because of its able to present heterogeneous material and nonlinear behavior. The FDM is largely used due to simplicity and the possibility of handling the non-linear behavior, but FDM was limited to regular mesh and was not able to simulate complex boundary conditions and irregular geometries. The BEM is to perform rock fracturing due to the most recent formulations, to reduce

the problem complexity from 3D to 2D, or 2D to 1D and solve the problem at boundary. It is suitable for solving large-scale rock mechanical problems. The DEM can investigate discontinuous deformations and due to joints and their orientations. The DEM solves the motion equations and allows de-bonding and detaching of elements, it is represented true discontinuities and suitable for solving problems with large number of fractures which are outstanding in failure process. (Nikolić et al. 2016)

Bhasin and Kaynia (2004) observe the static and dynamic rock simulation of a 700 m high rock slope in western Norway. They used numerical simulations to evaluate the rock mass volume, it can potentially slide under static and dynamic forces. This estimation has required to estimate the run-up heights (tsunami) in a fjord that could potentially be caused by the rock sliding. The findings show that, due to variations in the inclination of discontinuities, the entire slope does not become unstable and that down-slope sliding and rotation of blocks occur mainly on the top layers of the slope. This model has helped not only to better understand the dynamics of the rock sliding but also to estimate the potential rock volume that can become unstable when subjected to static and dynamic loads.

Li et al. (2007) compare the DEM with the limit equilibrium method (LEM). They study the effect of joints on the rock slope failure modes between experimental investigations and DEM simulations. The results shown that the DEM estimates a lower critical excavation depth than the limit equilibrium method (LEM) of the joint structures in the rock mass are not ignored.

Severin et al. (2013) calibrate the deformation of open pit slope in Teck Highland Valley Copper mine, Canada by using data from 3D radar monitoring and the DEM (3DEC software). The displacements from radar may be misinterpreted when extended to the behavior of the entire slope. Therefore, the displacement data from radar are necessary to calibrate with numerical model. 3DEC (Itasca, 2007) are chosen to simulate of this problem because its ability to represent the regions bounded by the faults as distinct blocks and allow for the rock mass to slip, separate, and rotate along the mapped structures within the open pit while the individual blocks can deform and yield. The structural model and the simulation results of this site is illustrated in Figures 2.23 and 2.24.

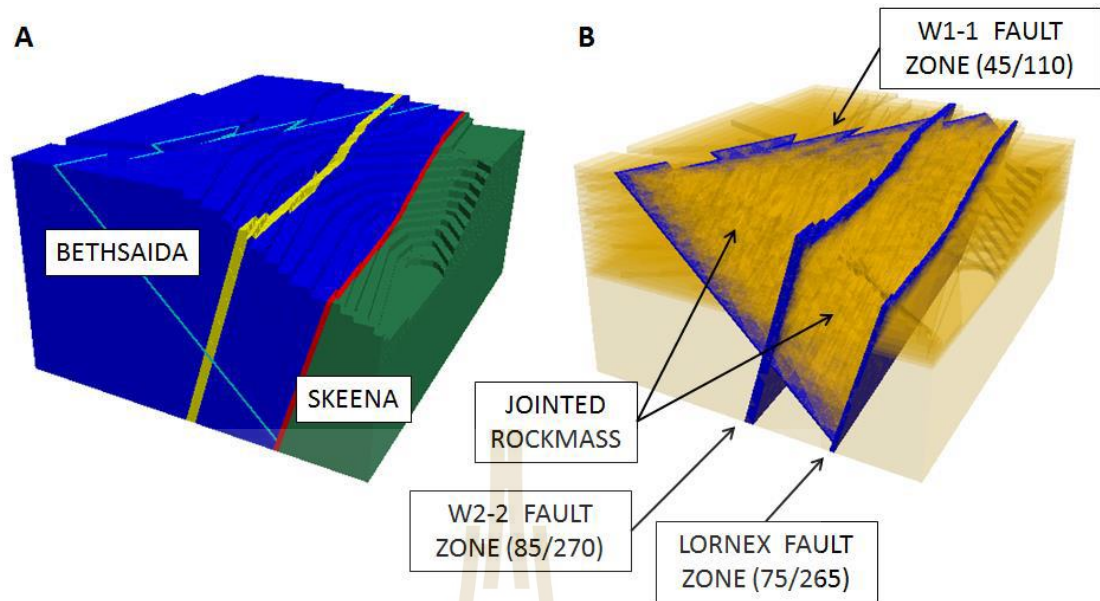


Figure 2.23 Large scale structures in 3DEC model (Severin et al., 2013).

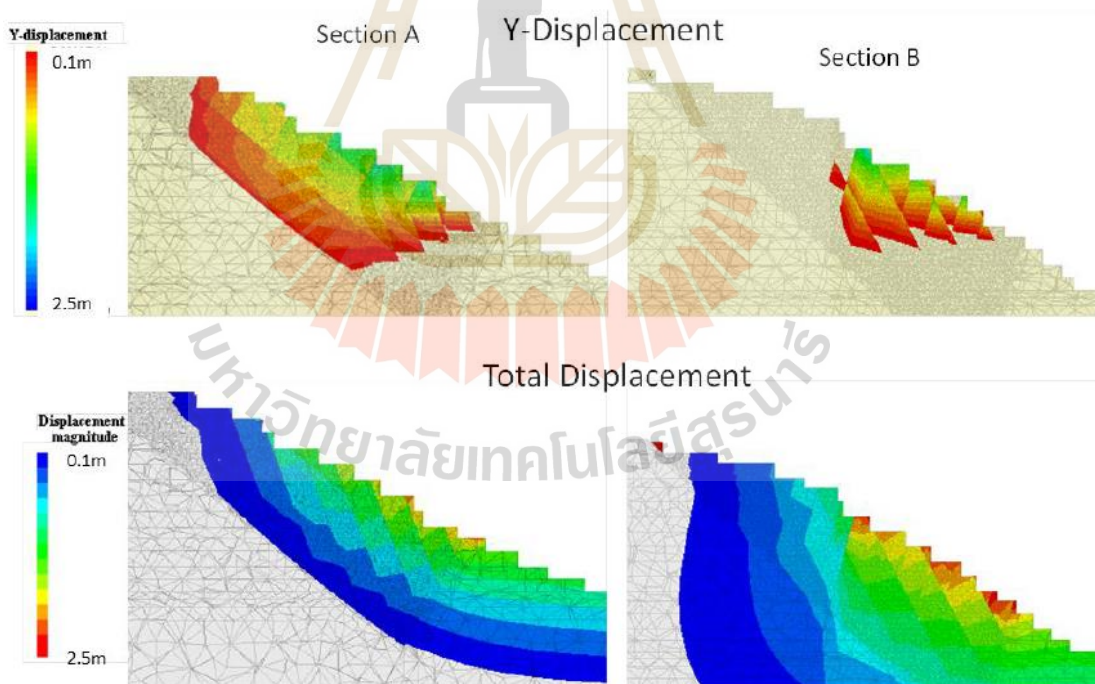
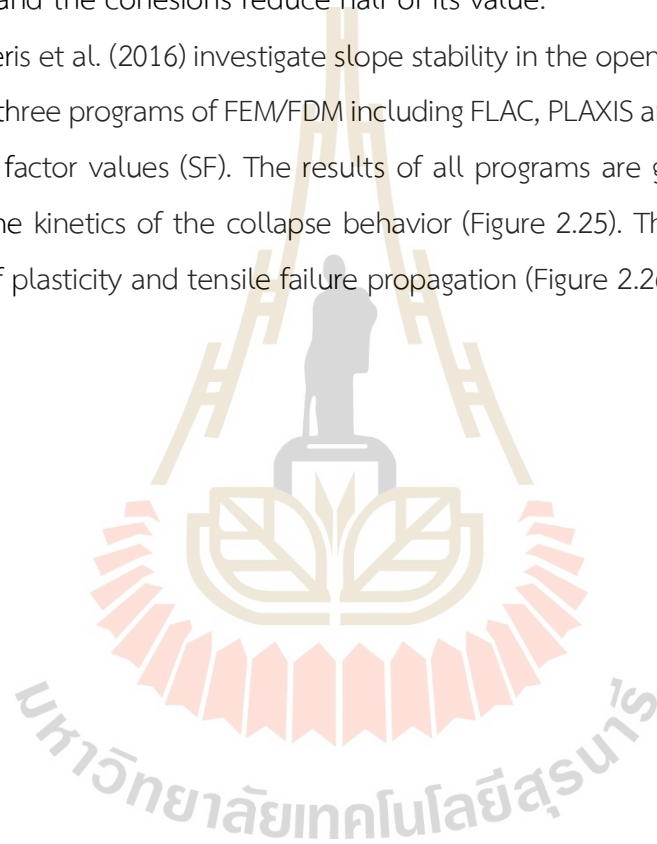


Figure 2.24 Horizontal and total displacement in 3DEC model (Severin et al., 2013).

Fawaz et al. (2014) compare the mechanical properties from experiments and back analysis of numerical model and study the effect of water in clay slope by using the FEM (PLAXIS software). The results indicate that the internal friction angles computed from model are the same as those measured in the laboratory, but the cohesion values from computer models are difference from laboratory test. This can cause by the disturbance of the soil samples tested in the laboratory. Furthermore, after slope fully saturated by water, the internal friction angle values decrease for a few degrees and the cohesions reduce half of its value.

Deliveris et al. (2016) investigate slope stability in the open pit lignite mines, they selected the three programs of FEM/FDM including FLAC, PLAXIS and Phase2 to compare the safety of factor values (SF). The results of all programs are good agreement of SF values and the kinetics of the collapse behavior (Figure 2.25). The findings have small differences of plasticity and tensile failure propagation (Figure 2.26).



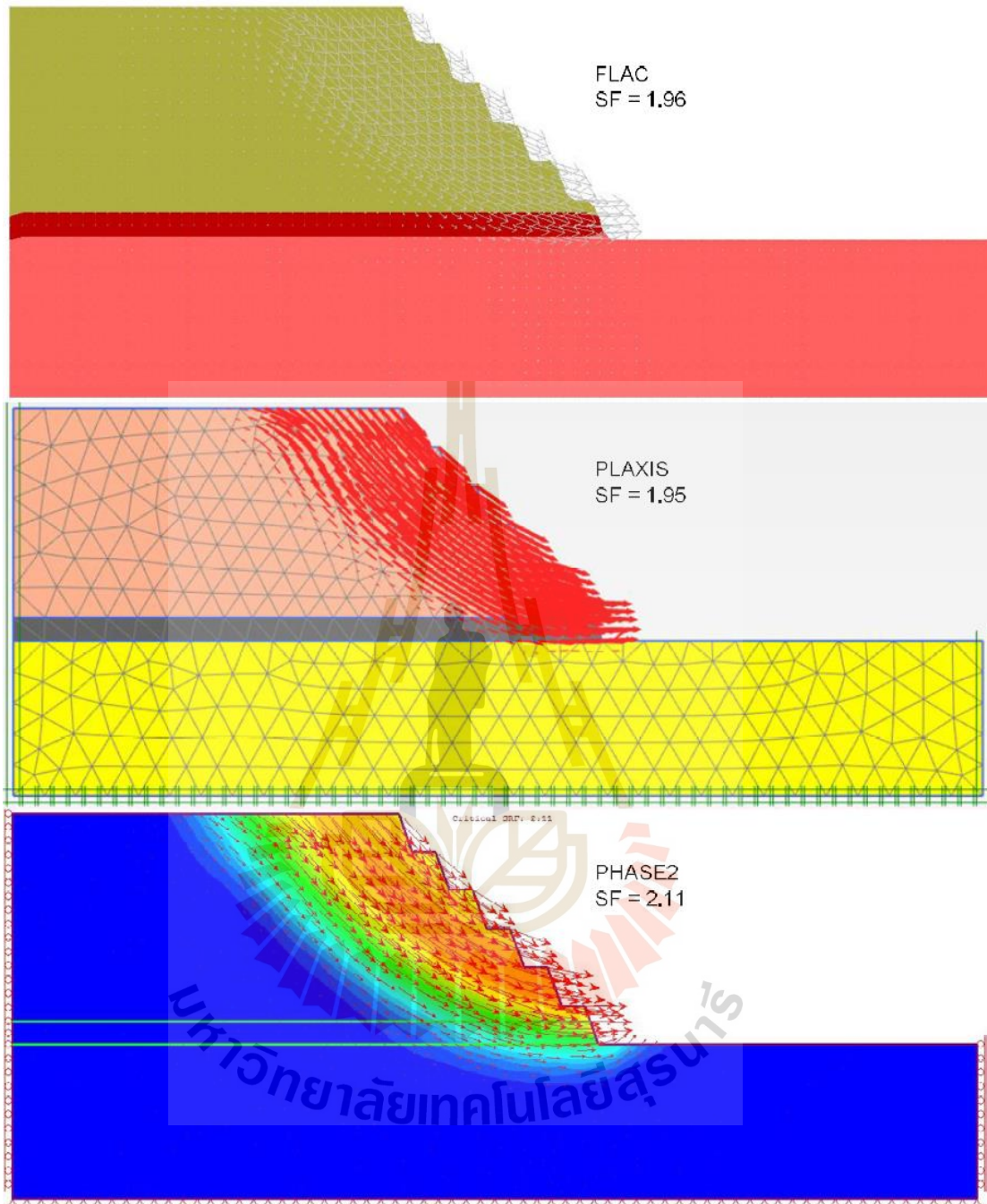


Figure 2.25 Displacement vectors distribution (Deliveris et al., 2016).

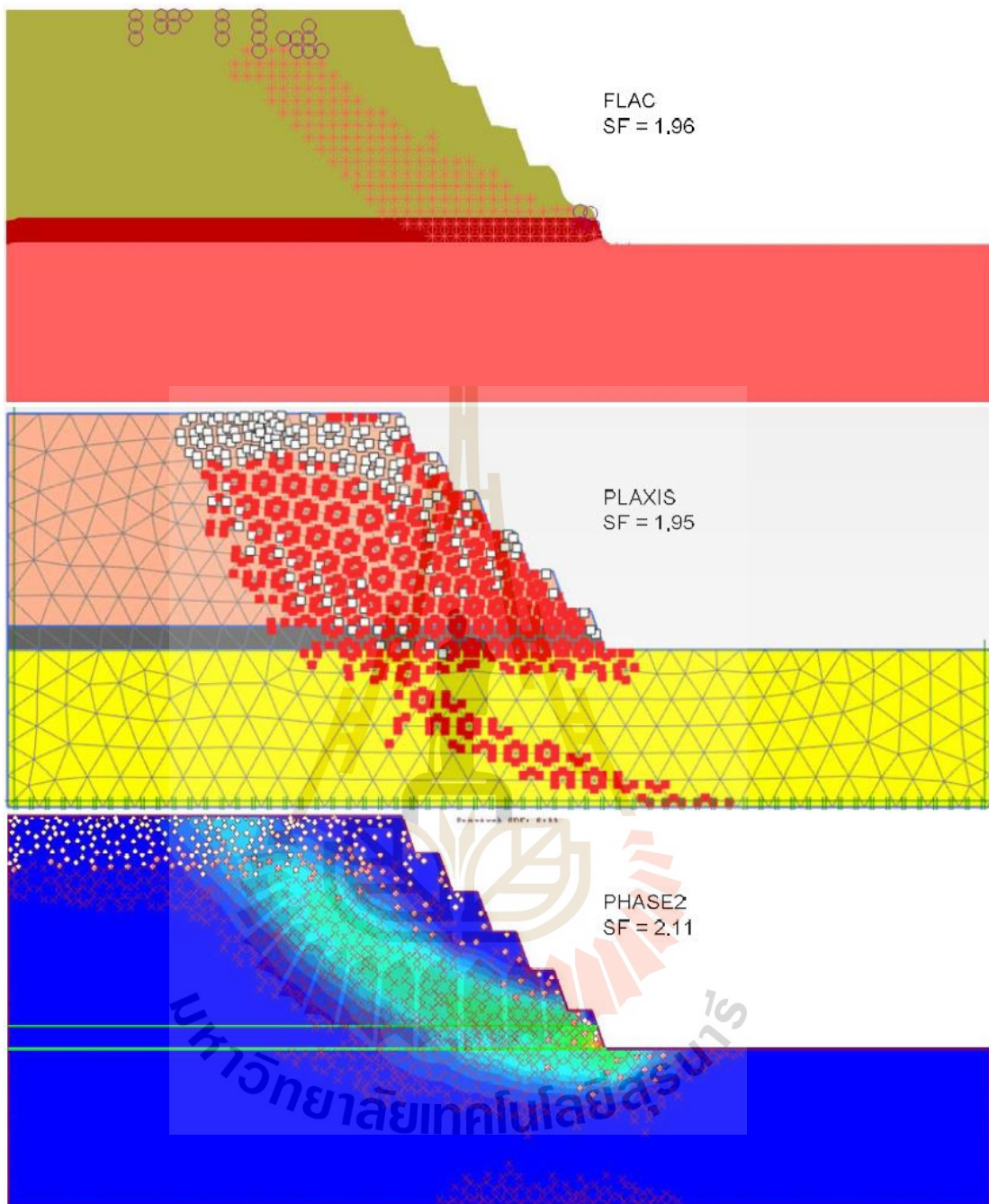


Figure 2.26 Plastic regions propagation. (Deliveris et al., 2016).

2.5 Relationship between slope geometry, mechanical properties of rock and slope stability

Abramson et al. (2001) state that the role of the slope failure factors can be summarized into 2 processes: 1) increased shear stresses (decrease in lateral pressure, triggered by removal of support, overloading, earthquakes) and 2) decreased shear strength of the soil (as a result of stratification, hydration of minerals and pore pressure due to melting snow or rainfall event). The strength parameters of slope materials (cohesion and friction angle) are influenced by the particle size distribution characteristics and other conditions, especially the water content (Zhou et al., 2013). However, increasing of both strength parameters have been reported to increase the slope stability (Coulibaly et al., 2017 and Muthreja, 2012).

Kusnadi (2017) studies mechanical properties of rock in open pit coal mine, East Kalimantan Province, Indonesia. The results indicate that landslide of slope due to decrease shear strength and the mechanical properties of rocks are affected the steepness of the slope include: shear strength (cohesion and internal friction angle), compressive and tensile strength.

Igwe and Chukwu (2018) summarize the effect of slope geometry (slope height and angle) and shear strength (cohesion and internal friction angle) of rock on slope stability (Factor of safety, FS) in Tables 2.2 through 2.5. Tables 2.2 and 2.3 show the results of the effects of slope height and angle can plot in the same plot area, as shown in Figure 2.27. The results indicate that the overall height and slope angle decrease with increasing FS. Figure 2.28 plots the factor of safety as affected by cohesion and internal friction angle, the results are combined from Tables 2.4 and 2.5. The results conclude that cohesion and internal friction angle decrease with decreasing FS.

Table 2.2 Implication of slope height on its factor of safety (Igwe and Chukwu, 2018).

Slope height (m)	Slope angle (°)	Cohesion (kPa)	Internal friction angle (°)	FS
5	40	32	14	3.45
10	40	32	14	1.80
15	40	32	14	1.37
20	40	32	14	1.13
25	40	32	14	0.94
30	40	32	14	0.86
35	40	32	14	0.82

Table 2.3 Significance of slope angle on factor of safety (Igwe and Chukwu, 2018).

Slope angle (°)	Slope height (m)	Cohesion (kPa)	Internal friction angle (°)	FS
10	35	32	14	3.08
20	35	32	14	2.05
30	35	32	14	1.42
40	35	32	14	0.96
50	35	32	14	0.85
60	35	32	14	0.80

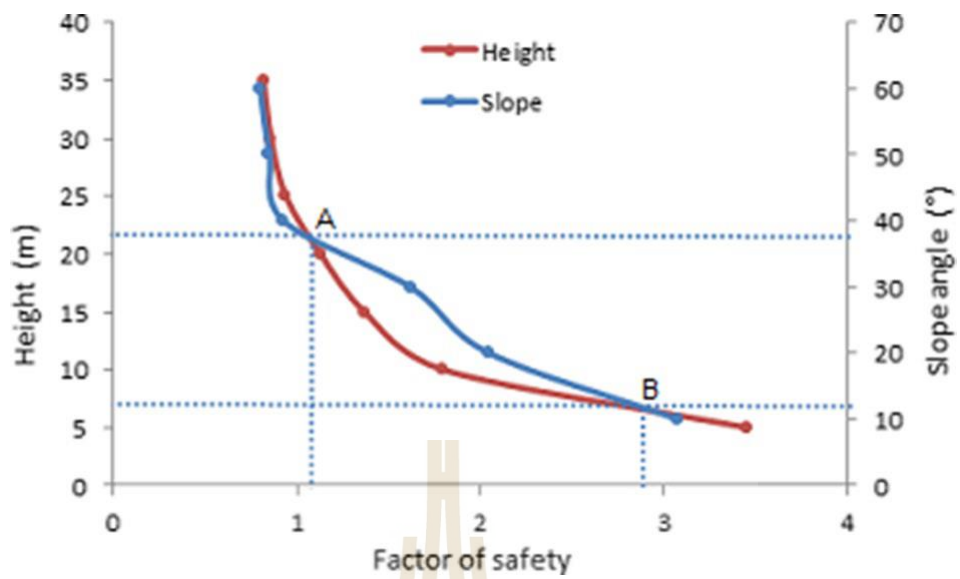


Figure 2.27 Effects of slope height and angle on factor of safety (Igwe and Chukwu, 2018).

Table 2.4 Effect of cohesion on factor of safety (Igwe and Chukwu, 2018).

Cohesion (kPa)	Internal friction angle (°)	Slope height (m)	Slope angle (°)	FS
5	14	35	40	0.72
10	14	35	40	0.77
15	14	35	40	0.81
20	14	35	40	0.84
25	14	35	40	0.88
30	14	35	40	0.93
35	14	35	40	0.96
40	14	35	40	1.00

Table 2.5 Effect of internal friction angle on factor of safety (Igwe and Chukwu, 2018).

Internal friction angle (°)	Cohesion (kPa)	Slope height (m)	Slope angle (°)	FS
5	32	35	40	0.32
10	32	35	40	0.42
15	32	35	40	0.56
20	32	35	40	0.66
25	32	35	40	0.78
30	32	35	40	0.91
35	32	35	40	1.02
40	32	35	40	1.15

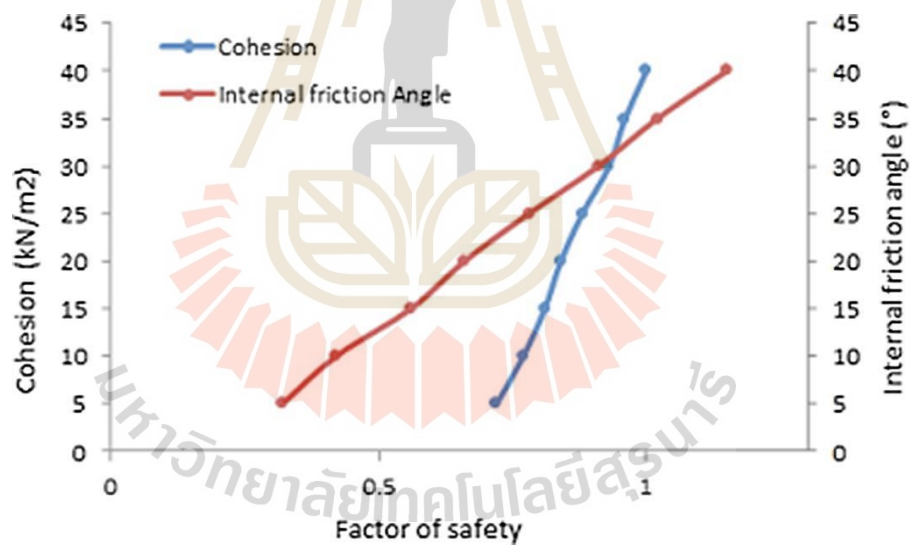


Figure 2.28 Relationship between shear strength parameters and factor of safety (Igwe and Chukwu, 2018).

CHAPTER III

LABORATORY TESTING

3.1 Introduction

The objective of laboratory testing is to determine the mechanical properties of rock and soil obtained from the study area. Mechanical properties are used to evaluate the stability of geo-engineering structures. This section describes the test method, apparatus and results.

3.2 Sample preparation

Three types of samples are used in this study. They are volcanic tuff (VTF), Red Beds (SLR), and faults collected from the South Wall zone in the Phu Kham pit as shown in Figure 3.1. The VTF and SLR, and fault are in hanging wall, footwall, and major fault, respectively (Figure 3.2, 3.3 and 3.4).

All samples are collected from diamond drill cores, there are three groups of sample preparation for different test methods, 1) uniaxial compressive strength tests (UCS), 2) direct shear tests of rock specimens on rough fracture (DS), and 3) direct shear tests of soil samples (DS- soil).

The core specimens with a nominal diameter of 61 mm (HQ bit size) tested here are drilled from depths ranging from 15.50 to 183.40 m. Twenty-six VTF specimens and twenty-seven SLR specimens are cut to obtain a nominal length-to-diameter ratio (L/D) ranging between 2.0 and 2.5 for UCS testing, following the ASTM D7012-14 standard practice.

Nine pairs of VTF specimens and nine pairs of SLR specimens are selected from a single discontinuity and cut to have length of 10 cm for DS testing, following the ASTM D5607 standard practice.

Three soil samples of fault for DS-soil test are collected. They are packed in plastic wrap to minimize disturbance, following the ASTM D3080 standard practice.

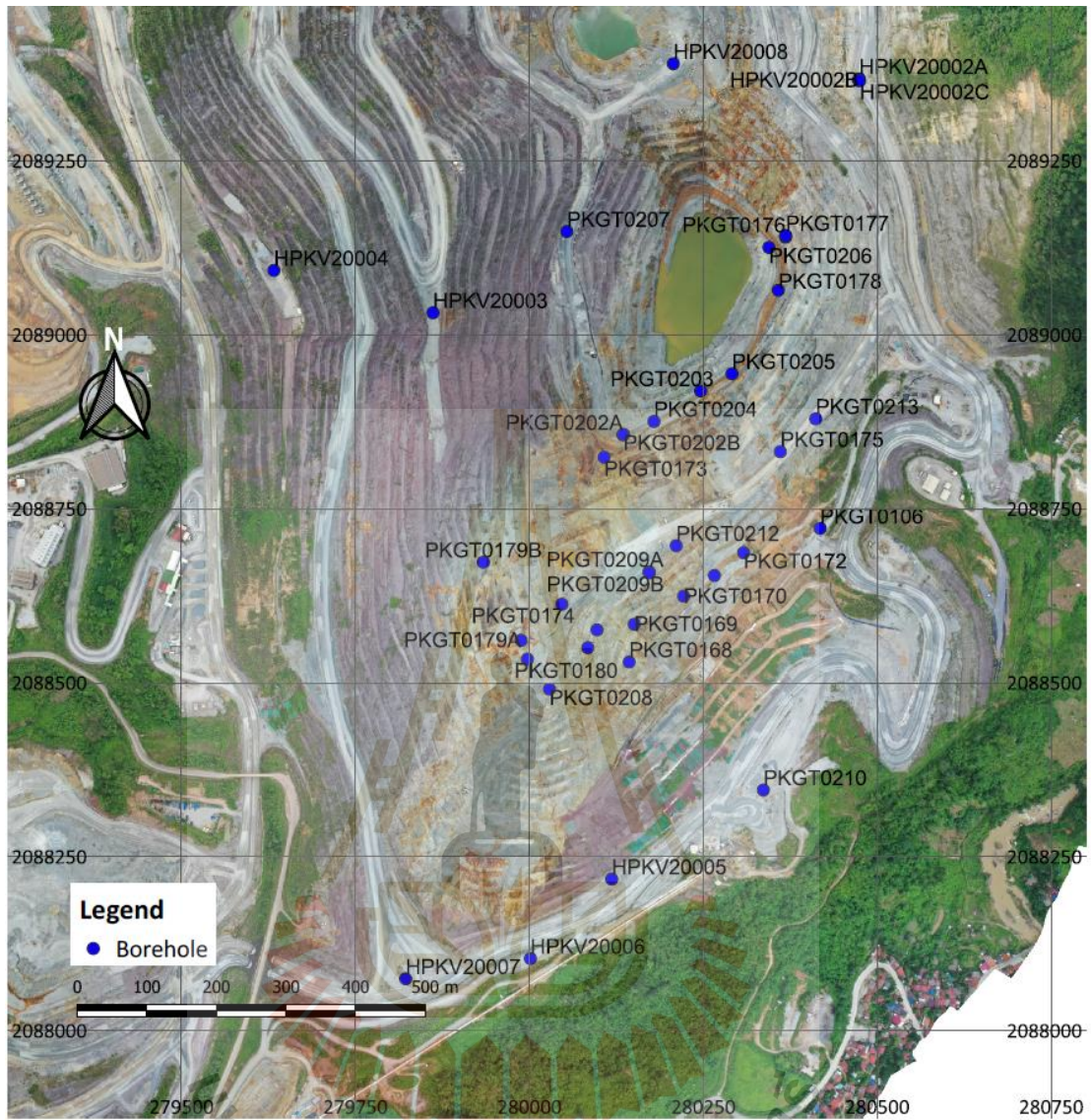


Figure 3.1 Borehole location in the study area.



Figure 3.2 VTF core samples



Figure 3.3 SLR core samples



Figure 3.4 Fault samples

3.3 Uniaxial compressive strength test

Rock strength or compressive strength of the joint walls is required as data input in numerical simulations. The laboratory testing procedure strictly follows the American Society for Testing and Materials (ASTM D7012-14). Compression load frame is shown in Figure 3.5. Cylindrical specimens of VTF and SLR with a diameter of 61 mm and L/D ratio between 2.0 to 2.5 are axially loaded to failure. Twenty-six VTF and twenty-seven SLR specimens have been tested. The UCS is calculated from the maximum load divided by the initial cross-sectional area. The elastic modulus (Young's modulus) is determined from the stress-strain curves at 50% of the maximum stress. Figures 3.6 and 3.7 show some pre-test and post-test of VTF and SLR samples. Figures 3.8 and 3.9 present the stress-strain relationships of some UCS test results. Sample dimensions and test results are summarized in Tables 3.1 through 3.4.



Figure 3.5 Uniaxial compressive strength test frame.



Figure 3.6 Some VTF (a) and SLR (b) specimens prepared for UCS testing.



Figure 3.7 Post-test VTF (a) and SLR (b) specimens of UCS testing.

Table 3.1 Dimensions of VTF specimen for UCS testing.

Sample No.	Borehole No.	Depth (m)		D (mm)	L (mm)	Weight (mm)	L/D	Density (g/cc)
		From	To					
GTT1693	PKGT0166	38.81	39.01	61.0	155.6	1238.6	2.55	2.73
GTT1694	PKGT0166	40.80	41.00	61.0	154.7	1235.0	2.54	2.73
GTT1695	PKGT0166	78.42	78.62	60.7	153.1	1159.2	2.52	2.62
GTT1696	PKGT0166	79.22	79.44	61.2	153.6	1188.7	2.51	2.64
GTT1817	PKGT0167	24.29	24.39	60.7	129.6	976.9	2.14	2.61
GTT1818	PKGT0167	25.20	25.39	60.7	153.7	1217.3	2.53	2.74
GTT1819	PKGT0167	30.58	30.75	60.7	155.5	1223.9	2.56	2.72
GTT1820	PKGT0167	33.46	33.64	60.7	154.6	1220.0	2.55	2.73
GTT1821	PKGT0167	65.00	65.20	60.9	120.6	950.4	1.98	2.71
GTT1822	PKGT0167	83.30	83.54	60.6	153.9	1211.3	2.54	2.73
GTT1823	PKGT0167	98.33	98.60	61.0	134.1	1144.6	2.20	2.93
GTT1824	PKGT0167	104.43	104.66	61.0	152.3	1289.4	2.50	2.90
GTT1825	PKGT0167	108.31	108.58	60.8	141.9	1136.9	2.34	2.76
GTT1826	PKGT0167	111.58	111.88	60.9	112.0	889.1	1.84	2.73
GTT1901	PKGT0175	15.55	15.73	61.0	153.7	1235.2	2.52	2.75
GTT1902	PKGT0175	17.30	17.50	61.0	152.9	1229.4	2.51	2.75
GTT1903	PKGT0175	43.90	44.05	60.7	152.2	1202.5	2.51	2.73
GTT1959	PKGT0174	55.80	55.93	60.7	154.1	1233.1	2.54	2.77
GTT1963	PKGT0174	85.16	85.30	61.0	152.9	1220.0	2.51	2.73
GTT1970	PKGT0174	115.37	115.53	60.7	154.0	1220.2	2.54	2.74
GTT1971	PKGT0174	115.60	115.75	61.3	152.7	1216.9	2.49	2.70
GTT1972	PKGT0174	116.10	116.23	60.9	148.6	1179	2.44	2.72
GTT2026	PKGT0180	18.57	18.77	61.4	128.8	991.5	2.10	2.60
GTT2028	PKGT0180	46.00	46.25	61.1	154.2	1231.6	2.52	2.73
GTT2042	PKGT079B	87.60	87.90	61.0	153.7	1232.7	2.52	2.74
Average								2.73
Standard Deviation								± 0.08

Table 3.2 Dimensions of SLR specimen for UCS testing.

Sample No.	Borehole No.	Depth (m)		D (mm)	L (mm)	Weight (mm)	L/D	Density (g/cc)
		From	To					
GTT1756	PKGT0168	116.10	116.30	60.4	151.5	1316.1	2.51	3.03
GTT1760	PKGT0168	131.00	131.20	60.5	151.4	1343.3	2.50	3.09
GTT1761	PKGT0168	131.92	132.08	60.8	137.8	1113.7	2.27	2.78
GTT1762	PKGT0168	148.43	148.67	60.7	128.9	1029.7	2.12	2.76
GTT1792	PKGT0172	128.63	128.79	60.9	138.9	1021.6	2.28	2.52
GTT1906	PKGT0175	125.08	125.25	60.5	160.6	1304.8	2.65	2.82
GTT1907	PKGT0175	125.30	125.46	60.7	154.3	1226.9	2.54	2.75
GTT1908	PKGT0175	140.20	140.40	60.6	134.1	1072.1	2.21	2.77
GTT1909	PKGT0175	142.56	142.65	60.8	158.3	1282.8	2.60	2.79
GTT1920	PKGT0173	159.72	160.09	60.7	151.7	1255.1	2.50	2.86
GTT1980	PKGT0174	163.63	163.98	60.9	151.0	1246.1	2.48	2.83
GTT1981	PKGT0174	169.65	169.85	60.8	153.5	1240.7	2.52	2.78
GTT1998	PKGT0171	93.28	93.49	60.4	152.9	1229.3	2.53	2.81
GTT2000	PKGT0171	110.16	110.38	60.5	152.5	1244.5	2.52	2.84
GTT2002	PKGT0171	140.40	140.62	60.6	147.5	1183.9	2.43	2.79
GTT2004	PKGT0171	166.30	166.50	60.6	148.1	1150.0	2.44	2.69
GTT2005	PKGT0171	166.70	166.90	60.6	151.6	1207.5	2.50	2.77
GTT2006	PKGT0171	167.22	167.40	60.8	149.0	1200.4	2.45	2.77
GTT2031	PKGT0180	76.30	76.55	60.5	154.1	1207.8	2.55	2.72
GTT2032	PKGT0180	103.52	103.78	60.4	162.5	1285.6	2.69	2.76
GTT2049	PKGT079B	183.00	183.20	60.5	148.6	1182.4	2.46	2.77
GTT2050	PKGT079B	183.20	183.40	60.6	148.4	1238.3	2.45	2.90
GTT2755	PKGT0203	137.64	137.44	61.0	151.2	1222.4	2.48	2.77
GTT2855	PKGT0210	73.82	73.63	61.1	152.4	1223.2	2.50	2.74
GTT3047	HPKV20006	47.27	47.41	60.5	156.7	1232.4	2.59	2.74
GTT3089	HPKV20003	132.67	132.81	61.2	156.7	1244.3	2.56	2.70
GTT3138	PKGT0212	138.25	138.39	60.5	163.2	1304.2	2.70	2.78
Average								2.84
Standard Deviation								± 0.17

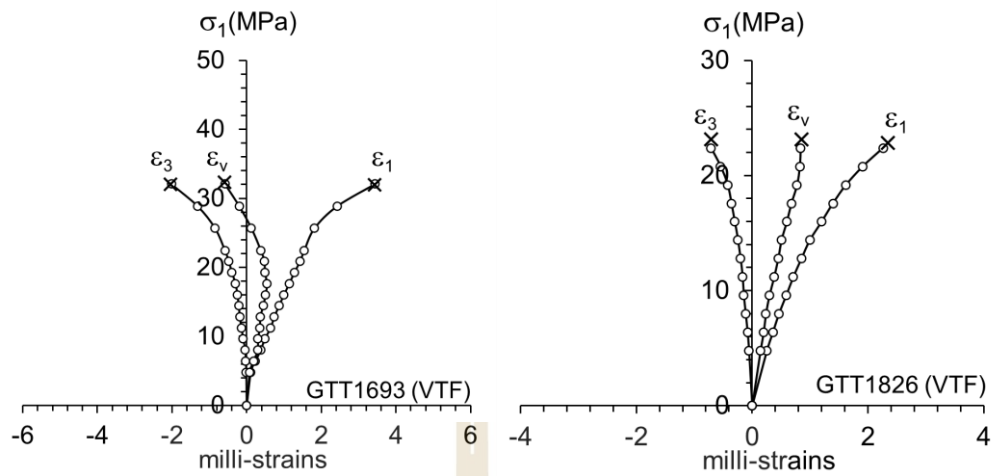


Figure 3.8 Some stress-strain curves of uniaxial compression test (VTF).

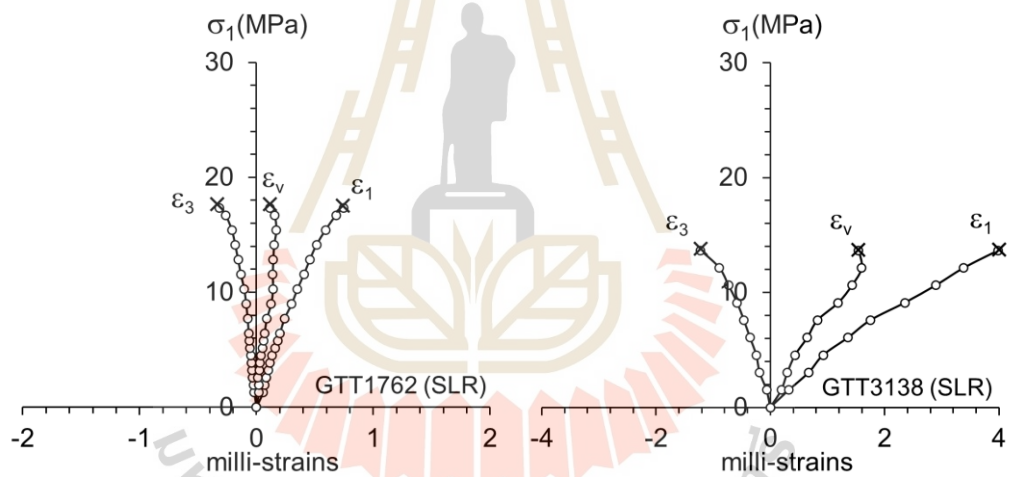


Figure 3.9 Some stress-strain curves of uniaxial compression test (SLR).

Table 3.3 Test results of VTF samples.

Sample No.	Strength (MPa)	Elastic Modulus (GPa)	Poisson's Ratio	Mode of Failure
GTT1693	34.6	16.3	0.23	Longitudinal Spitting
GTT1694	17.3	17.6	0.22	Weak Failure
GTT1695	2.9	5.3	0.25	Weak Plane Failure
GTT1696	4.4	3.1	0.28	Weak Plane Failure
GTT1817	60.4	42.7	0.26	Longitudinal Spitting
GTT1818	27.6	28.5	0.23	Longitudinal Spitting
GTT1819	41.3	49.1	0.20	Longitudinal Spitting
GTT1820	21.6	21.2	0.23	Longitudinal Spitting
GTT1821	10.1	28.4	0.21	Longitudinal Spitting
GTT1822	35.1	18.6	0.23	Weak Plane Failure
GTT1823	4.7	3.3	0.17	Weak Plane Failure
GTT1824	13.8	3.5	0.24	Weak Plane Failure
GTT1825	3.5	5.1	0.28	Weak Plane Failure
GTT1826	9.8	9.6	0.27	Weak Plane Failure
GTT1901	5.7	14.3	0.25	Weak Plane Failure
GTT1902	9.1	21.0	0.21	Weak Plane Failure
GTT1903	3.2	15.1	0.21	Weak Plane Failure
GTT1959	9.2	12.3	0.25	Weak Plane Failure
GTT1963	44.1	35.2	0.24	Longitudinal Spitting
GTT1970	10.8	21.2	0.25	Weak Plane Failure
GTT1971	3.7	9.9	0.2	Weak Plane Failure
GTT1972	9.5	27.8	0.3	Weak Plane Failure
GTT2026	3.7	2.5	0.20	Weak Plane Failure
GTT2028	11.9	13.2	0.24	Weak Plane Failure
GTT2042	4.4	9.0	0.21	Weak Plane Failure
Average	16.14	17.35	0.24	
Standard Deviation	± 15.30	± 12.10	± 0.03	

Table 3.4 Test results of SLR samples.

Sample No.	Strength (MPa)	Elastic Modulus (GPa)	Poisson's Ratio	Mode of Failure
GTT1730	93.1	25.5	0.22	Longitudinal Spitting
GTT1756	38.5	18.0	0.26	Weak Plane Failure
GTT1760	22.4	11.3	0.30	Weak Plane Failure
GTT1761	7.9	7.0	0.17	Weak Plane Failure
GTT1762	3.8	4.1	0.21	Weak Plane Failure
GTT1792	2.5	11.1	0.25	Weak Plane Failure
GTT1906	11.2	25.2	0.22	Weak Plane Failure
GTT1907	5.7	3.2	0.26	Weak Plane Failure
GTT1908	8.3	4.7	0.25	Longitudinal Spitting
GTT1909	4.4	5.6	0.23	Weak Plane Failure
GTT1920	5.7	6.1	0.22	Shear Failure
GTT1980	8.2	7.1	0.22	Weak Plane Failure
GTT1981	5.1	7.5	0.28	Weak Plane Failure
GTT1998	20.5	19.8	0.25	Weak Plane Failure
GTT2000	22.4	15.0	0.24	Longitudinal Spitting
GTT2002	3.0	9.0	0.10	Weak Failure
GTT2004	39.4	22.2	0.13	Longitudinal Spitting
GTT2005	13.7	4.4	0.28	Longitudinal Spitting
GTT2006	8.7	15.9	0.27	Weak Plane Failure
GTT2031	17.3	26.1	0.24	Longitudinal Spitting
GTT2032	17.3	26.6	0.22	Longitudinal Spitting
GTT2049	6.4	7.1	0.21	Weak Plane Failure
GTT2050	11.2	5.8	0.25	Longitudinal Spitting
GTT2755	0.6	3.7	0.19	Weak Plane Failure
GTT2855	17.2	29.9	0.26	Weak Plane Failure
GTT3047	3.8	10.4	0.22	Longitudinal Spitting
GTT3089	18.8	13.1	0.28	Shear Failure
GTT3138	6.4	10.4	0.25	Weak Plane Failure
Average	15.42	12.50	0.23	
Standard Deviation	± 17.54	± 7.88	± 0.04	

3.4 Direct shear tests of rock specimens on rough fracture

The rock shear strength is a significant parameter for the design of rock slopes, foundations, and structures. The test procedure is followed the American Society for Testing and Materials standard (ASTM D5607-16) and the method suggested by the International Society of Rock Mechanics (ISRM) (Brown, 1981). Figure 3.10 is shown direct shear test frame.

Nine pairs of VTF specimens and nine pairs of SLR specimens with a nominal length 10 cm contain discontinuities (i.e., bedding, joint), and are separated into upper and lower halves of the encapsulated cement molds. The shear displacement is applied under constant rate of 0.2 mm/min. A minimum of 10 sets of monitoring and recording data points is suggested to be taken before obtaining the peak shear strength. The loading continues until a residual shear strength is established. Post-test VTF and SLR specimens are shown in Figure 3.11 and 3.12. Figure 3.13 and 3.14 show the stress-displacement relationships of some DS test results. Sample dimensions and test results are summarized in Table 3.5 through 3.8.



Figure 3.10 Direct shear test frame

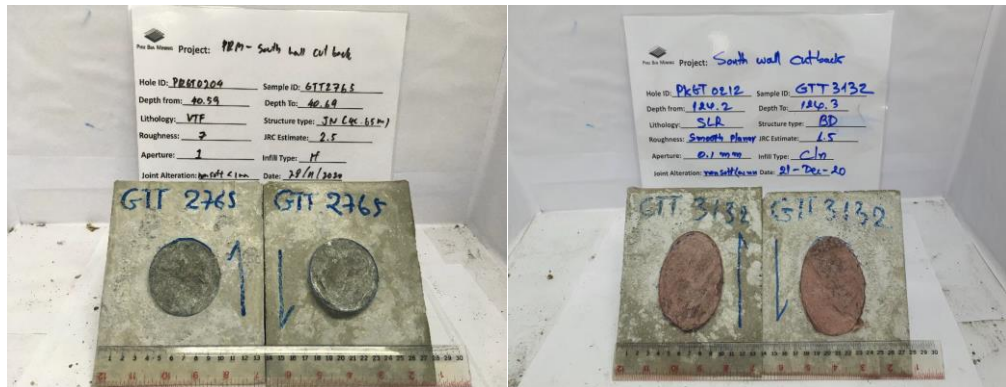


Figure 3.11 Some VTF (left) and SLR (right) specimens prepared and moulded for DS testing.

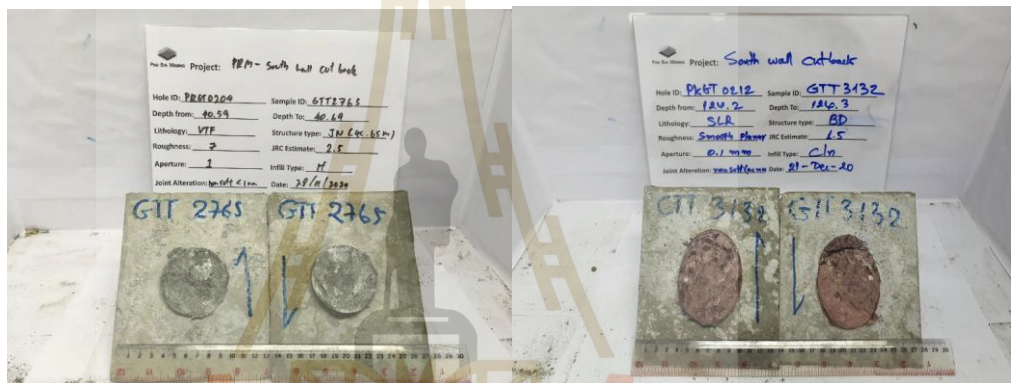


Figure 3.12 Some VTF (left) and SLR (right) specimens after DS testing

Table 3.5 Dimensions of VTF specimen for DS testing.

Sample No.	Borehole No.	Depth (m)		Nominal cross-sectional area (m ²)	Density (g/cc)
		From	To		
GTT1684	PKGT0166	55.14	55.25	0.0037	2.68
GTT1687	PKGT0166	96.45	96.55	0.0035	2.73
GTT1840	PKGT0169	86.42	86.53	0.0040	2.69
GTT1842	PKGT0169	95.02	95.12	0.0035	2.70
GTT1850	PKGT0169	172.87	172.98	0.0044	2.73
GTT1886	PKGT0175	36.75	36.86	0.0042	2.69
GTT1887	PKGT0175	42.55	42.65	0.0044	2.70
GTT2765	PKGT0204	40.59	40.69	0.0031	2.73
GTT3129	PKGT0212	103.95	104.05	0.0033	2.73
Average					2.70
Standard Deviation					± 0.02

Table 3.6 Dimensions of SLR specimen for DS testing.

Sample No.	Borehole No.	Depth (m)		Nominal cross-sectional area (m ²)	Density (g/cc)
		From	To		
GTT1716	PKGT0170	135.10	135.45	0.0042	2.68
GTT1718	PKGT0170	162.10	162.22	0.0043	2.68
GTT1988	PKGT0171	131.36	131.45	0.0035	2.67
GTT1990	PKGT0171	168.83	168.95	0.0032	2.67
GTT2025	PKGT0180	101.69	101.86	0.0040	2.64
GTT2141	PKGT0183	88.22	88.33	0.0039	2.60
GTT3009	PKGT0208	54.00	54.700	0.0036	2.65
GTT3131	PKGT0212	123.85	123.95	0.0040	2.59
GTT3132	PKGT0212	124.20	124.30	0.0043	2.68
Average					2.66
Standard Deviation					± 0.03

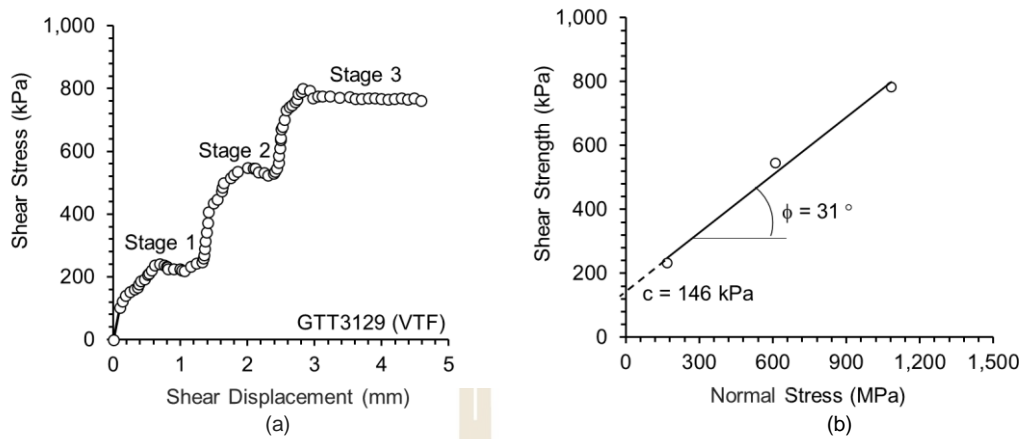


Figure 3.13 Some stress-displacement relationships of DS test (VTF) (a) with shear strength-normal stress (b).

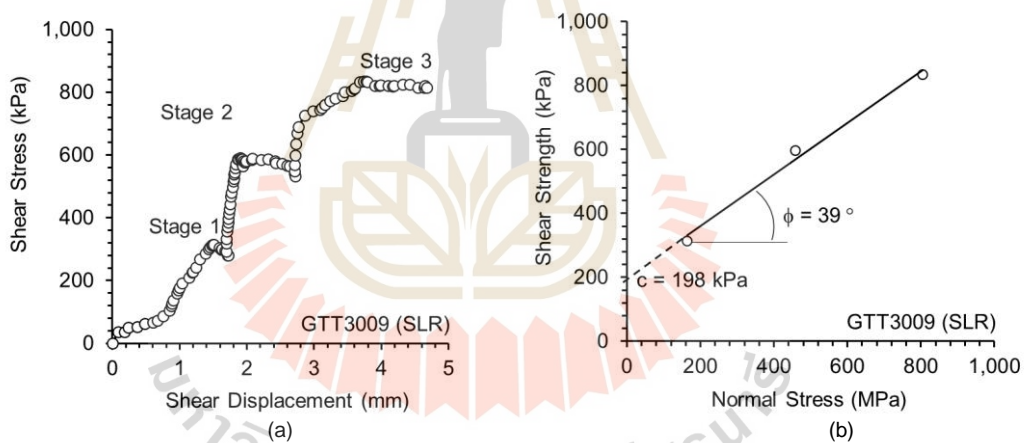


Figure 3.14 Some stress-displacement relationships of DS test (SLR) (a) with shear strength-normal stress (b).

Table 3.7 DS test results of VTF.

Sample No.	Normal stress (kPa)			Shear stress (kPa)		
	Stage 1	Stage 2	Stage 3	Stage 1	Stage 2	Stage 3
GTT1684	135.13	405.40	675.67	240.00	428.97	650.35
GTT1687	142.86	714.28	1285.71	140.00	562.97	747.85
GTT1840	250.00	500.00	750.00	285.00	400.00	640.00
GTT1842	284.00	568.18	852.27	400.00	620.00	950.00
GTT1850	225.23	675.67	1126.12	150.00	280.00	400.00
GTT1886	239.23	717.70	1196.17	185.00	350.00	565.91
GTT1887	224.72	674.16	1123.59	175.00	300.00	532.72
GTT2765	164.46	682.79	1068.77	140.00	422.89	641.30
GTT3129	168.59	610.33	1082.4	235.00	545.28	784.11

Table 3.8 DS test results of SLR.

Sample No.	Normal stress (kPa)			Shear stress (kPa)		
	Stage 1	Stage 2	Stage 3	Stage 1	Stage 2	Stage 3
GTT1716	118.76	593.82	1068.88	100.00	311.87	550.14
GTT1718	233.64	700.93	1168.22	115.00	452.75	600.00
GTT1988	283.28	849.85	1416.43	215.00	602.06	1045.00
GTT1990	308.64	925.92	1543.20	200.00	513.51	750.00
GTT2025	123.76	618.81	1113.86	200.00	496.98	817.77
GTT2141	255.10	765.30	1275.51	250.00	444.87	650.00
GTT3009	288.76	842.12	1377.34	250.00	440.25	800.00
GTT3131	138.919	497.70	873.305	250.00	389.73	608.43
GTT3132	155.093	468.02	826.628	380.00	700.00	880.00

Hijaj et al. (2005), Dazhong, (2014) and Kanazawa, (2021) summarize a best approach for estimate shear strength to determine slope stability. Shear strength parameters from lower bound limit are conservative, but the upper bound limit is overestimated. Adopted value is a combination of upper and lower bound limit, this is a suitable estimation for slope in mining because conservative scenario is affected to operation economy. Figures 3.15 and 3.16 plot shear strengths and normal stresses of laboratory testing data (Tables 3.7 and 3.8). Mohr-Coulomb strength parameters are estimated by using Equation (3.1) and summarized in Table 3.9.

$$\tau = \sigma \tan \phi + c \quad (3.1)$$

where τ = shear strength,
 σ = normal stress,
 ϕ = friction angle,
 c = cohesion

Table 3.9 shows upper bound cohesion of VTF is more twice times than adopted value and 3 times than lower bound limit, but upper bound cohesion of SLR is more 2.3 times than adopted value and 4 times than lower bound limit. Friction angles of VTE do not quite differ in each approach. The upper bound limit friction angle of SLR is more than the lower bound limit of 8 degrees, but it is more than adopted value of 0.9 degrees.

Table 3.9 Summary of shear strength parameters of VTF and SLR.

Rock type	Approach	c (kPa)	ϕ (degrees)
VTF	Upper bound limit	236.80	29.0
	Adopted value	104.69	28.4
	Lower bound limit	78.33	26.0
SLR	Upper bound limit	209.58	28.0
	Adopted value	89.10	27.1
	Lower bound limit	52.03	20.0

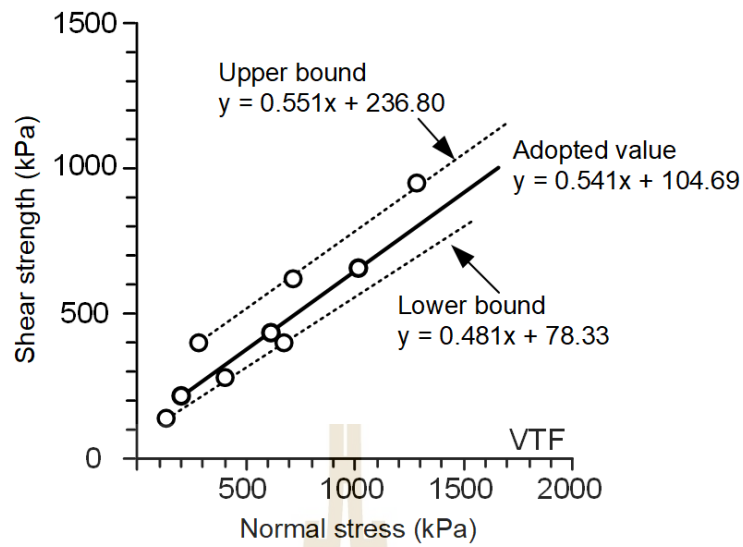


Figure 3.15 Shear strength of VTF.

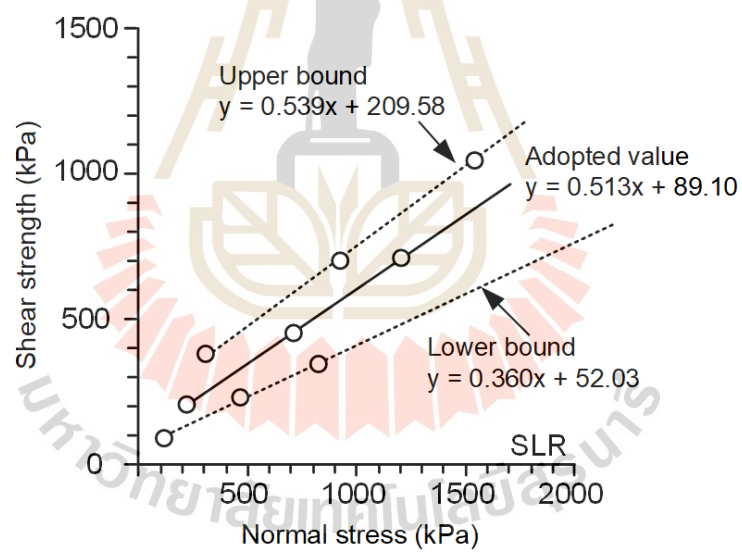


Figure 3.16 Shear strength of SLR.

3.5 Direct shear tests of soil samples

A set of direct shear tests on compacted soil samples has been conducted on fault samples. After compaction, the soil samples are placed and set up in a direct shear load box and frame (Figure 3.17). All samples are sheared under a constant displacement rate of 0.1 mm/min. Figures 3.18 and 3.19 show pre-test and post-test of soil direct shear test. Normal stresses are determined from in-situ pressures. The sample descriptions and test results are shown in Tables 3.10 and 3.11.

Shear strength parameters of soil are determined from the relationship between shear strengths and normal stresses (Figure 3.20) with a limit approach similar with section 3.4. Table 3.12 summarizes shear strength parameters from test results. Cohesion and friction angle do not quite differ in each approach.

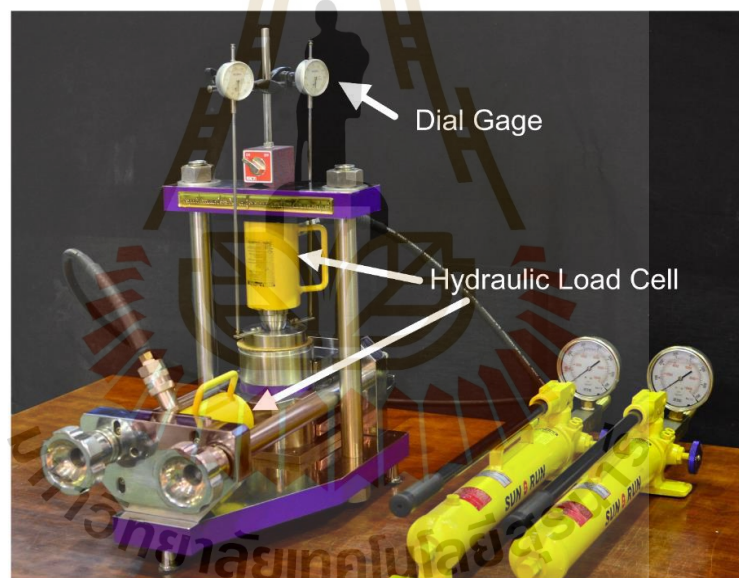


Figure 3.17 Direct shear tests frame for three-ring mold

Table 3.10 Dimensions of soil samples.

Samples No.	Borehole No.	Depth (m)	D (mm)	L (mm)	W (g)	Shear Area (cm ²)	Bulk Density (g/cc)
GTT1254-DS-01	PKGT0106	85.90-88.00	101.6	116.3	1,882	81.07	1.99
GTT1254-DS-02					1,895		2.01
GTT1254-DS-03					1,915		2.03
GTT1254-DS-04					1,895		2.01
GTT1255-DS-01		88.00-90.30	101.6	116.3	1,911	81.07	2.02
GTT1255-DS-02					1,916		2.03
GTT1255-DS-03					1,959		2.08
GTT1255-DS-04					1,917		2.03
GTT1256-DS-01		90.30-93.17	101.6	116.3	1,945	81.07	2.06
GTT1256-DS-02					1,954		2.07
GTT1256-DS-03					1,928		2.04
GTT1256-DS-04					1,942		2.06
Average							2.03
Standard Deviation							± 0.03



Figure 3.18 Soil samples before testing



Figure 3.19 Soil samples after testing

Table 3.11 Test results of soil samples.

Sample No.	Normal stress (kPa)				Shear stress (kPa)			
	Stage 1	Stage 2	Stage 3	Stage 4	Stage 1	Stage 2	Stage 3	Stage 4
GTT1716	689.8	1378.4	2068.2	2757.7	297.2	540.3	694.5	851.3
GTT1718	689.8	1378.4	2068.2	2757.7	268	491.3	625.3	781.6
GTT1988	689.8	1378.4	2068.2	2757.7	272.5	469	625.3	770.5

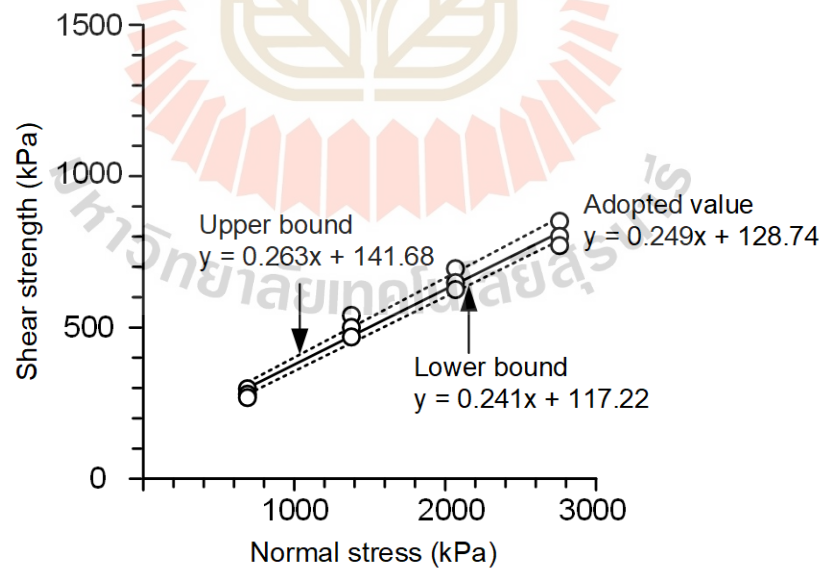


Figure 3.20 Shear strength of fault.

Table 3.12 Summarize shear strength parameters of Fault.

Rock type	Approach	c (kPa)	ϕ (degrees)
Fault	Upper boundary	141.68	14.8
	Adopted value	128.74	14.0
	Lower boundary	117.22	13.6



CHAPTER IV

NUMERICAL SIMULATIONS

4.1 Introduction

This section describes the results of discrete element analyses using UDEC (Itasca, 2011). The objective of numerical simulations is to determine slope stability behavior under various slope face angles, distances between fault and crest and mechanical properties of hanging rock. The models use mechanical properties obtained from the laboratory testing.

4.2 Numerical simulations

Discrete element analyses are performed using UDEC (Itasca, 2011) to describe the shear strain and displacement vectors of the slope models. The discrete element models are constructed to represent various slope face angles (ψ) and distances between fault and slope crest (X). The models use mechanical properties obtained from the laboratory testing (Table 4.1).

Table 4.1 Summary of mechanical properties used in models.

Properties	VTF (Hanging wall)	SLR (Footwall)	Fault
Density (g/cm^3)	2.73	2.84	2.03
Compressive strength (MPa)	16.14	15.42	-
Elastic modulus (GPa)	20.16	14.57	-
Poisson's ratio	0.26	0.22	-
Cohesion (kPa)	104.69	89.10	128.74
Friction angle ($^\circ$)	28.4	27.1	14.0

The slope height, fault width, and fault angle are maintained constant at 100 m, 10 m and 63 degrees. The distance between the toe and right boundary is 100 m and between the crest and left boundary is 150 m. The cohesion and friction angle of VTF (hanging wall) are assumed in models to determine effect of shear strength and maintained constant shear strength of SLR (footwall) and fault. The test variables include slope face angle (ψ), distance X , fault angle (α), hanging wall cohesion (c_{hang}) and friction angle (ϕ_{hang}), as shown in Table 4.2. Initial stress due to gravitational loading is first calculated from the density of the overburden. All computer models assume plane strain condition. To cover the entire range of the slope dimensions, over 3,000 triangular elements have been performed to obtain correct simulation results. The data iteration of about 19,600 cycles are performed. Figures 4.1 and 4.2 illustrate representative boundary conditions and meshes of slope model.

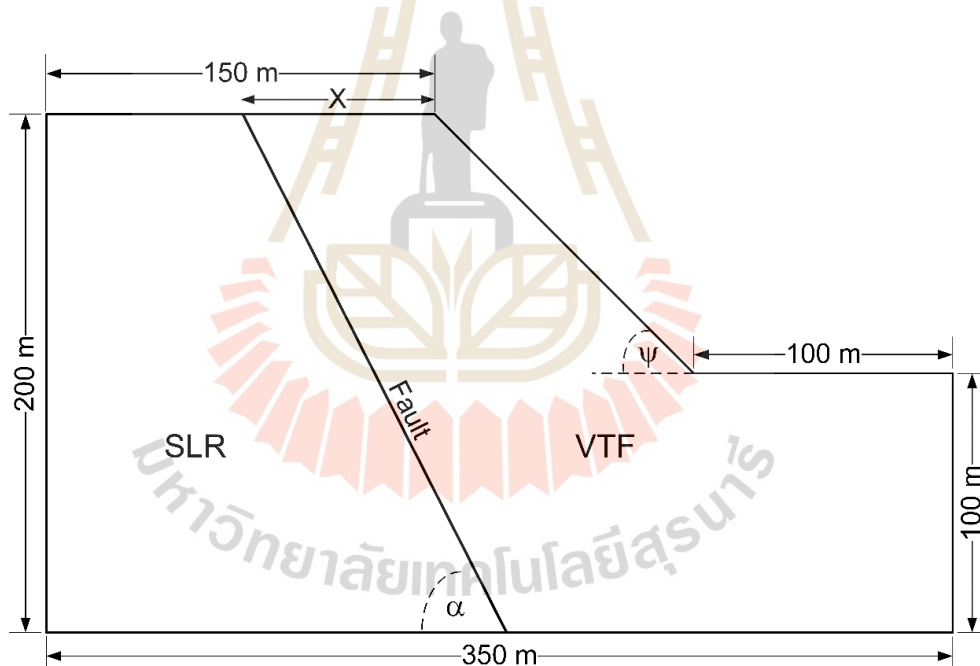


Figure 4.1 Boundary conditions and geometry of the representative slope model.

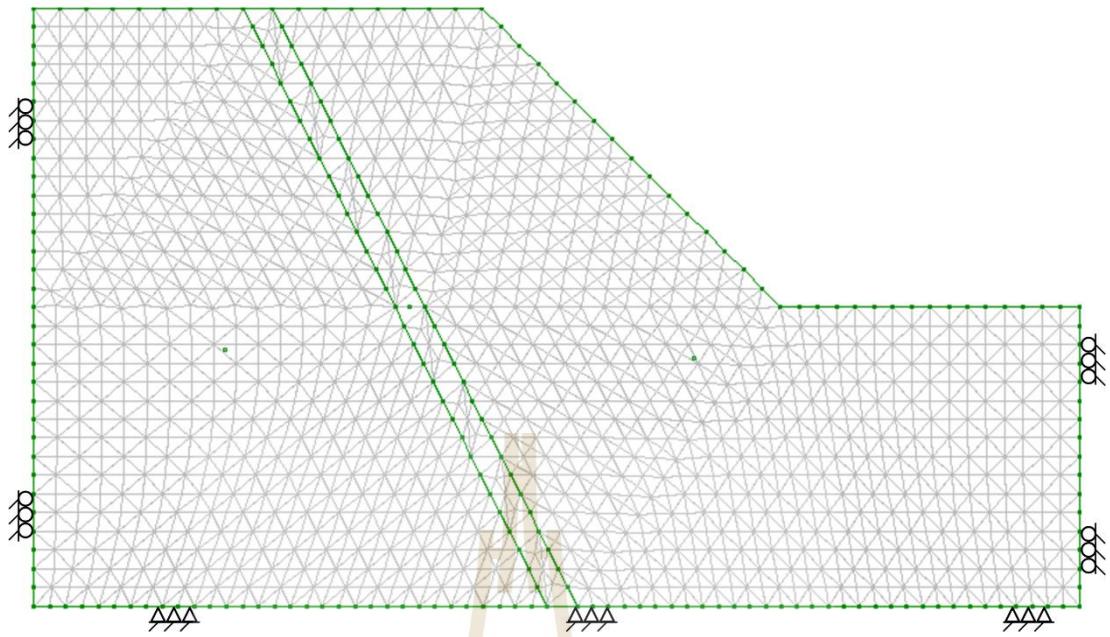


Figure 4.2 Mesh model.

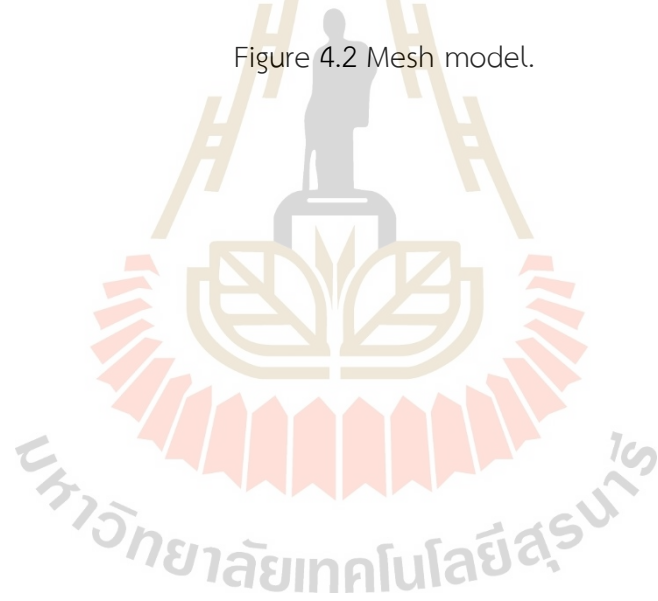
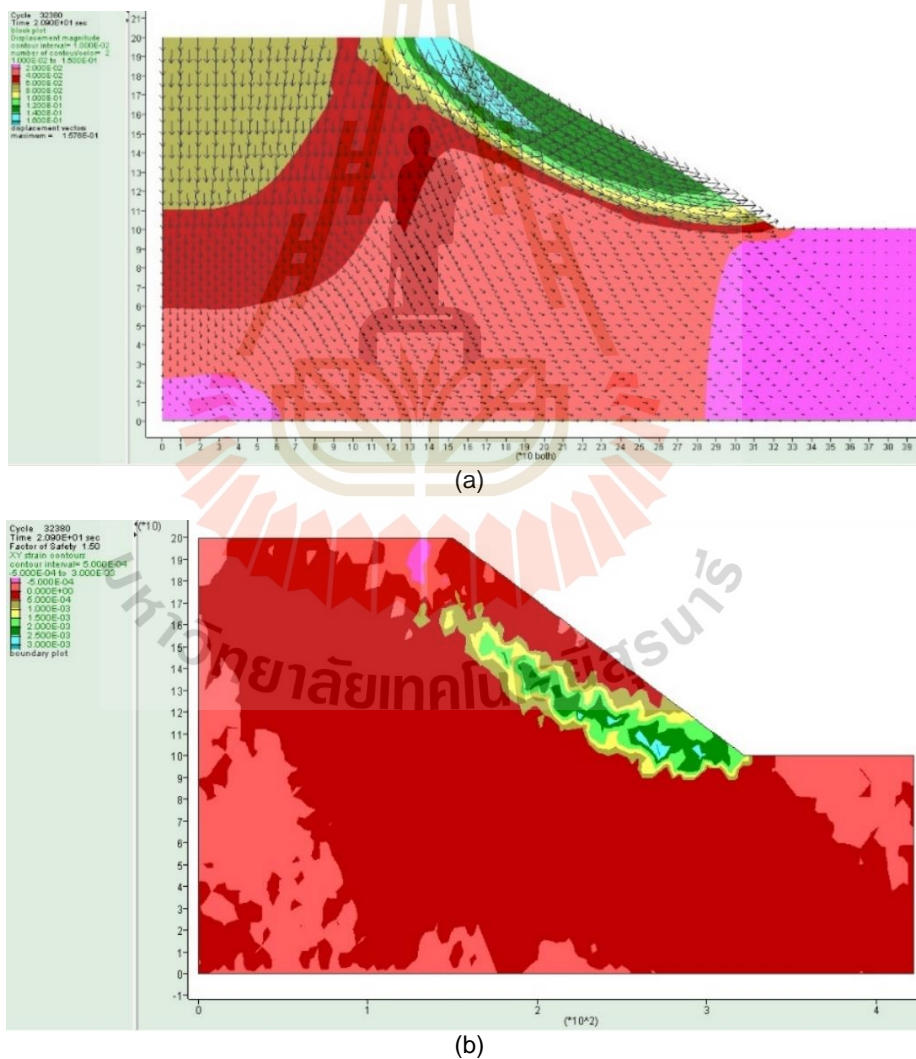


Table 4.2 Parameters used in UDEC simulations.

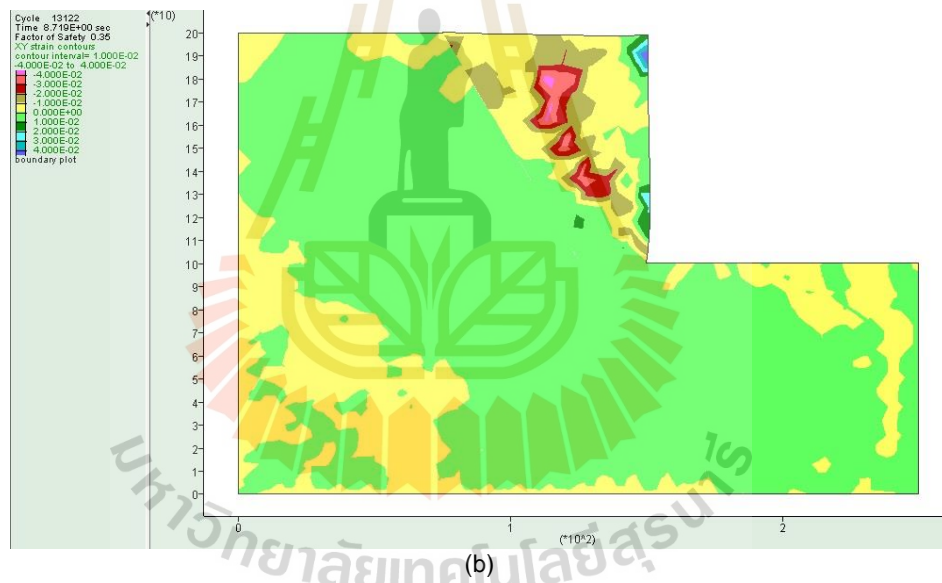
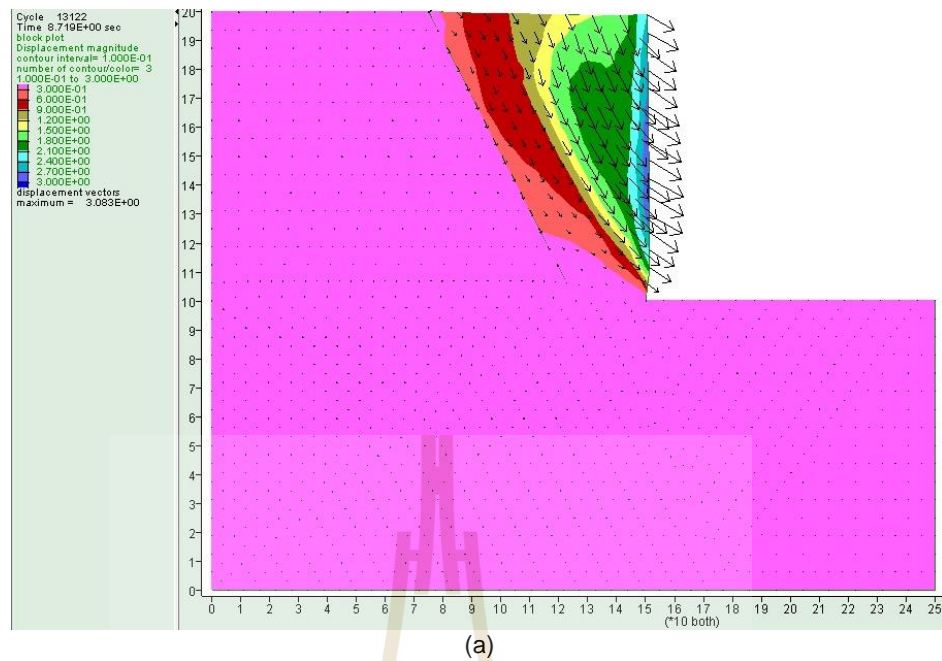
Series	Variable parameters	Constant parameters
I	Slope face angle (Ψ)	30°
		40°
		50°
		60°
		70°
		80°
		90°
II	Distances between fault and crest (X)	25 m
		50 m
		75 m
		100 m
		125 m
III	fault angle (α)	40°
		50°
		63°
		70°
		80°
IV	Cohesion of hanging wall (C_{hang})	0.01 MPa
		0.05 MPa
		0.10 MPa
		0.15 MPa
		0.20 MPa
		0.30 MPa
		0.50 MPa
		1.00 MPa
		2.00 MPa
V	Friction angle of hanging wall (ϕ_{hang})	22.5°
		25.0°
		28.4°
		30.0°
		32.5°
		35.0°

4.2.1 Effect of slope face angle

The slope face angles (ψ) are varied from 30°, 40°, 50°, 60°, 70°, 80° to 90°. The slope height and distance between fault and crest are constant at 100 m and 75 m, respectively. The mechanical properties of footwall, hanging wall and fault are constant (Table 4.1). Figures 4.3 and 4.4 show displacement vectors, shear strains and factor of safety of slope face angles 30 and 90 degrees, respectively. Figure 4.5 shows the factor of safety (FS) as a function of ψ . The results indicate that FS decrease with increasing slope face angle. This agrees well with the results concluded by Igwe and Chukwu (2018) that the overall slope angle decrease with increasing FS.



Figures 4.3 Displacement vectors (a), shear strains and factor of safety (b) of slope face angle 30°



Figures 4.4 Displacement vectors (a), shear strains and factor of safety (b) of slope face angle 90°

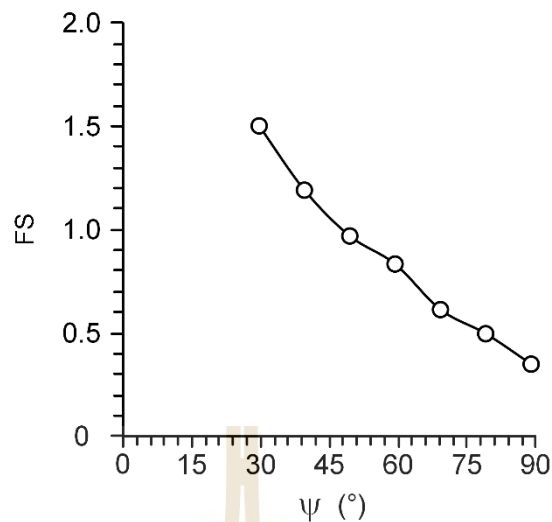
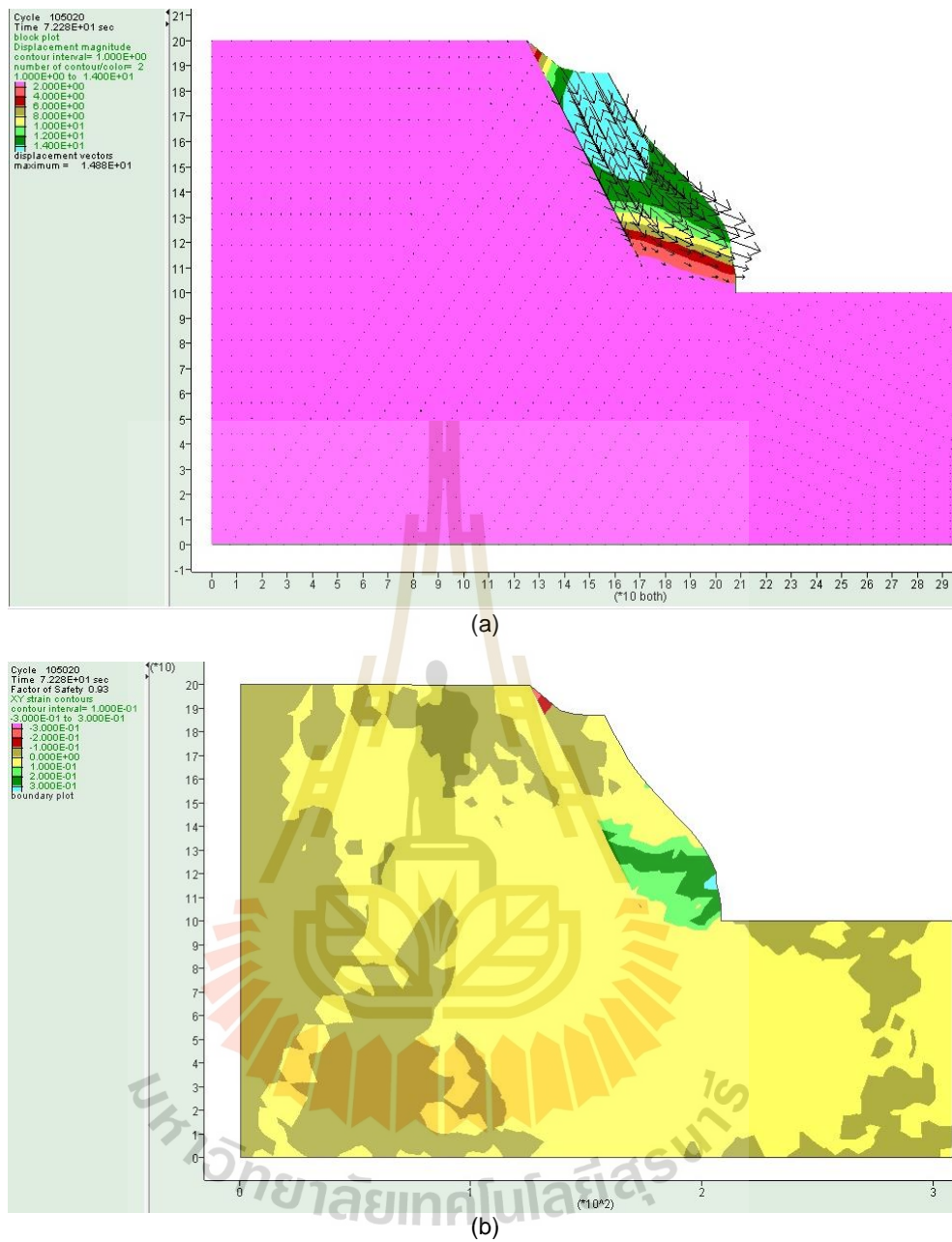


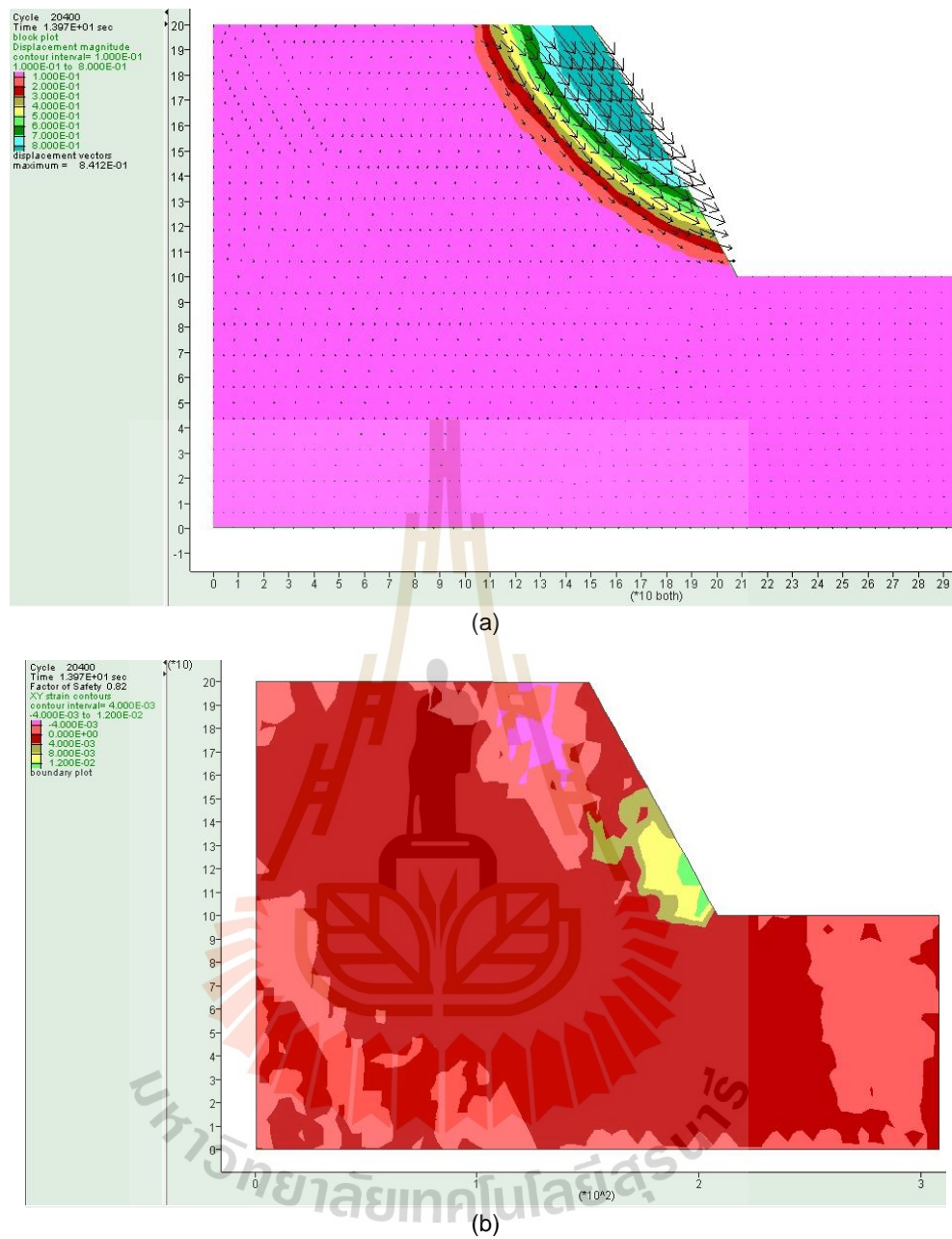
Figure 4.5 Factors of safety as a function of slope angle (ψ).

4.2.2 Effect of distance between fault and crest

The distance between fault and crest (X) are varied from 25, 50, 75, 100 to 125 m. The slope height and slope face angle are constant at 100 m and 60° , respectively. The mechanical properties of footwall, hanging wall and fault are maintained constant. Figures 4.6 and 4.7 show displacement vectors, shear strains and factor of safety of X 25 and 125 m, respectively. Figure 4.8 shows the factor of safety (FS) as a function of X . The results indicate that FS increase with increasing distance between fault and crest.



Figures 4.6 Displacement vectors (a), shear strains and factor of safety (b) of distance between fault and crest is 25 m.



Figures 4.7 Displacement vectors (a), shear strains and factor of safety (b) of distance between fault and crest is 125 m.

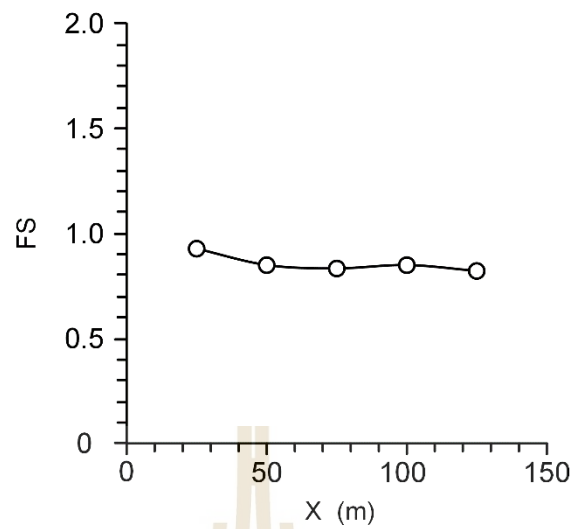
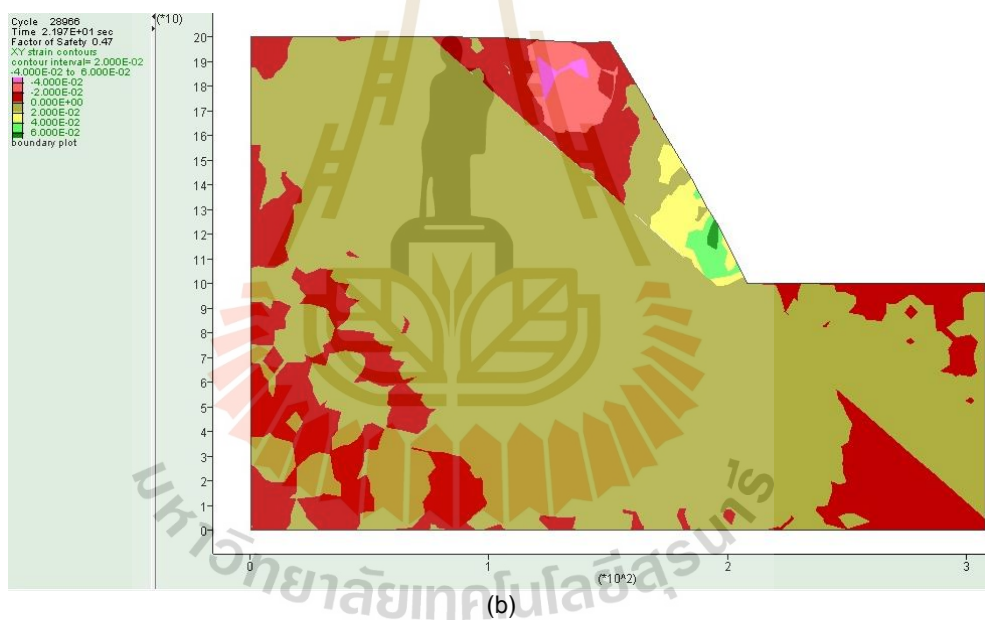
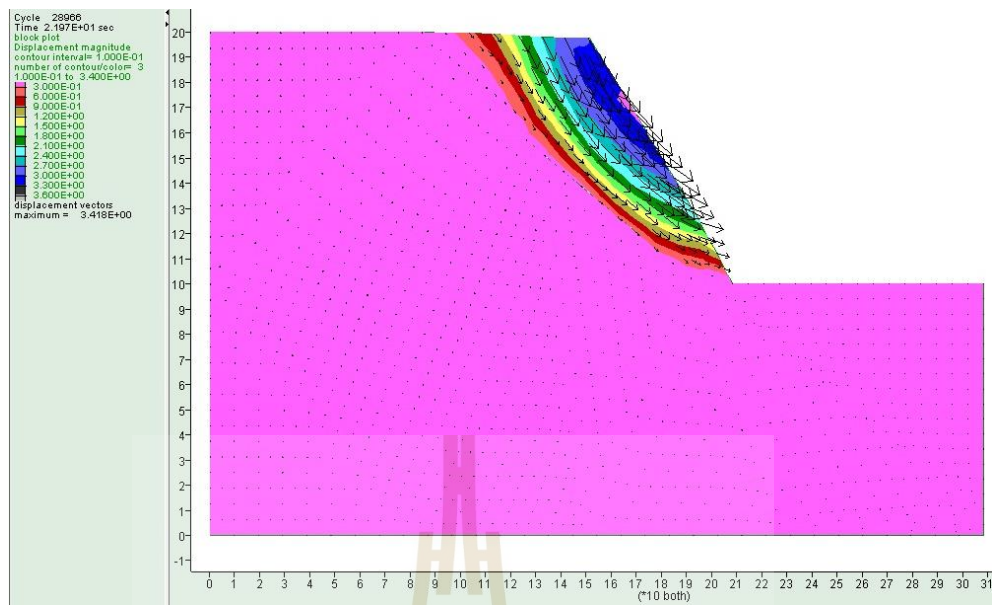


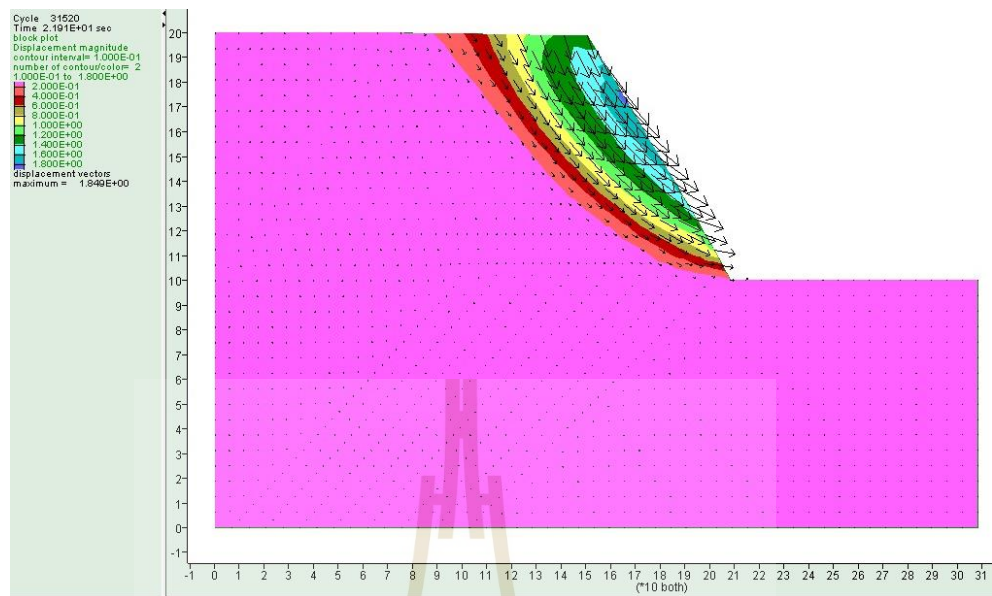
Figure 4.8 Factors of safety as a function of distance between fault and slope crest (X).

4.2.3 Effect of fault angle

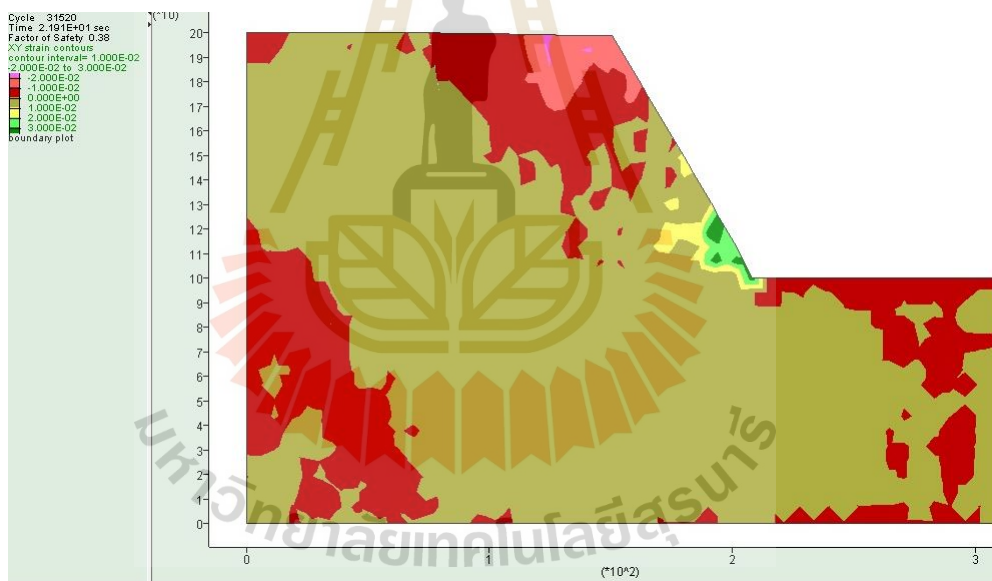
The fault angle (α) are varied from 40, 50, 63, 70 and 80 degrees. The slope height and slope face angle are constant at 100 m and 60° , respectively. The mechanical properties of footwall, hanging wall and fault are maintained constant. Figures 4.9 and 4.10 show displacement vectors, shear strains and factor of safety of α 40 and 80 degrees, respectively. Figure 4.11 shows the factor of safety (FS) as a function of α . The results indicate that α is not sensitive to the FS.



Figures 4.9 Displacement vectors (a), shear strains and factor of safety (b) of fault angle 40 degrees.



(a)



(b)

Figures 4.10 Displacement vectors (a), shear strains and factor of safety (b) of fault angle 80 degrees.

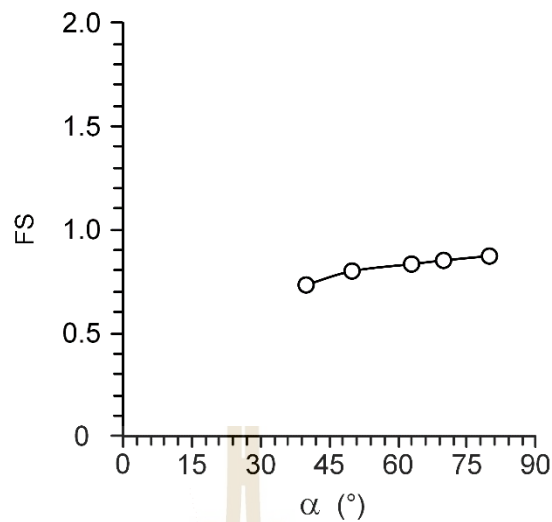
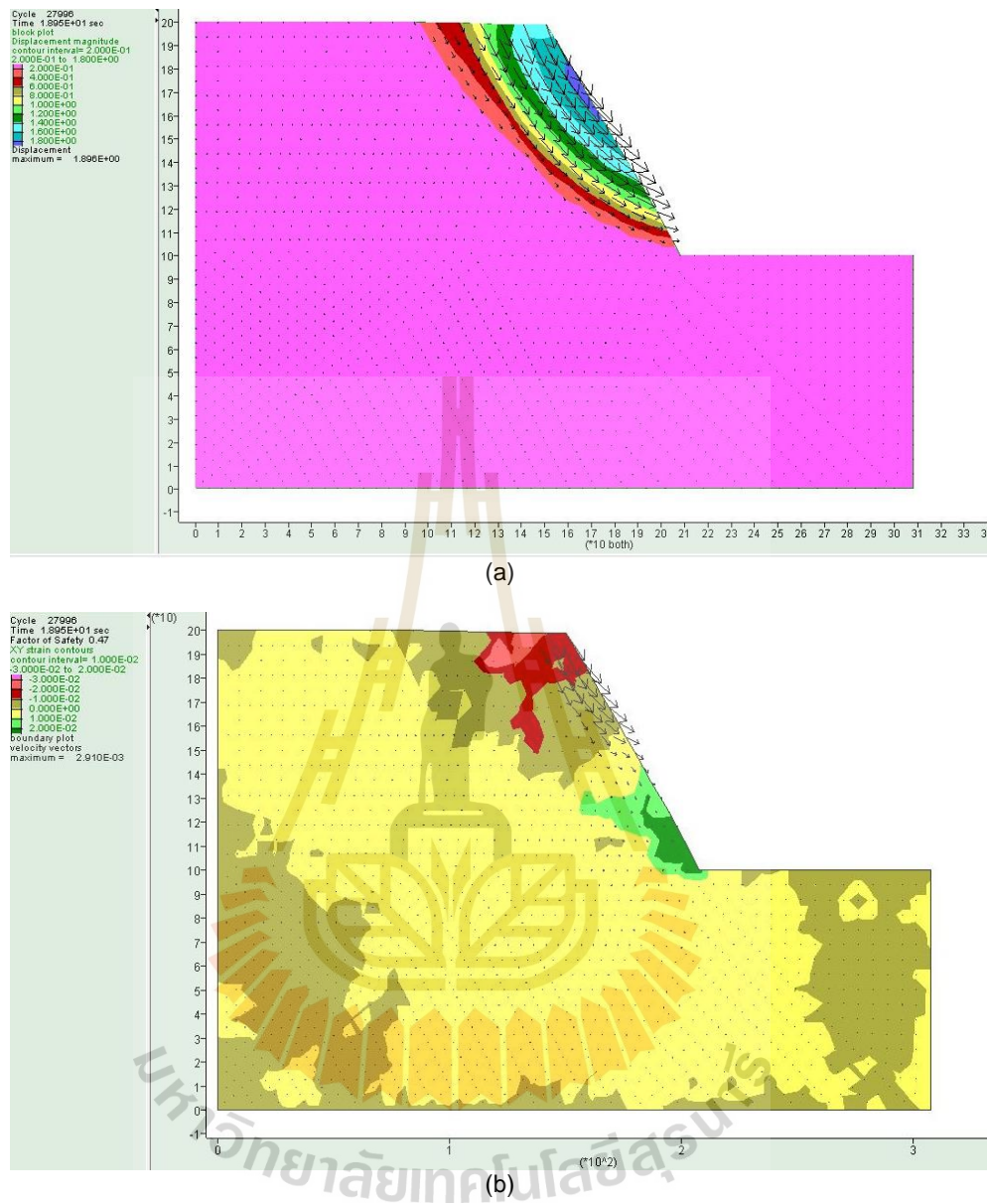


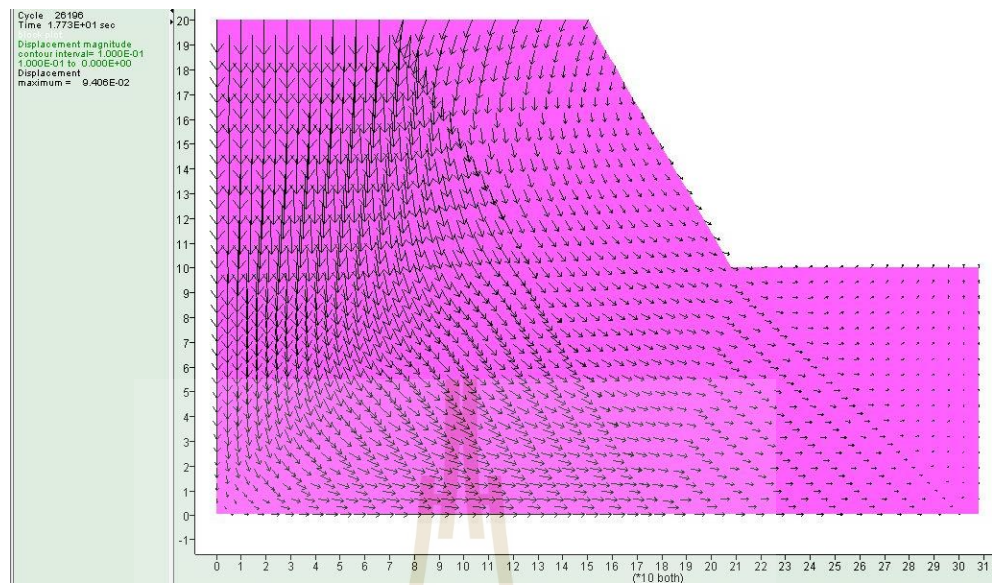
Figure 4.11 Factors of safety as a function of fault angle (α).

4.2.4 Effect of mechanical properties of hanging rock

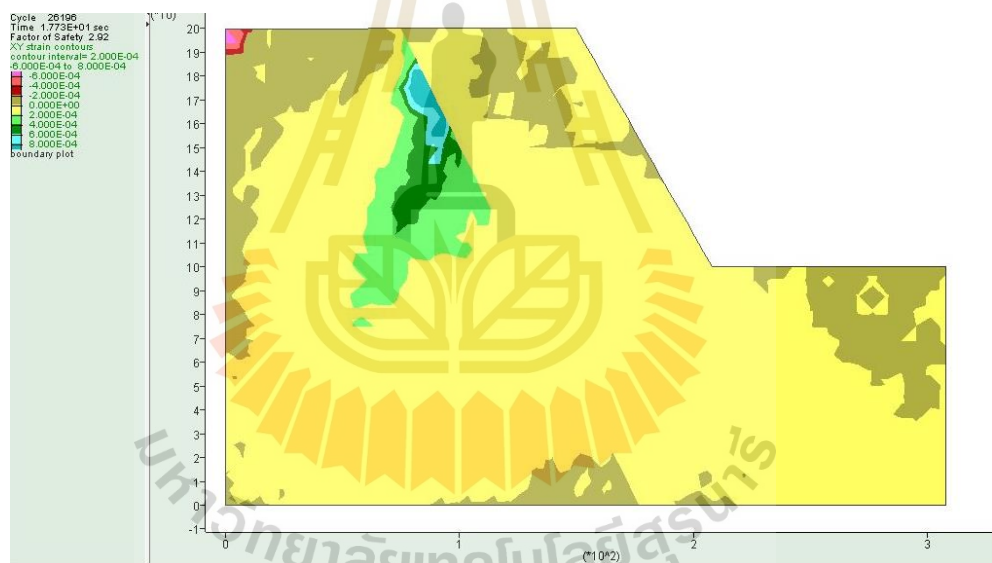
The cohesions of hanging rock (c_{hang}) are assumed varying from 0.01, 0.05, 0.10, 0.20, 0.30, 0.50, 1.00 to 2.00 MPa. The friction angles (ϕ_{hang}) are varied from 22.5°, 25.0°, 28.4°, 30.0°, 32.5° to 35°. The slope face angle and height are constant at 60° and 100 m, respectively. The mechanical properties of footwall and fault are constant. Figures 4.12 and 4.13 show displacement vectors, shear strains and factor of safety of c_{hang} 0.01 and 2.00 MPa, respectively. Figures 4.14 and 4.15 show displacement vectors, shear strains and factor of safety of ϕ_{hang} 22.5 and 35.0 degrees, respectively. Figure 4.16 illustrates FS as a function of ϕ_{hang} under various c_{hang} . The results show that FS increase with increasing ϕ_{hang} and c_{hang} . The results are consistent with Abramson et al. (2001), Muthreja (2012), Coulibaly et al. (2017) and Kumnadi (2017) that increasing of both strength parameters (cohesion and friction angle) have been reported to increase the slope stability.



Figures 4.12 Displacement vectors (a), shear strains and factor of safety (b) of c_{hang} 0.01 MPa.

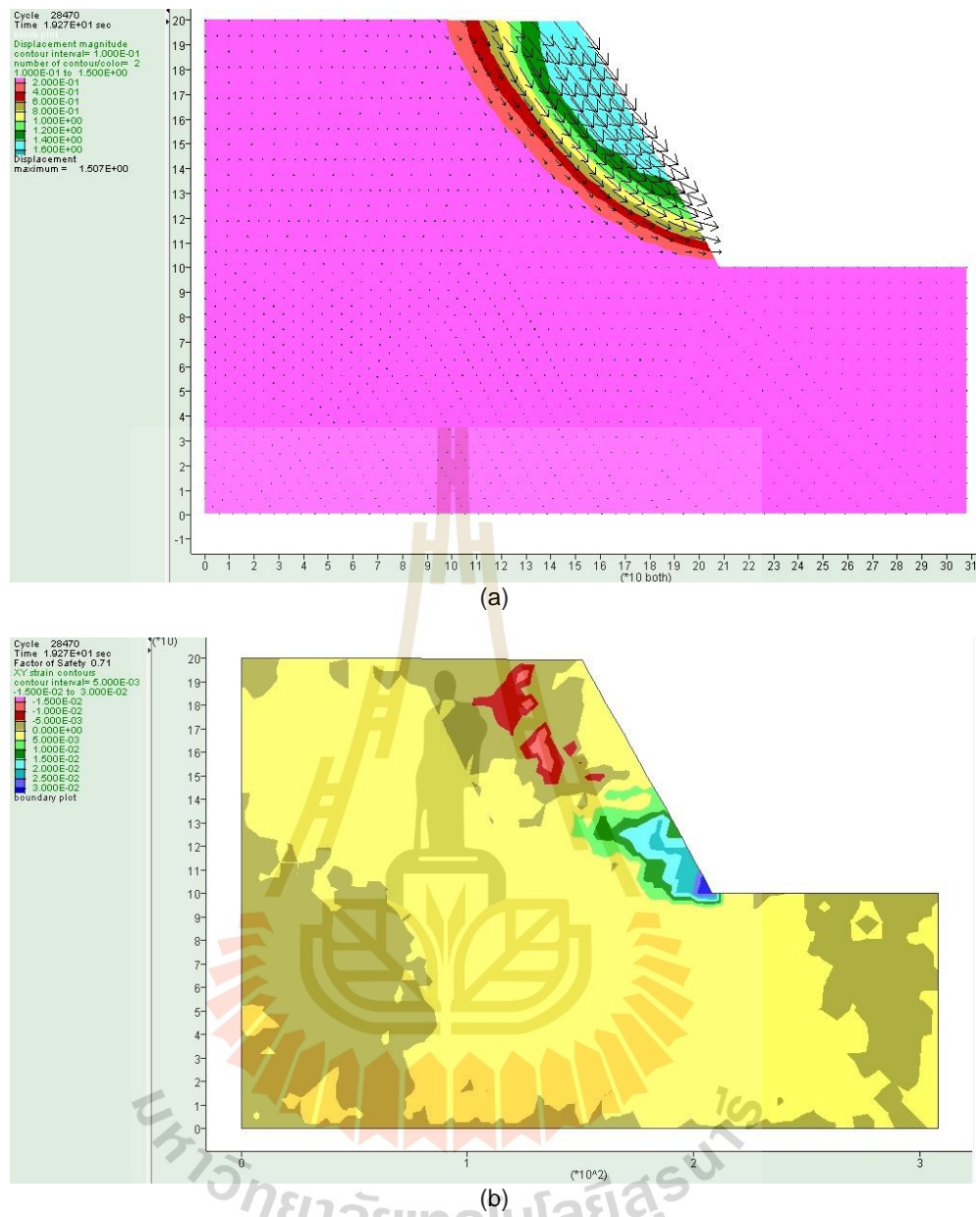


(a)

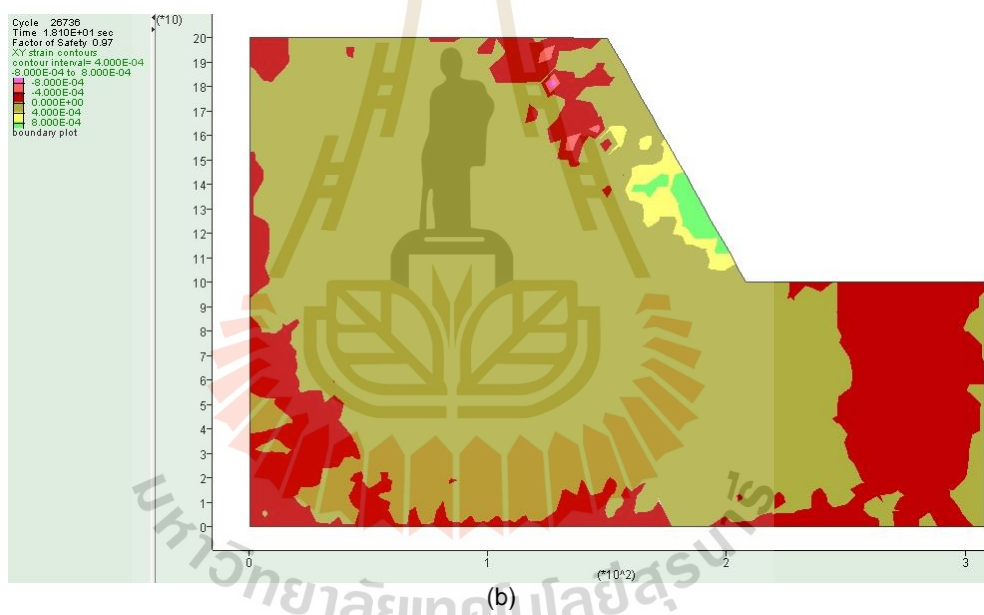
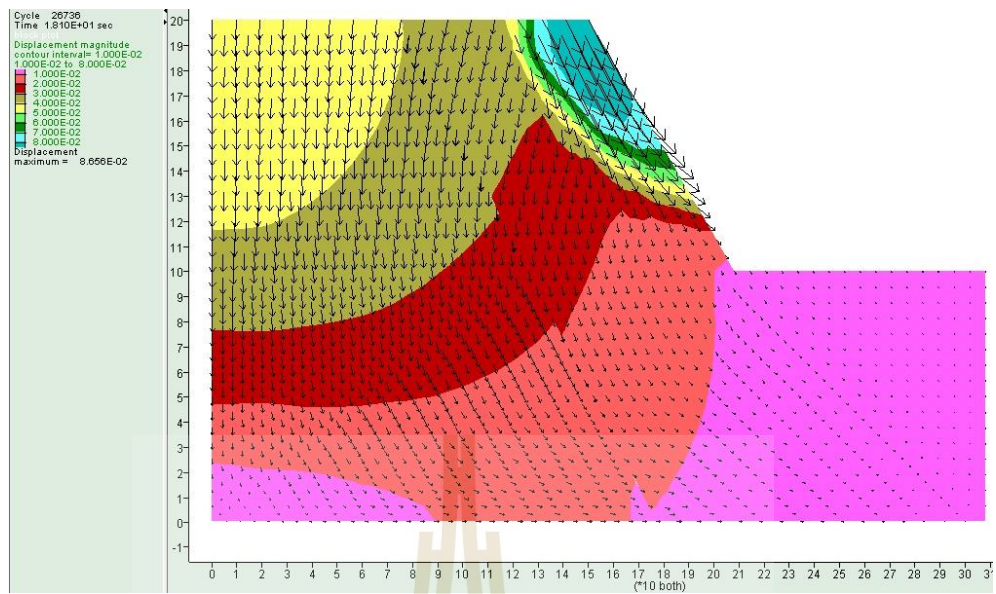


(b)

Figures 4.13 Displacement vectors (a), shear strains and factor of safety (b) of c_{hang} 2.00 MPa.



Figures 4.14 Displacement vectors (a), shear strains and factor of safety (b) of ϕ_{hang} 22.5 degrees.



Figures 4.15 Displacement vectors (a), shear strains and factor of safety (b) of $\phi_{\text{hang}} 35.0$ degrees.

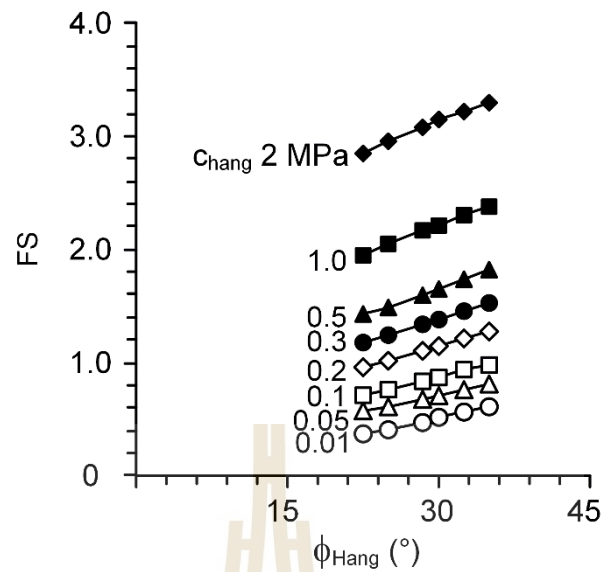


Figure 4.16 Factors of safety as a function of hanging wall friction angle (ϕ_{hang}) various cohesion of hanging rock (c_{hang})

4.3 Prediction

The mathematical relationship is derived here using the simulation results. The empirical equation can be used to predict the safety factor of slopes under various slope face angles, cohesions and friction angles of the hanging wall. Distances between fault from crest and fault angles are not derived in equation because they are not sensitive to the factor of safety. Regression analyses are performed using the SPSS code (Wendai, 2000) to fit the model results with the derived empirical equation. An indicator of the predictive capability of equation is the correlation coefficient (R^2).

Figure 4.17 plots the FS as a function of friction angle of hanging wall which is normalized by slope face angle, fault angle and friction angle of fault ($\phi_{hang} \cdot \alpha / \phi_{flt} \cdot \psi$). The relation between the FS, ($\phi_{hang} \cdot \alpha / \phi_{flt} \cdot \psi$) and c_{hang}/c_{flt} can be best represented by:

$$FS = [0.335 \cdot (c_{hang}/c_{flt})^{0.18} \cdot (\phi_{hang} \cdot \alpha / \phi_{flt} \cdot \psi)] + 0.269 \cdot (c_{hang}/c_{flt})^{0.737} \quad (4.1)$$

The empirical constants in the equation above are generated from the linear regression analysis of the model simulation results. The R^2 of 0.997 indicates a good correlation with the data.

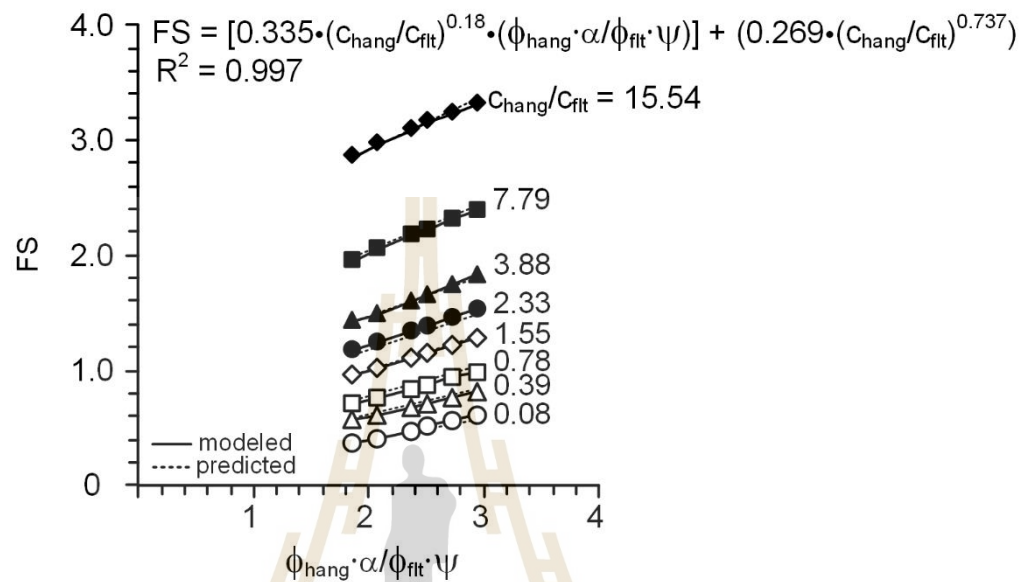


Figure 4.17 Predicted FS as a function of $\phi_{hang} \cdot \alpha / \phi_{fit} \cdot \psi$ under various C_{hang}/C_{fit}

CHAPTER V

DISCUSSIONS AND CONCLUSIONS

5.1 Discussions

In this study, Empirical equation for determination of safe pit slope geometry was collected of drill core specimens of Red Bed siltstone (Footwall), Tuff (Hanging wall) and faults collected from South Wall area of Phu Kham open pit mine in Xaisomboun Province, Lao PDR are studied through laboratory testing. Direct shear tests are carried out on these specimens. The number of rock material specimens used here is adequately represented behaviors of the rock mass, even though, the sample number of fault material specimens to be limited because thin fault zone (5–10 meter thickness) when drilled interested with fault zone.

Numerical simulation is performed to demonstrate the material behaviors on rock slope stability by using UDEC because this software can simulate the slope failures from structural controls and the behavior of discontinuous materials. Thirty-two numerical models are simulated in this study with the same boundary conditions and basic properties of rock at the footwall and fault. These models are adequate to demonstrate the behaviors of rock mass from the Phu Kham mine. Effect of groundwater is not considered in this study because the Phu Kham mine has been drilled horizontal holes for groundwater depressurization.

The findings from this study indicate that the factors affecting the factor of safety of slope are the slope face angle and shear strength properties of hanging rock (friction angle and cohesion). The results obtained here agree reasonably well with those from other researchers (Muthreja, 2012; Coulibaly et al., 2017; Kusnadi, 2017 and Igwe and Chukwu, 2018) that factor of safety increases with increasing friction angle and cohesion, but it decreases with increasing slope face angle.

The proposed empirical equation may be used as a predictive tool to estimate the factor of safety of slope, based on slope face angle, fault angle, cohesion and friction angle of hanging rock and fault. Equation (4.1) is applicable for slope of open

pit in metal mining, the material with cohesion beyond 0.01 MPa and friction angle beyond 22.5 degrees with the overall slope face angles between 30 and 90 degrees and slope height is 100m. As evidenced by the good correlation coefficients ($R^2 > 0.9$) obtained from the proposed empirical equation, the model results are believed to be reasonably reliable.

Comparison of factor of safety (FS) for pit slope geometry obtained from the developed empirical equation with different numerical simulation methods such as Distinct Element Method (DEM), Finite Element Method (FEM) and Limit Equilibrium Method (LEM) are performed. The results indicated that FS of empirical equation, DEM, LEM, and FEM are similar (Figure 5.1 and 5.2).

Scenario 1 :

When : Slope high (H)	= 100m
Slope angle (ψ)	= 60 deg
Slope of Fault (α)	= 63deg
Fault distance (x)	= 75 m
Cohesion of Hanging wall (c_{hang})	= 0.25 MPa
Friction angle of hanging wall (ϕ_{hang})	= 27 deg
Cohesion of Fault (c_{ftt})	= 0.12 MPa
Friction angle Fault (ϕ_{ftt})	= 15 deg

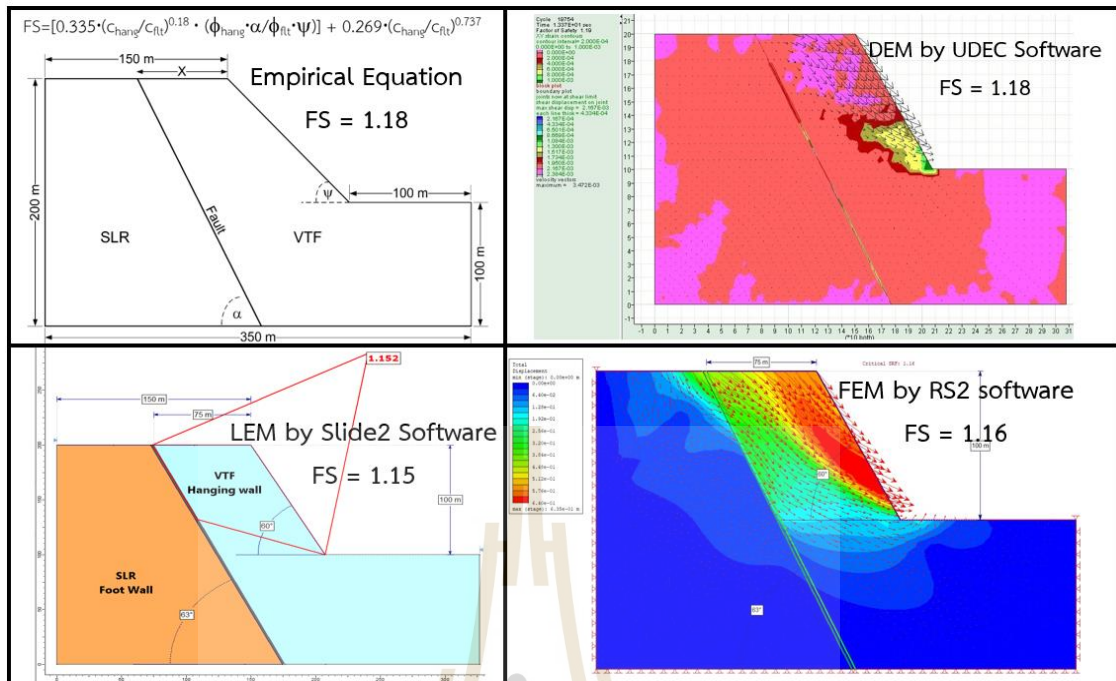


Figure 5.1 Comparison Factors of safety of empirical equation, DEM, LEM, and FEM (Scenario 1)

Scenario 2 :

When : Slope high (H)	= 100m
Slope angle (ψ)	= 50 deg
Slope of Fault (α)	= 63deg
Fault distance (x)	= 75 m
Cohesion of Hanging wall (c_{hang})	= 0.75 MPa
Friction angle of hanging wall (ϕ_{hang})	= 31 deg
Cohesion of Fault (c_{flt})	= 0.12 MPa
Friction angle Fault (ϕ_{flt})	= 15 deg

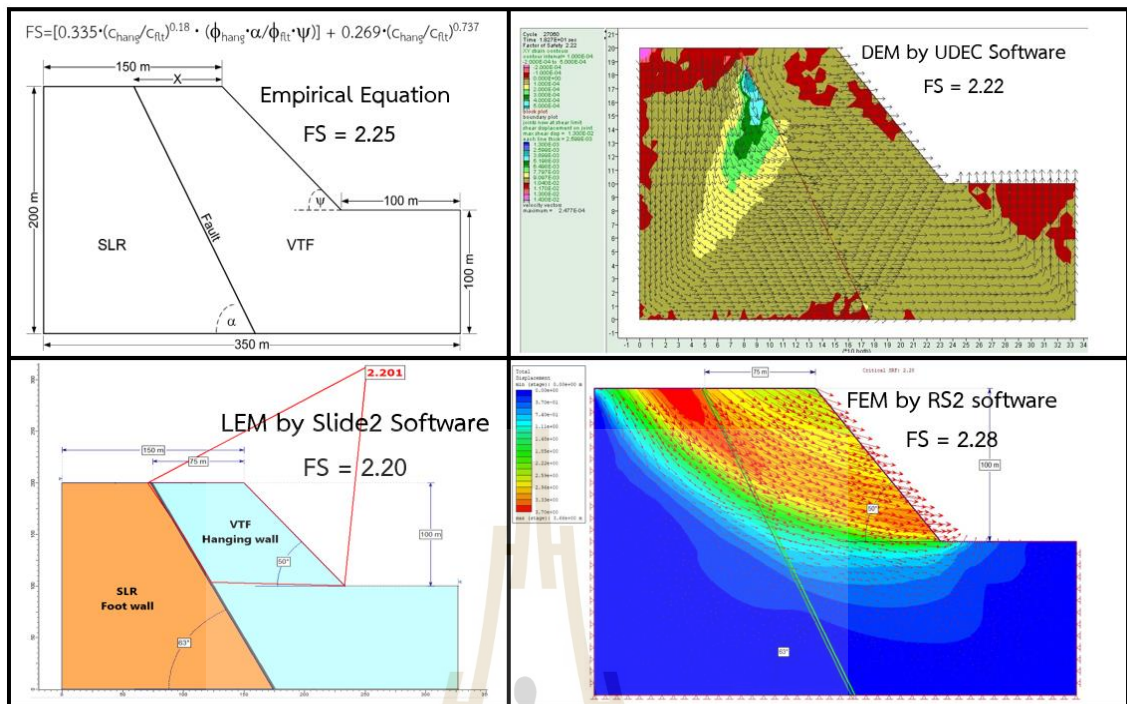


Figure 5.2 Comparison Factors of safety of empirical equation, DEM, LEM, and FEM (Scenario 2)

5.2 Conclusions

Conclusion drawn from this research can be summarized as follows:

- 1) A quick and reliable empirical equation is needed to keep up with rapid excavation of mine slope.
- 2) Comparison Factor of Safety (FS) of empirical equation, DEM, LEM, and FEM are similar.
- 3) Increasing slope face angle decreases slope stability but increasing distance between fault and crest increases the stability.
- 4) The factor of safety is dependent of the fault angle. This can be attributed to the fault being a thin layer located at a considerable distance from both the crest and toe of the slope.
- 5) The enhancement of shear strength parameters, such as cohesion and friction angle, can result in an increase in slope stability, as these parameters are

directly related to the resisting forces that act against slope failure. Increasing cohesion and friction angle leads to the increase of resisting forces that prevent slope failure.

5.3 Recommendations for future studies

The limitations of this study and results discussed above lead to suggestions for further research.

(1) The laboratory testing for hanging rock, footwall and fault have been a limited diversity of material. To confirm the conclusions drawn in this study, more testing in a variety of rock and soil is required.

(2) The numerical simulations should be performed with various material types.

(3) Monitoring of the actual slope behavior is desirable to validate the method and results obtained from this study.

(4) The effect of shear rate should be investigated. Lower shear rates should be performed as they would represent the loading rate closely to the actual mining operation.

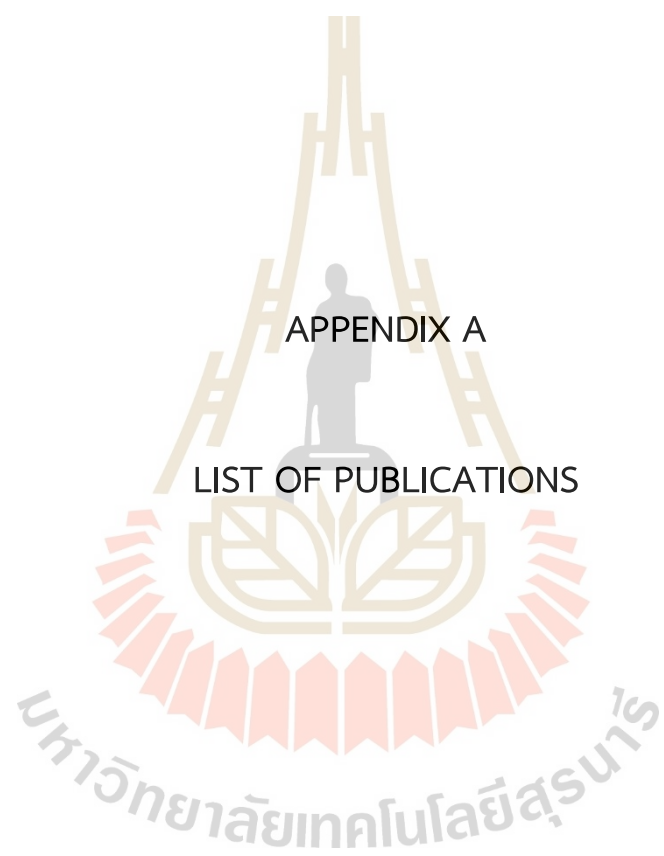


REFERENCES

- Abramson, L. W., Lee, T. S., Sharma, S., and Boyce, G. M. (2001). *Slope stability and stabilization methods*. John Wiley & Sons.
- ASTM D5607-08. Standard test method for performing laboratory direct shear strength tests of rock specimens under constant normal force. *Annual Book of ASTM Standards* (Vol. 04.08). Philadelphia: American Society for Testing and Materials.
- Barton, N. (1973). Review of a new shear-strength criterion for rock joints. *Engineering Geology*, 7(4): 287-332.
- Barton, N., and Choubey, V. (1977). The shear strength of rock joints in theory and practice. *Rock Mechanics*, 10(1-2): 1-54.
- Basahel, H. and Mitri, H. (2017). Application of rock mass classification systems to rock slope stability assessment- a case study. *Journal of Rock Mechanics and Geotechnical Engineering*, 9: 993-1009.
- Bhasin, R. and Kaynia, A. M. (2004). Static and dynamic simulation of a 700-m high rock slope in Western Norway. *Engineering Geology*. 71: 213-226.
- Bieniawski, Z. T. (1989). *Engineering rock mass classifications: a complete manual for engineers and geologists in mining, civil, and petroleum engineering*. John Wiley & Sons.
- Coggan, J. S., Stead, D. and Eyre, J. M. (1998). Evaluation of techniques for quarry slope stability assessment. *Applied Earth Science*, 107.
- Coulibaly, Y., Belem, T., and Cheng, L. (2017). Numerical analysis and geophysical monitoring for stability assessment of the northwest tailings dam at Westwood Mine. *International Journal of Mining Science and Technology*, 27(4): 701-710.
- Deliveris, A. V., Zevgolis, I. E., and Koukoulas, N. C. (2019). Slope failure incidents and other stability concerns in surface lignite mines in Greece. *Journal of Sustainable Mining*, 18(4): 182-197.
- Fawaz, A., Farah, E., and Hagechade, F. (2014). Slope stability analysis using numerical modelling. *American Journal of Civil Engineering*, 2(3): 60-67.

- Grasselli, G., and Egger, P. (2003). Constitutive law for the shear strength of rock joints based on three-dimensional surface parameters. *International Journal of Rock Mechanics and Mining Sciences*, 40(1): 25-40.
- Hoek, E., and Bray, J. D. (1981). *Rock Slope Engineering*. The Institute of Mining and Metallurgy, London.
- Hoek, E., Kaiser, P.K. and Bawden. W.F. (1995). *Support of Underground Excavations in Hard Rock*. Rotterdam: Balkema.
- Itasca, (2011). U.D.E.C. Version 5.0 User's Manuals. Itasca Consulting Group, Minneapolis.
- Itasca, (2007) *3DEC version 4.1, 3 Dimensional Distinct Element Code user's manuals*. Itasca Consulting Group, Minneapolis.
- Igwe, O. and Chukwu, C. (2018). Evaluation of the mechanical properties and critical slope parameters of mine tailings at Enyigba, south eastern, Nigeria. *International Journal of Geo-Engineering*, 9(1): 1-25.
- King, S. (2015). Structural geology, face mapping and fault modelling of the Phu Kham Mine, Laos. *Soild Geology Ltd Report to Phu Bia Mining*, August 2015.
- Kusnadi, S. (2017). Slope stability analysis based on type, physical and mechanical properties rock in Teluk Pandan District, East Kutai Regency, East Kalimantan. *Journal of Geoscience, Engineering, Environment, and Technology*, 2(4): 272-277.
- Ladanyi, B. and Archambault, G. (1970). Simulation of shear behavior of a jointed rock mass. *In Proceeding 11th symposium on Rock Mechanics* (pp. 105-125). New York: Society of Minig Engineers, AIME.
- Li, S. H., Wang, J. G., Liu, B. S., and Dong, D. P. (2007). Analysis of critical excavation depth for a jointed rock slope using a face-to-face discrete element method. *Rock Mechanics and Rock Engineering*, 40(4): 331.
- Muthreja, I. L., Yerpude, R. R., and Jethwa, J. L. (2012). Role of site selection on the stability of surface coal mine waste dumps. *Indian Mining and Engineering Journal*, 51(9).

- Nikolić, M., Roje-Bonacci, T., and Ibrahimbegović, A. (2016). Overview of the numerical methods for the modelling of rock mechanics problems. *Tehnicki Vjesnik-Technical Gazette*. 23(2): 627-637.
- Patton, F. D. (1966). Multiple modes of shear failure in rock. In *1st ISRM Congress. International Society for Rock Mechanics and Rock Engineering*.
- Price, N. J. and Cosgrove, J. W. (1990). *Analysis of geological structures*. Cambridge, England: Cambridge University Press.
- Romer, C. and Ferentinou, M. (2019). Numerical investigations of rock bridge effect on open pit slope stability. *Journal of Rock Mechanics and Geotechnical Engineering*, 11: 1184-1200.
- Severin, J., Eberhardt, E., and Fortin, S. (2013). Open pit numerical model calibration using a pseudo three-dimensional radar monitoring technique. In *Proceedings of the 2013 International Symposium on Slope Stability in Open Pit Mining and Civil Engineering* (pp. 639-652). Australian Centre for Geomechanics.
- Tate, N. (2005). Geology model Phu Kham copper-gold deposit. *Proprietary Report for Phu Bia Mining*.
- Wyllie, D.C. and C.W. Mah (2005). *Rock Slope Engineering: Civil and mining*, 4th edition Spon Press, Taylor & Francis Group, London, UK., 431 pp.
- Zhou, J. W., Shi, C., and Xu, F. G. (2013). Geotechnical characteristics and stability analysis of rock-soil aggregate slope at the Gushui Hydropower Station, Southwest China. *The Scientific World Journal*, 2013: 1-16.



APPENDIX A

LIST OF PUBLICATIONS

List of Publications.

Wasan saranart, Thanittha thangrapha, Kittitep fuenkajorn (2022) Derivation of Empirical Equations for Determination of Safe Pit Slope Geometry at Phukham Mining Page(s): 18-22.



DERIVATION OF EMPIRICAL EQUATIONS FOR DETERMINATION OF SAFE PIT SLOPE GEOMETRY AT PHUKHAM MINING

¹WASAN SARANART, ²THANITTHA THONGPRAPHA, ³KITTITTEP FUENKAJORN

^{1,2,3} Geomechanics Research Unit, Institute of Engineering, Suranaree University of Technology, Nakhon Ratchasima, 30000, Thailand
E-mail: ¹w_saranart@hotmail.com

Abstract - Objective of this study is to investigate rock shear strength parameters of fault and shear zone at South Wall of Phu Kham open pit mine by direct shear testing. The test results are simulated in numerical models using distinct element method (UDEC code) under different slope faces and angles and shear strength parameters. The model results indicate that the safety factors of slope increase with increasing cohesions, friction angles and distances between fault and slope face, but decreases with increasing slope face angles. An empirical equation is derived here using the simulation results. It can be used to predict the safety factor of slopes under various slope face angles, cohesions and friction angles of the hanging wall. Distances between fault from crest are not derived in equation because they are not sensitive to the factor of safety.

Keywords - Slope Angle, Fault, Friction Angle

I. INTRODUCTION

Rock slope stability is considered crucial to public safety in engineering project areas, such as open pit mine, dam, road cut, and railway. Slope failure can be affected by rock mass characteristics, slope geometries, groundwater and other operating conditions. Geology comprehension is necessary for rock slope design. In the mining process, small changes in the slope face angle may have large consequences on the mining operation economy. Phu Kham open pit mine is the largest copper reserve in Laos, which is located in PanAust's Phu Bia Mining Contract Area, Xaisomboun Province, Lao PDR. A problem of Phu Kham open pit is slope instability at the South Wall. This location has specific discontinuities that lead to the decrease of the slope stability. To prevent slope failures, several methods have been proposed by researchers. Empirical method or rock mass classification system is often used for preliminary evaluation of rock mass behaviors [2]. It is simple and convenient to use. Numerical method is used for a more complex slope geometry and failure mechanisms. It is useful when the other methods cannot represent rock mass behaviors [9, 10]. Even though the empirical methods have been proposed by many researchers to quantify rock mass behavior, the effort of rock mass classification for specific pit slope design of Phu Kham open pit has rarely been attempted. To correlate the shear strength parameters with the rock slope behavior, empirical equations for predicting the slope failure are needed. Such equations can be readily applied, and hence allows a quick excavation and production of the ore.

The objective of this study is to determine rock shear strength parameters of fault and shear zone at South Wall of Phu Kham open pit mine by direct shear testing. The laboratory results are demonstrated in numerical simulations with a distinct element method using the Universal Distinct Element Code (UDEC) [5]. The numerical results are used to develop

mathematical relationships between shear strength parameters under different factors of safety (FS).

II. LABORATORY TESTINGS

Three types of samples are used in this study. They are volcanic tuff (VTF), Red Beds (SLR), and faults collected from the South Wall zone in the Phu Kham pit. The VTF and SLR, and fault are in hanging wall, footwall, and major fault, respectively (Fig. 1 and 2). All samples are collected from diamond drill cores, there are three groups of sample preparation for different test methods, 1) uniaxial compressive strength tests (UCS), 2) direct shear tests of rock specimens on rough fracture (DS), and 3) direct shear tests of soil samples (DS-soil). The core specimens with a nominal diameter 61 mm (HQ bit size) tested here were drilled from depths ranging between 15.50 to 183.40 m. Twenty-eight of VTF specimens and thirty-one of SLR specimens are cut to obtain a nominal length-to-diameter ratio (L/D) ranging between 2.0 to 2.5 for UCS testing, following the ASTM D7012 standard practice. Six pairs of VTF specimens and ten pairs of SLR specimens are selected from a single discontinuity and cut to have a nominal length 10 cm for DS testing, following the ASTM D5607 standard practice. Three soil samples of fault for DS-soil test are collected for three specimens. They packed in plastic wrap to minimize disturbance, following the ASTM D3080 standard practice. Figs.3 and 4 are show some pre-test and post-test of VTF and SLR samples.

A. Uniaxial Compressive Strength Test (UCS)

The rock strength or compressive strength of the joint walls is required as data input in numerical simulations. The laboratory testing procedure strictly follows the American Society for Testing and Materials (ASTM D7012-14). Cylindrical specimens of VTF and SLR with a nominal diameter of 61 mm and L/D ratio between 2.0 to 2.5 are axially loaded to

failure. Twenty-eight of VTF and thirty-one of SLR specimens have been tested. The UCS is calculated from the maximum load divided by the initial cross-sectional area. The elastic modulus (Young's modulus) is determined from the stress-strain curves at 50% of the maximum stress. Test results are shown in Table 1.

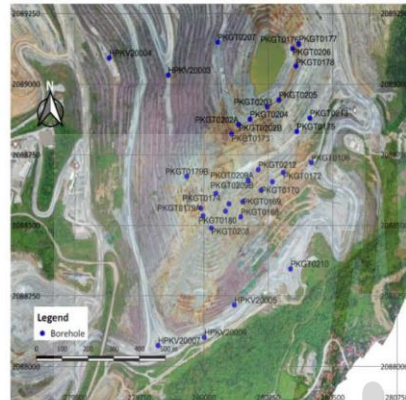


Fig.1. Borehole locations in the study area

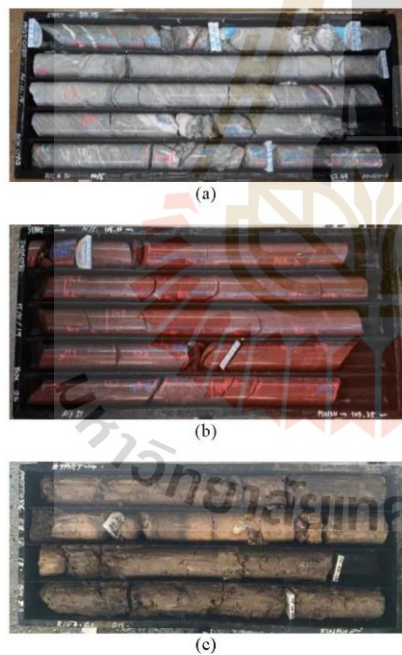


Fig.2. Core samples: VTF (a) and SLR (b) and fault samples (c) collected for testing.



Fig.3. Some VTF (a) and SLR (b) specimens prepared for UCS testing.

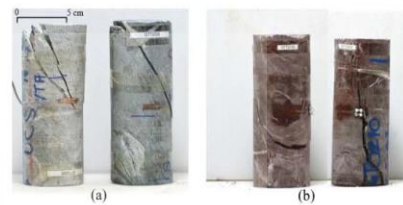


Fig.4. Post-test VTF (a) and SLR (b) specimens of UCS testing

Properties	VTF	SLR
Density (g/cm ³)	2.73 ± 0.08	2.84 ± 0.17
UCS (MPa)	16.14 ± 15.30	15.42 ± 17.54
E (GPa)	20.16 ± 12.10	14.57 ± 7.88
Poisson's ratio	0.26 ± 0.03	0.22 ± 0.04

Table 1 Summary UCS Testing Results

B. Direct shear tests of rock specimens with rough fracture

The rock shear strength is a significant parameter for the design of rock slopes, foundations, and structures. The test procedure is followed the American Society for Testing and Materials standard (ASTM D5607-16) and the method suggested by the International Society of Rock Mechanics (ISRM) [3]. Six pairs of VTF specimens and ten pairs of SLR specimens with a nominal length 10 cm contain discontinuities (i.e., bedding, joint), and are separated into upper and lower halves of the encapsulated cement molds (Fig.5). The shear displacement is applied under constant rate of 0.2 mm/min. A minimum of 10 sets of monitoring and recording data points is suggested to be taken before obtaining the peak shear strength. The loading continues until a residual shear strength is established. Post-test VTF and SLR specimens are shown in Fig.6. The test results are shown in Table 2.

C. Direct shear tests of soil samples

A set of direct shear tests on compacted soil samples has been conducted on fault samples. After compaction, the soil samples are placed and set up in a direct shear load box and frame. All samples are sheared under a constant displacement rate of 0.1 mm/min. The test results are shown in Table 2.

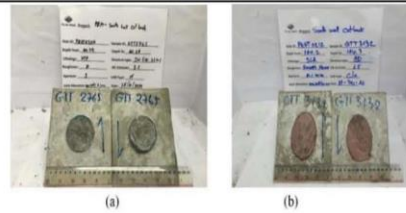


Fig.5. Some VTF (a) and SLR (b) specimens prepared and molded for DS testing.

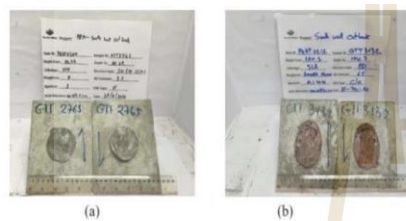


Fig.6. Post-test of VTF (a) and SLR (b) specimens of DS testing.

Properties	VTF	SLR	Fault
Density (g/cm ³)	2.73	2.84	2.03
Cohesion (kPa)	1,000.00	500.00	128.71
Friction angle (°)	35	33	15

Table II Summary DS Testing Results

III. NUMERICAL SIMULATIONS

Discrete element analyses are performed using UDEC [5] to describe the slope stability behavior. The discrete element models are constructed to represent various slope face angles (ψ) and distances between fault and crest (X). The models use mechanical properties obtained from the laboratory testing (Tables 1 and 2). The slope height, fault width, and fault angle are maintained constant at 100 m, 10 m and 63 degrees. The distance between the toe and right boundary is 100 m and between the crest and left boundary is 150 m. The slope face angle (ψ) varies from 45°, 60°, 75° to 90°, and distance X varies from 10, 25, 50, 75 to 100 m. Fig.7 and 8 show representative boundary conditions and meshes of slope model. The cohesion and friction angle of VTF (hanging wall) are assumed in models for determine effect of shear strength and maintained constant shear strength of SLR (footwall) and fault. The cohesion (c_{hang}) varies from 0.1, 0.5, 1.0 to 2.0 MPa, and friction angle (ϕ_{hang}) from 25.0, 27.5, 30.0, 32.5, 35.0 to 37.5. Initial stress due to gravitational loading is first calculated from the density of the overburden. All computer models assume plane strain condition.

Simulation results in the form of displacement vectors are shown in Fig. 9.

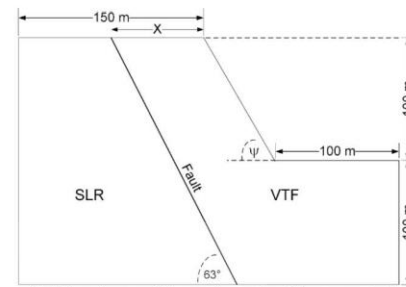


Fig.7. Boundary conditions and geometry of the representative slope model.

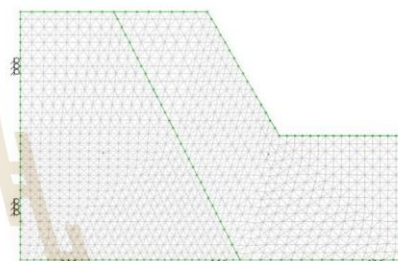


Fig.8. Mesh model.

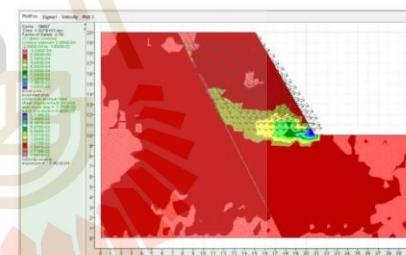


Fig.9. Representative simulation results of displacement vectors.

IV. RESULTS AND DISCUSSIONS

Slope failure is geotechnical hazards that occur due to driving forces overcome resisting forces. The driving force is typically gravity, the resisting force is the shear strengths of slope material. The model results indicate that FS increases with increasing X, c_{hang} and ϕ_{hang} but it decreases with increasing ψ (Figs.10 to 12).The mathematical relationship is derived here using the simulation results. The empirical equation can be used to predict the safety factor of slopes under various slope face angles, cohesions and friction angles of the hanging wall (cohesion and friction angle). Distances between fault from crest are not derived in equation

because they are not sensitive to the factor of safety. Regression analyses are performed using the SPSS code [11] to fit the model results with the derived empirical equation. An indicator of the predictive capability of equation is the correlation coefficient (R^2). Fig. 13 plots the FS as a function of friction angle of hanging wall which is normalized by slope face angle (ϕ_{hang}/ψ). The relation between the FS, ϕ_{hang}/ψ and c_{hang} can be best represented by:

$$FS = 3.4 \tilde{Y}(c_{hang}^{0.458}) \tilde{Y}(f_{hang}/\gamma)^{0.42} \quad (1)$$

The empirical constants in the equation above are generated from the non-linear regression analysis of the model simulation results. The R^2 of 0.997 indicates a good correlation with the data.

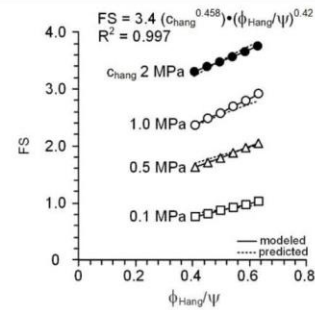


Fig. 13. Predicted FS as a function of ϕ_{hang}/ψ

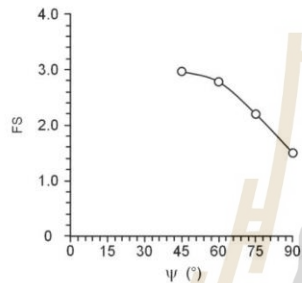


Fig. 10. Factor of safety as a function of slope angle (ψ)

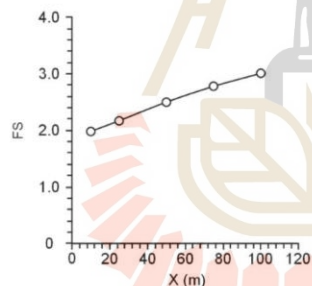


Fig. 11. Factor of safety as a function of fault distance (X)

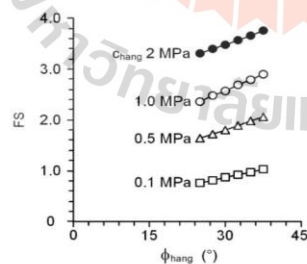


Fig. 12. Factor of safety as a function of hanging wall friction angle (ϕ_{hang})

IV. CONCLUSIONS

Thirty-three numerical models are simulated in this study with the same boundary conditions and basic properties of rock at the footwall and fault. The direct shear tests determine the shear strength parameters of the hanging wall, footwall and fault materials. The simulation results agree well with those of [4, 6, 7, and 8]. The factor of safety depends on shear strength parameters of slope materials and slope face angle, but not sensitive to the distance between fault and slope face.

ACKNOWLEDGMENTS

This study is funded by Suranaree University of Tech. and by the Higher Education Promotion and National Research University of

REFERENCES

- [1] ASTM D5607-08, "Standard Test Method for Performing Laboratory Direct Shear Strength Tests of Rock Specimens Under Constant Normal Force", Annual Book of ASTM Standards (Vol. 04), Philadelphia: American Society for Testing and Materials, 2018.
- [2] H. Basahel, and H. Mitri, "Application of Rock Mass Classification Systems to Rock Slope Stability Assessment- A case study", Journal of Rock Mechanics and Geotechnical Engineering, vol. 9, pp. 993-1009, 2017.
- [3] E. T. Brown, International Society for Rock Mech. Suggested Methods, 1981.
- [4] Y. Coulibaly, T. Belem, and L. Cheng, "Numerical analysis and Geophysical Monitoring for Stability Assessment of the Northwest Tailings Dam at Westwood Mine", International Journal of Mining Science and Technology, vol. 27, no. 4, pp. 701-710, 2017.
- [5] Itasca, U.D.E.C. Version 5.0 User's Manuals, Itasca Consulting Group, Minneapolis, 2011.
- [6] O. Igwe, and C. Chukwu, "Evaluation of the mechanical properties and Critical Slope Parameters of Mine Tailings at Enyigba, Southeastern, Nigeria", International Journal of Geo-Engineering, vol. 9, no. 1, pp. 1-25, 2018.
- [7] S. Kusnadi, "Slope Stability Analysis Based on Type, Physical and Mechanical Properties Rock in Teluk Pandan District, East Kutai Regency, East Kalimantan", Journal of Geoscience, Engineering, Environment, and Technology, vol. 2, no. 4, pp. 272-277, 2017.

Derivation of Empirical Equations for Determination of Safe Pit Slope Geometry at Phukham Mining

- [8] I. L. Muthreja, R. R. Yerpude, and J. L. Jethwa, "Role of Site Selection on the Stability of Surface Coal Mine Waste Dumps", *Indian Mining and Engineering Journal*, vol. 51, no.9, 2012.
- [9] C. Romer, and M. Ferentinou, "Numerical Investigations of Rock Bridge Effect on Open Pit Slope Stability", *Journal of Rock Mechanics and Geotechnical Engineering*, vol. 11, pp. 1184-1200, 2019.
- [10] D. C. Wyllie, and C. W. Mah, *Rock Slope Engineering: Civil and mining*, 4th edition, Spon Press, Taylor & Francis Group, London, UK, 2015.
- [11] L. Wendai, *Regression Analysis, Linear Regression and Profit Regression*, Publishing House of Electronics Industry, Beijing, China, 2000.



BIOGRAPHY

Wasan Saranart was born in 1979 in Phetchaboun Province, Thailand. He received his Bachelor's Degree in Engineering (Geotechnical) from Suranaree University of Technology in 2001. For his post-graduate, he works at Phu Bia Mining Limited in Lao, PDR since 2008 and commenced to study with a Master's degree in Civil, Transportation and Geo-resources Engineering Program, Institute of Engineering, Suranaree University of Technology. During graduation, 2020-202

